

**CARBON DIOXIDE HYDROGENATION TO METHANE  
OVER SILICA SUPPORTED NICKEL CATALYSTS IN A  
DIFFERENTIAL REACTOR AND KINETIC MODEL  
DEVELOPMENT**

**Miss Angkana Khuenpetch**



**A Dissertation Submitted in Partial Fulfillment of the Requirements  
for the Degree of Doctor of Philosophy in Chemical Technology  
Department of Chemical Technology  
FACULTY OF SCIENCE  
Chulalongkorn University  
Academic Year 2021  
Copyright of Chulalongkorn University**

ไฮโดรจีนชั้นของคาร์บอนไดออกไซด์เป็นมีเทนบนตัวเร่งปฏิกิริยานิกเกิลบนตัวรองรับซิลิกาใน  
เครื่องปฏิกรณ์คิฟเฟอร์นเซียลและการพัฒนาแบบจำลองทางจลนศาสตร์



วิทยานิพนธ์นี้เป็นส่วนหนึ่งของการศึกษาตามหลักสูตรปริญญาวิทยาศาสตรดุษฎีบัณฑิต  
สาขาวิชาเคมีเทคนิค ภาควิชาเคมีเทคนิค  
คณะวิทยาศาสตร์ จุฬาลงกรณ์มหาวิทยาลัย  
ปีการศึกษา 2564  
ลิขสิทธิ์ของจุฬาลงกรณ์มหาวิทยาลัย

Thesis Title                                    CARBON DIOXIDE HYDROGENATION TO  
METHANE OVER SILICA SUPPORTED NICKEL  
CATALYSTS IN A DIFFERENTIAL REACTOR AND  
KINETIC MODEL DEVELOPMENT

By    Miss Angkana Khuenpetch

Field of Study                                    Chemical Technology

Thesis Advisor                                   Associate Professor PRASERT REUBROYCHAROEN,  
Ph.D.

---

Accepted by the FACULTY OF SCIENCE, Chulalongkorn University in  
Partial Fulfillment of the Requirement for the Doctor of Philosophy

..... Dean of the FACULTY OF  
SCIENCE  
(Professor POLKIT SANGVANICH, Ph.D.)

DISSERTATION COMMITTEE

..... Chairman  
(Associate Professor Chanatip Samart, Ph.D.)

..... Thesis Advisor  
(Associate Professor PRASERT REUBROYCHAROEN,  
Ph.D.)

..... Examiner  
(Professor NAPIDA HINCHIRANAN, Ph.D.)

..... Examiner  
(Professor Chawalit Ngamcharussrivichai, Ph.D.)

..... Examiner  
(Professor THARAPONG VITIDSANT, Ph.D.)

จุฬาลงกรณ์มหาวิทยาลัย  
CHULALONGKORN UNIVERSITY

อังกฤษ ชื่อเพชร : ไฮโดรจิเนชันของคาร์บอนไดออกไซด์เป็นมีเทนบนตัวเร่งปฏิกิริยานิกเกิลบนตัวรองรับซิลิกาในเครื่องปฏิกรณ์ดิฟเฟอเรนเชียลและการพัฒนาแบบจำลองทางจลนศาสตร์. ( CARBON DIOXIDE HYDROGENATION TO METHANE OVER SILICA SUPPORTED NICKEL CATALYSTS IN A DIFFERENTIAL REACTOR AND KINETIC MODEL DEVELOPMENT) อ.ที่ปรึกษาหลัก : รศ. ดร.ประเสริฐ เรียบร้อยเจริญ

งานวิจัยนี้ศึกษาจลนศาสตร์ของกระบวนการผลิตมีเทนจากคาร์บอนไดออกไซด์โดยใช้ตัวเร่งปฏิกิริยาเชิงพานิชย์นิกเกิลบนตัวรองรับซิลิกาโดยใช้เครื่องปฏิกรณ์ไอโซเทอร์มอลดิฟเฟอเรนเชียล โดยศึกษาที่อุณหภูมิ 300–350 °C และความดัน 0.1–0.9 MPa อัตราการป้อนสารตั้งต้นต่อปริมาตรของตัวเร่งปฏิกิริยาอยู่ที่ 37,494 h<sup>-1</sup> และอัตราส่วนป้อนของไฮโดรเจนต่อคาร์บอนไดออกไซด์ 1/1, 2/1, 4/1 และ 5/1 ซึ่งการเปลี่ยนแปลงของคาร์บอนไดออกไซด์ที่สมมติขึ้นที่ศึกษาอยู่ในช่วง 0 ถึง 0.7 นอกจากนี้ยังมีการป้อนแก๊สผลิตภัณฑ์ คือ มีเทน และ น้ำ เพื่อคำนวณหาลำดับของปฏิกิริยา และ ยับยั้งการเสื่อมสภาพของตัวเร่งปฏิกิริยาในขณะศึกษาจลนศาสตร์ สำหรับการทดลองก่อนอื่นป้อนสารในสถานะสมดุลที่อุณหภูมิ 500 °C ระยะเวลา 35 h เพื่อให้ตัวเร่งปฏิกิริยามีความสามารถในการเร่งปฏิกิริยาเริ่มต้นที่เท่ากันทุกเงื่อนไขการทดลอง สมการกำลัง (PL, PL-H<sub>2</sub>O, PL-WI, PL-OH) และสมการของแลงเมียร์-อินเซลวูดถูกนำมาใช้เพื่อการประมาณค่าพารามิเตอร์ โดยเริ่มจากการพิจารณาเพียงปฏิกิริยาซาบาเทียร์ จากนั้นพิจารณาการเกิดคาร์บอนมอนอกไซด์ผ่านปฏิกิริยาออกเตอร์แก๊สซิฟิเคชันกลับโดยใช้สมการกำลัง จากการพิจารณาค่า AIC และ BIC เพื่อเลือกแบบจำลองที่เหมาะสมที่สุด พบว่าแบบจำลองผสมระหว่างแลงเมียร์-อินเซลวูด และ สมการกำลังแสดงผลลัพธ์ที่มีความเหมาะสมที่สุด ซึ่งสามารถอธิบายได้ว่ากระบวนการเกิดมีเทนของคาร์บอนไดออกไซด์โดยใช้ตัวเร่งปฏิกิริยานิกเกิลบนตัวรองรับซิลิกาเกิดผ่านกลไกผสมระหว่าง A และ B โดยการก่อตัวของฟอร์มิลเป็นขั้นกำหนดอัตราและยังอธิบายได้ว่าปฏิกิริยายับยั้งอิทธิพลของน้ำ

จุฬาลงกรณ์มหาวิทยาลัย  
CHULALONGKORN UNIVERSITY

สาขาวิชา เคมีเทคนิค

ลายมือชื่อนิติ

ปีการศึกษา 2564

ลายมือชื่อ อ.ที่ปรึกษาหลัก

# # 6172865123 : MAJOR CHEMICAL TECHNOLOGY

KEYWORD CARBON DIOXIDE METHANATION, KINETICS, CARBON  
DIOXIDE TO METHANE, POWER-TO-GAS, NI/SIO2  
CATALYST

Angkana Khuenpetch : CARBON DIOXIDE HYDROGENATION TO  
METHANE OVER SILICA SUPPORTED NICKEL CATALYSTS IN A  
DIFFERENTIAL REACTOR AND KINETIC MODEL  
DEVELOPMENT. Advisor: Assoc. Prof. PRASERT  
REUBROYCHAROEN, Ph.D.

Development of a kinetic model for CO<sub>2</sub> methanation over a commercial nickel catalyst was performed to consider pathways of CO<sub>2</sub> conversion via Sabatier and RWGS reactions. H<sub>2</sub>/CO<sub>2</sub> ratio in the feed gas composition was varied at the stoichiometry of the Sabatier reaction assuming a fictitious CO<sub>2</sub> conversion of 0 to 0.7. Non-stoichiometric gas feeding and the addition of product gases, i.e., methane and steam, were also considered to examine reaction orders and inhibition effects. The kinetic tests were carried out at 300–350 °C and 0.1–0.9 MPa. GHSV corresponded to 37,494 h<sup>-1</sup>. The stable activity was achieved by forcibly stressing the catalyst under the equilibria at 500 °C for 35 h. The kinetic measurements were conducted at an isothermal differential fixed bed reactor in the absence of heat and mass transport limitations. The methanation reaction was first fitted with a power law (PL, PL-H<sub>2</sub>O, PL-WI, PL-OH) and LH approaches by considering the Sabatier reaction. Then, the RWGS reaction was added to consider CO formation using power law models. The least-square method was performed to minimize the residues between experimented and predicted reaction rate values for prediction kinetic parameters. The models were discriminated under the lowest value of the Akaike information criterion (AIC) and Bayesian information criterion (BIC). The results showed a better fitting of experimental observations by using the LH expression with the formation of formyl as RDS and power law model with inhibiting influence of water.

CHULALONGKORN UNIVERSITY

Field of Study: Chemical Technology

Student's Signature

Academic Year: 2021

Advisor's Signature

Year:

.....

## ACKNOWLEDGEMENTS

Throughout the Ph.D. Thesis, I have received a great deal of support and assistance.

I would first like to extend my sincere thanks to Assoc. Prof. Dr. Prasert Reubroycharoen for your patient support and all of the opportunities.

I must also thank Prof. Dr.Koyo Norinaga for supporting me during the past a year in Nagoya, Japan. Your valuable guidance raised my thesis better.

I would like to express my deepest appreciation to Dr. Choi Cheolyong, whose expertise was invaluable in the research questions and methodology. Your suggestion and question pushed me to sharpen my thinking and brought my work to a higher level.

Special thanks to the financially supported by Chulalongkorn University Dussadeepipat Scholarship (PTT PLC.-Science) and Thailand Science research and Innovation Fund Chulalongkorn University (CU\_FRB65\_bcg (11)\_079\_23\_09))

Many thanks to the laboratory worker of Assoc. Prof. Dr. Prasert Reubroycharoen and Prof. Dr.Koyo Norinaga to assist me.

More importantly, I would like to thank my family, my husband, and my friend for their sympathetic ear.

Finally, I would like to thank myself for doing all the hard work, never giving up, and being patient to get the goal.

จุฬาลงกรณ์มหาวิทยาลัย  
CHULALONGKORN UNIVERSITY

Angkana Khuenpetch

# TABLE OF CONTENTS

	<b>Page</b>
.....	iii
ABSTRACT (THAI) .....	iii
.....	iv
ABSTRACT (ENGLISH) .....	iv
ACKNOWLEDGEMENTS .....	v
TABLE OF CONTENTS .....	vi
LIST OF TABLES .....	ix
LIST OF FIGURES .....	x
LIST OF ABBREVIATIONS .....	x
CHAPTER I .....	1
INTRODUCTION .....	1
1.1. Significance of problem.....	1
1.2. Research objectives.....	2
1.3. Scope of research.....	2
1.4. Benefits .....	2
CHAPTER II.....	3
THEORY AND LITERATURE REVIEW .....	3
2.1. The Carbon dioxide problems.....	3
2.2. Energy demand .....	3
2.3. Technologies for reducing the CO <sub>2</sub> concentration.....	4
2.4. The CO <sub>2</sub> Methanation: Sabatier Reaction.....	5
2.5. Catalysts for CO <sub>2</sub> Methanation .....	6
2.6. Catalyst deactivation [21, 26, 29] .....	7
2.7. Effect of temperature .....	9
2.8. Effect of gas hourly space velocity (GHSV) .....	10

2.9. Effect of H <sub>2</sub> /CO <sub>2</sub> ratio.....	10
2.10. Mechanism.....	11
2.11. Kinetic study.....	15
2.12. Reactor for kinetic study.....	17
2.13. Related literatures.....	18
CHAPTER III.....	21
RESEARCH PROCEDER.....	21
3.1. Kinetic measurements.....	21
3.2. Reactor operation.....	22
3.3. Assessment of diffusional limitations.....	24
3.4. Parameter estimation and kinetic equation.....	25
3.5. Model discrimination and thermodynamic consistency.....	29
CHAPTER IV.....	31
RESULTS AND DISCUSSION.....	31
4.1. Catalyst deactivation.....	31
4.2. Isothermal operation.....	32
4.3. Diffusional limitation.....	32
4.4. Apparent activation energy and reaction order.....	36
4.5. Kinetic model and parameter estimation.....	38
CHAPTER V.....	47
CONCLUSION.....	47
5.1. Conclusion.....	47
5.2. Recommendation.....	47
APPENDIX.....	48
APPENDIX A.....	48
APPENDIX B.....	56
APPENDIX C.....	57
APPENDIX D.....	59
APPENDIX E.....	65



APPENDIX F .....	68
REFERENCES .....	70
VITA.....	80



## LIST OF TABLES

	<b>Page</b>
Table 1. Possible reactions occurring in methanation of carbon oxides [21] .....	5
Table 2. Propose mechanism over Ni/CeO <sub>2</sub> catalysts via formate intermediate [56].	12
Table 3. Propose mechanism via carbon intermediate [61-64].....	14
Table 4. Propose mechanism via formyl intermediate [64] .....	14
Table 5. CO <sub>2</sub> methanation over supported Ni catalysts rate equations proposed .....	16
Table 6. Experimental condition for kinetic study.....	22
Table 7. Criteria equation to assess transport limitation [67] .....	24
Table 8. Criteria equation to assess diffusional limitation [96] .....	24
Table 9. CO <sub>2</sub> methanation via CO intermediated formation-Mechanism A [65].....	26
Table 10. CO <sub>2</sub> methanation via HCOO intermediated formation-Mechanism B [65]	27
Table 11. CO <sub>2</sub> methanation via hybrid mechanism-Mechanism AB [65] .....	27
Table 12. Exponents of Eq.3.9.....	28
Table 13. Parameters used in the assessment of diffusional limitation .....	33
Table 14. Calculated values for diffusional limitation.....	33
Table 15. Criteria for mass and heat transfer limitations.....	34
Table 16. Criteria for diffusional limitations .....	34
Table 17. The values for model discrimination .....	39
Table 18. Estimated parameter from PL-H <sub>2</sub> O (PL-H <sub>2</sub> O <sub>Sabatier</sub> and PL-H <sub>2</sub> O <sub>RWGS</sub> ) .....	40
Table 19. Values for model discrimination of LH approach .....	42
Table 20. Estimated parameter from hybrid models (NO <sub>8</sub> <sub>Sabatier</sub> and PL-H <sub>2</sub> O <sub>RWGS</sub> ) ..	43
Table 21. Values for model discrimination of LH approach .....	45

## LIST OF FIGURES

	<b>Page</b>
Figure 1. Hydrogenation of CO <sub>2</sub> to value-added products [17, 18].....	4
Figure 2. Proposed mechanism under H <sub>2</sub> S poisoning for Ni-CeO <sub>2</sub> catalyst [34].....	7
Figure 3. CO <sub>2</sub> conversion change with H <sub>2</sub> S present in CO <sub>2</sub> steam.....	8
Figure 4. Schematic representation of supported metal catalysts sintering.....	8
Figure 5. Carbon species and adsorption regions in infrared spectra [58].....	14
Figure 6. Schematic diagram of the CO <sub>2</sub> methanation reactor.....	23
Figure 7. Deactivation of the catalyst during ageing.....	31
Figure 8. Temperature difference under furnace temperature 300–350 °C.....	32
Figure 9. Diffusional limitation results from calculation Table 7: (a) external mass; (b) internal mass; (c) internal heat; (d) internal mass transfer limitations.....	35
Figure 10. Diffusional limitation results from calculation Table 8: (a) Pressure drop; (b) Axial dispersion; (c) inert bed dilution; (d) Radial heat transfer limitation.....	35
Figure 11. Apparent activation energy with Arrhenius plot (H <sub>2</sub> /CO <sub>2</sub> /Ar = 4/1/2.14): (a) Sabatier reaction; (b) RWGS reaction.....	36
Figure 12. Determining apparent reaction order for Sabatier reaction at different temperatures and total pressures: (a) 0.1MPa; (b) 0.5MPa; and (c) 0.9MPa.....	37
Figure 13. Determining apparent reaction order for RWGS reaction at different temperatures and total pressures: (a) 0.1MPa; (b) 0.5MPa; and (c) 0.9MPa.....	37
Figure 14. Reaction order of H <sub>2</sub> from estimation: (H <sub>2</sub> /CO <sub>2</sub> /Ar = 1/1/2, 1/1/0.67, 2/1/3, 2/1/7 5/1/2, T=300–350 °C, 0.1–0.9 MPa.).....	38
Figure 15. Calculated r <sub>CH<sub>4</sub></sub> using estimated parameters from Figure 14.....	38
Figure 16. Results from fitting PL-H <sub>2</sub> O model: (a) r <sub>CH<sub>4</sub></sub> ; (b) r <sub>CO</sub> ; (c) r <sub>CO<sub>2</sub></sub> .....	39
Figure 17. Results from fitting LH: (a) r <sub>CH<sub>4</sub></sub> ; (b) r <sub>CO</sub> ; (c) r <sub>CO<sub>2</sub></sub> .....	43
Figure 18. Prediction performance of reactor for Ni/SiO <sub>2</sub> catalyst under H <sub>2</sub> /CO <sub>2</sub> /Ar = 4/1/5, P = 0.5 MPa, Q = 200 and 20 ml/min, m = 20 mg. ....	45
Figure 19. Temperature versus CO <sub>2</sub> conversion compared to other literature for H <sub>2</sub> /CO <sub>2</sub> /Ar = 4/1/5 P = 0.5 MPa, Q = 200 ml/min, m = 20 mg. ....	46

## LIST OF ABBREVIATIONS

$r_{obs}$	$r_{CO_2}$ from experiment
$R_p$	Particle radius
$d_p$	Particle diameter
$n$	Reaction order
$\tau_g$	Bed tortuosity
$\varepsilon_p$	Bed porosity
$E_a$	Activation energy
$\lambda_s$	Thermal conductivity of catalyst (Ni/SiO <sub>2</sub> )
$\lambda_{inert}$	Thermal conductivity of inert ( $\gamma$ Al <sub>2</sub> O <sub>3</sub> )
$\rho_b$	Bulk density of catalyst bed
$\rho_{inert}$	Bulk density of inert material
$H$	Catalyst bed height
$d_t$	Catalyst bed diameter
$P$	Total pressure
$X_{CO_2}$	CO <sub>2</sub> conversion
$W_{cat}$	Amount of catalyst (Ni/SiO <sub>2</sub> ) material
$W_{inert}$	Amount of Inert ( $\gamma$ Al <sub>2</sub> O <sub>3</sub> ) material
$\rho_g$	The density of gas mixture
$u_o$	Fluid superficial velocity
$\mu_g$	the viscosity of the gas mixture
$D_{CO_2,mix}$	Diffusivity of CO <sub>2</sub> in gas mixture
$D_{CO_2,e}$	Effective diffusivity
$C_{CO_2,s}$	The concentration of CO <sub>2</sub> at the solid surface
$C_{CO_2,b}$	The concentration of CO <sub>2</sub> at the bulk phase
$k_g$	Mass transfer coefficient
$\Delta H_r$	Heat of reaction
$\lambda_e$	Effective thermal conductivity of particle
$\lambda_{er}$	Effective radial thermal conductivity in the bed catalyst
$\lambda_g$	Thermal conductivity of gas mixture
$h$	Heat transfer coefficient
COOH*	formate species
CO*	carbonyl species
CO <sub>3</sub> <sup>2-</sup>	Carbonate species
*COOH	Carboxyl species
HCO <sub>3</sub> <sup>-</sup>	bicarbonate species
O*	oxygen active site (oxygen vacancy)
* <sub>M</sub>	is the Ni active site
PL	Power law rate equation
LH	Langmuir-Hinshelwood

# CHAPTER I

## INTRODUCTION

### 1.1. Significance of problem

The CO<sub>2</sub> concentration in the atmosphere has been continuously increased from fossil fuels consumption. This occurrence entirely affects human health and the environment. There are two considered worldwide options to reduce CO<sub>2</sub> concentration in the atmosphere: capture CO<sub>2</sub> and storage (CCS) and capture CO<sub>2</sub> and utilization (CCU). CCS is a technology that CO<sub>2</sub> is collected from industrial facilities or power plants to permanent store it underground. In comparison, CCU aims to convert the captured CO<sub>2</sub> into value-added products such as methanol, dimethyl ether, formic acid, ethylene oxide and ethanol, methane, and other hydrocarbons. CCU is extensively emphasized because of environmentally beneficial and economically profitable. Because of increasing natural gas demand, methane production was deemed one key role for sustainable energy. Furthermore, numerous researchers have paid attention to power-to-gas (PtG) technology. In case of CO<sub>2</sub> methanation, it can be called power-to-methane. Hydrogen via the electrolysis reacts with emitted CO<sub>2</sub> to produce methane and water. The hydrogenation of CO<sub>2</sub> to produce methane is also known as the Sabatier reaction. However, the combined reversed water gas shift reaction and CO methanation are widely accepted. Since CO<sub>2</sub> methanation thermodynamically favors at low temperatures, it is necessary to design a suitable catalyst to achieve a high reaction rate and methane selectivity. The Ni/SiO<sub>2</sub> catalyst popularly has been used for CO<sub>2</sub> methanation. Even though numerous works were published in the development of Ni/SiO<sub>2</sub> performance, few literature studies the kinetic characterization of Ni/SiO<sub>2</sub>.

This work aims to determine intrinsic kinetic parameters and predict the mechanism of CO<sub>2</sub> methanation reaction over commercial Ni/SiO<sub>2</sub> catalyst using an isothermal differential fixed bed reactor without diffusional limitation. The kinetics were investigated with feeding gas compositions by following and non-following the stoichiometry of the Sabatier reaction ( $H_2/CO_2 = 4/1$ ,  $CH_4/H_2O = 1/2$ ), and the experimental observations were considered in modeling using power law and Langmuir-Hinshelwood models with AIC and BIC for model discrimination.

## 1.2. Research objectives

1. Determination of kinetic parameters over commercial 17–23%wt Ni/SiO<sub>2</sub> catalyst
2. Examination of mechanism over commercial 17–23%wt Ni/SiO<sub>2</sub> catalyst

## 1.3. Scope of research

This study focuses on determining kinetic parameters and finding out the mechanism using the power law and Langmuir-Hinshelwood models. Recent thesis will use an isothermal differential tubular fixed bed reactor to perform the CO<sub>2</sub> methanation over commercial 17–23%wt Ni/SiO<sub>2</sub> catalyst without heat and mass transport limitations. The kinetic characterizations were investigated at temperatures of 300–350 °C, pressures of 0.1–0.9 MPa, and a total flow rate of 200 mL/min with the catalyst loading 20 mg. The model discrimination was assessed by the AIC and BIC.

## 1.4. Benefits

This work observed the suitable model and parameters to describe the kinetics and mechanism for CO<sub>2</sub> hydrogenation to CH<sub>4</sub> over Ni/SiO<sub>2</sub> catalyst.

## CHAPTER II

### THEORY AND LITERATURE REVIEW

#### 2.1. The Carbon dioxide problems

Thus far, the concentration of carbon dioxide in the atmosphere has continuously increased [1] because of natural systems and human activities. Industrial activities demonstrated approximately 90% of all CO<sub>2</sub> emissions from human activities [2]. Carbon dioxide is the main component in greenhouse gases (GHGs) and one of the primary problems of climate change [3]. The increasing of CO<sub>2</sub> concentration results in hard plants growth [4] and rising sea levels due to melting of ice sheets [5, 6]. Moreover, a number of natural phenomena such as storms, floods, drought and heatwaves, and others are cause of increasing of CO<sub>2</sub> concentration [7]. Besides effect on natural balance, the increasing of CO<sub>2</sub> concentration effects to human health, for example, body inflammations, reductions in cognitive abilities, losings mineral in bone, calcification of the kidney, worsen the stress, endothelial dysfunction [8], hypertension, cardiovascular diseases, and water-borne diseases [9].

#### 2.2. Energy demand

Coal, crude oil, and natural gas are the most crucial fossil fuel sources of energy worldwide [10]. Natural gas is multipurpose consumption. It is mainly used for power generation followed by household consumption, and it is extensively used in industries [11], such as fuel in automotive industries and heating in industries. In addition, it is used as a raw material in the chemical industries or iron and steel industry [12]. Sometimes, it is also used as an alternative to transportation fuel and services. Furthermore, EIA expected that natural gas consumption in the industrial sector will increase 40% from 2022 to 2050 [13]. Although natural gas presents lower air pollution compared to others fossil fuels, it releases some toxic gases while combustion, including nitrogen oxides (NO<sub>x</sub>) [14] and CO<sub>2</sub> [15]. Then renewable natural gas plays a key role in environment-friendly energy and meets the energy demand.

### 2.3. Technologies for reducing the CO<sub>2</sub> concentration

There are two considered worldwide options to reduce carbon dioxide concentration in the atmosphere, carbon capture and storage (CCS) and carbon capture and utilization (CCU) technologies [16]. The difference between CCS and CCU is the ended status of CO<sub>2</sub> capture. CCS captures CO<sub>2</sub> to transport it to a storage site for long-term storage, whereas CCU aims to convert the captured CO<sub>2</sub> into value-added products. The different routes and different catalysts to produce CO, dimethyl ether, higher alcohol, and hydrocarbons are shown in Figure 1 [17, 18]. In addition, methanol can produce from CO<sub>2</sub> hydrogenation to methanol (Eq. 2.1) or via RWGS reaction and continue producing methanol (Eq. 2.2) over metal catalysts such as Pd-Cu, Pd-Zn, Cu-Zn, Pd, Pt, and In [19]. Eqs 2.3 and 2.4 represent the production of hydrocarbons from CO<sub>2</sub> hydrogenation via the RWGS reaction [18].

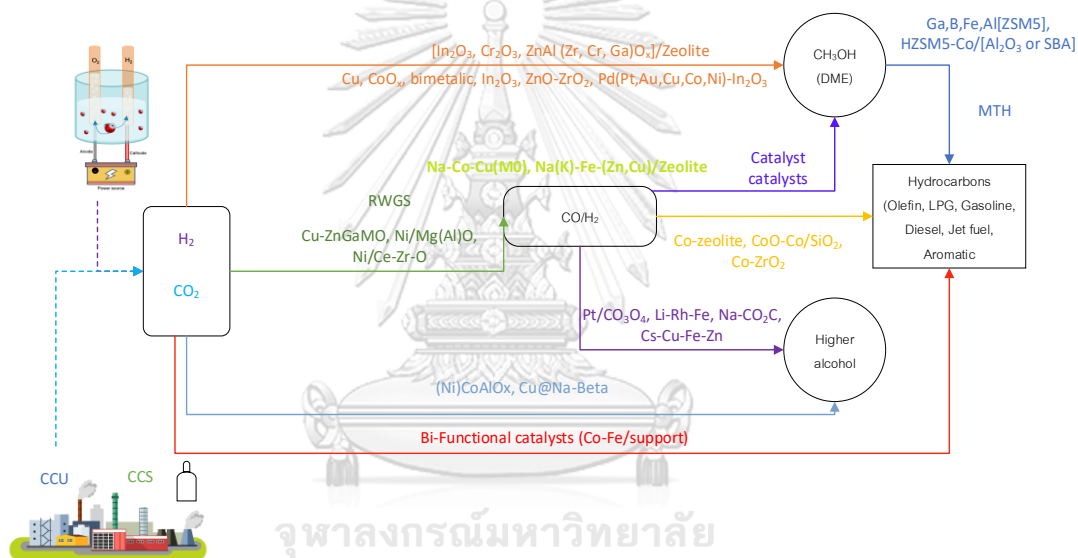
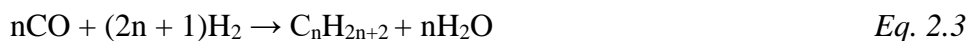
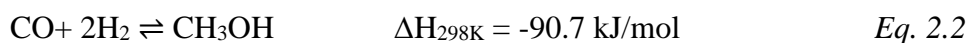
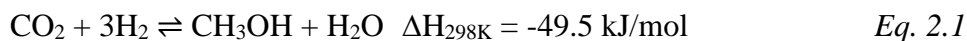


Figure 1. Hydrogenation of CO<sub>2</sub> to value-added products [17, 18]



The CO<sub>2</sub> methanation or Sabatier reaction is one of process to produce renewable fuels and plays an important role in commercialization [12, 20].



## 2.4. The CO<sub>2</sub> Methanation: Sabatier Reaction

Brodie, in 1872, was first described the conversion of CO<sub>2</sub> to CH<sub>4</sub> by applying an electric discharge to a CO/CO<sub>2</sub>/H<sub>2</sub> mixture followed by French chemists. In 1902, Paul Sabatier and Jean-Baptiste Senderens observed the same reaction using heterogeneous catalysts. Later on, Sabatier was rewarded with the Nobel Prize in 1912 for the “method of hydrogenating organic compounds in the presence of finely disintegrated metals”[21]. The CO<sub>2</sub> methanation, also called the Sabatier reaction, is reaction between H<sub>2</sub> and CO<sub>2</sub> to produce CH<sub>4</sub> and H<sub>2</sub>O, as shown in Eq.2.5. For two steps CO<sub>2</sub> methanation reaction, first step is endothermic reversed water gas shift reaction (RWGS) that is conversion of CO<sub>2</sub> and H<sub>2</sub> into CO and H<sub>2</sub>O, the second step is exothermic CO methanation that is reaction of CO from first step and excess H<sub>2</sub> to produce CH<sub>4</sub> and H<sub>2</sub>O, as shown in Eqs.2.6 and 2.7, respectively [22, 23]. Note that CO<sub>2</sub> methanation is thermodynamically responsive ( $\Delta G_{298K} = -130.8$  kJ/mol) at low temperatures [21, 24] and low pressure [21]. It will have the opportunity to achieve CO more than CH<sub>4</sub> when the reaction temperature is higher than 450 °C [24] or reaction conditions proper for RWGS. Some side reactions that may occur in CO<sub>2</sub> methanation are listed in Table 1.

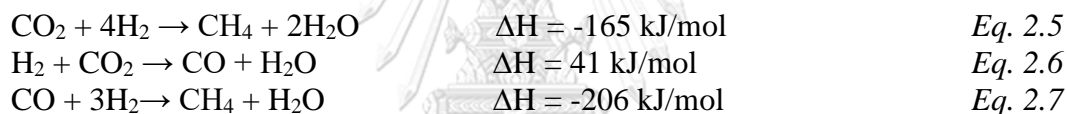


Table 1. Possible reactions occurring in methanation of carbon oxides [21]

Reaction	Reaction Type	$\Delta H_{298}$ (kJ/mol)
<b>CH<sub>4</sub> forming</b>		
$2\text{CO}_{(g)} + 2\text{H}_{2(g)} \rightleftharpoons \text{CH}_{4(g)} + \text{CO}_{2(g)}$	Inverse methane dry reforming	- 247.3
<b>Carbon forming</b>		
$\text{CH}_{4(g)} \rightleftharpoons 2 \text{H}_{2(g)} + \text{C}_{\text{graphite(s)}}$	Methane cracking	74.6
$\text{CO}_{(g)} + \text{H}_{2(g)} \rightleftharpoons \text{C}_{\text{graphite(s)}} + \text{H}_2\text{O}_{(g)}$	CO reduction	-131.3
$\text{CO}_{2(g)} + 2\text{H}_{2(g)} \rightleftharpoons \text{C}_{\text{graphite(s)}} + 2\text{H}_2\text{O}_{(g)}$	CO <sub>2</sub> reduction	- 90.1
<b>Hydrocarbon forming</b>		
$n\text{CO}_{(g)} + (2n + 1)\text{H}_{2(g)} \rightleftharpoons \text{C}_n\text{H}_{2n + 2(g)} + n\text{H}_2\text{O}_{(g)}$	Alkane formation	-
$n\text{CO}_{(g)} + 2n\text{H}_{2(g)} \rightleftharpoons \text{C}_n\text{H}_{2n(g)} + n\text{H}_2\text{O}_{(g)}$	Alkene formation	-

## 2.5. Catalysts for CO<sub>2</sub> Methanation

Since CO<sub>2</sub> is a stable molecule, converting it into a different molecule is normally energy intensive. Then, CO<sub>2</sub> methanation requires a highly active catalyst to overcome the kinetic energy barrier or reduce activation energy ( $E_a$ ) to achieve high rates and selectivity of CH<sub>4</sub> [25]. The catalysts were used in CO<sub>2</sub> methanation such as iron (Fe), cobalt (Co), nickel (Ni), copper (Cu), rhodium (Rh), ruthenium (Ru), palladium (Pd), iridium (Ir), platinum (Pt) and gold (Au) supported on silicon dioxide (SiO<sub>2</sub>), alumina (Al<sub>2</sub>O<sub>3</sub>), zeolites, titanium dioxide (TiO<sub>2</sub>), and carbon nanomaterials with potassium (K), sodium (Na), Lithium (Li), Cesium (Cs), manganese (Mn) as a promoter. The activity and selectivity of the respective metal catalysts are shown below [24, 26, 27].

Activity: Ru>Fe>Ni>Co>Rh>Pd>Pt>Ir

Selectivity: Pd>Pt>Ir>Ni>Rh>Co>Fe>Ru

Noble metals are very active metals and have high CH<sub>4</sub> selectivity even at low temperatures, but they are limited in term of high price [21]. At present, Ni-based catalysts are the most commonly used in CO<sub>2</sub> methanation because they are highly active catalysts, have high CH<sub>4</sub> selectivity, and are low cost [28].

Support materials play an important role in the performance of a heterogeneous catalyst. Relation between a metal catalyst and support influences the catalytic activity such as catalyst metal dispersion, electron transfer between the metal and the support, and the introduction of additional defects sites on the support. In the last decade, many types of supporting materials have been published, including zeolite materials, carbon (carbon nanotubes, activated carbon, carbon nanofiber, and so on), and oxide support groups (Al<sub>2</sub>O<sub>3</sub>, SiO<sub>2</sub>, ZrO<sub>2</sub>, TiO<sub>2</sub>, CeO<sub>2</sub> and so on) [29]. According to oxide support materials, Al<sub>2</sub>O<sub>3</sub> is the most commonly used for methanation catalysts because of their complicated chemistry and various crystallographic modifications, including  $\gamma$ ,  $\kappa$ ,  $\delta$ ,  $\theta$ ,  $\alpha$  phase [24]. Then, Ni/ $\gamma$ -Al<sub>2</sub>O<sub>3</sub> is the most commonly used for industrial [21]. However, limitation of the Ni/ $\gamma$ -Al<sub>2</sub>O<sub>3</sub> catalysts is sintering while the water presence in process at high temperature. The Other supporting materials that got attention are metal-organic framework (MOF). The MOF show a highly controlled structure and high surface areas up to and above 1000 m<sup>2</sup>g<sup>-1</sup> [24], but they are an expensive catalyst to be a commercial catalyst [24].

According to Ni/SiO<sub>2</sub> catalyst, although it stands for a large surface area around 163 m<sup>2</sup> g<sup>-1</sup> of 10wt%Ni/SiO<sub>2</sub> [30], it has been established in low CO<sub>2</sub> conversion [31], and it is facial chemical deactivation and thermal deactivation. Then, several researchers have been attempted to improve Ni/SiO<sub>2</sub> performance. For instance, GuO et al. (2014) added MgO as a promoter to increase the capacity of CO<sub>2</sub> adsorption, inhibit Ni sintering, and oxidation [31]. Like Dias et al. (2021), who applied promoters (Fe, Co) to improve the dispersion of Ni leading to smaller crystallite size and modified the reducibility of NiO. It also enhanced the carbon

deposit (cooking) and sintering [32]. Besides improving the performance of Ni/SiO<sub>2</sub> catalyst by adding promoter, the preparation method has been investigated. For example, Ye et al. (2019) prepared Ni/SiO<sub>2</sub> catalyst by an ammonia-evaporation method that successfully developed nickel particle size to ultrasmall nickel particles resulting in high dispersion and strong interaction between nickel particle and support [33]. Even though numerous works were published in the development of Ni/SiO<sub>2</sub> performance, few works study the kinetic of Ni/SiO<sub>2</sub>. This work was designed to study kinetics using Ni/SiO<sub>2</sub> because it demonstrates great catalytic performance for a CO<sub>2</sub> conversion and it is widely used in industry for CO<sub>2</sub> methanation.

## 2.6. Catalyst deactivation [21, 26, 29]

Deactivation is a big problem in CO<sub>2</sub> methanation, especially in Ni catalyst. The catalyst deactivation can be classified into chemical deactivation (poisoning and coking), thermal deactivation (sintering), and mechanical deactivation.

1. Poisoning is a chemical reaction of impurities in feed stream. Ni catalysts are sensitive to gas impurity containing hydrogen sulfide (H<sub>2</sub>S). Nickel oxide (NiO) can quickly react with H<sub>2</sub>S to form an inactive phase of nickel sulfide (NiS) on the catalyst's surface, as shown in Eq.2.8 results in catalyst deactivation [20]. Alarcón et al. (2020) presented a scheme of the proposed reaction mechanism of CO<sub>2</sub> methanation under H<sub>2</sub>S poisoning for Ni-CeO<sub>2</sub> catalyst. Obviously, the adsorption of sulfur (green spot) blocks the active site (Figure 2) cause of low methane selectivity and CO<sub>2</sub> conversion [34]. The result from H<sub>2</sub>S in the feed stream is shown in Figure 3.

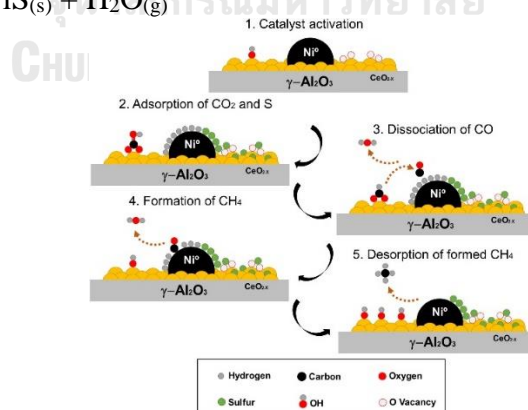


Figure 2. Proposed mechanism under H<sub>2</sub>S poisoning for Ni-CeO<sub>2</sub> catalyst [34]

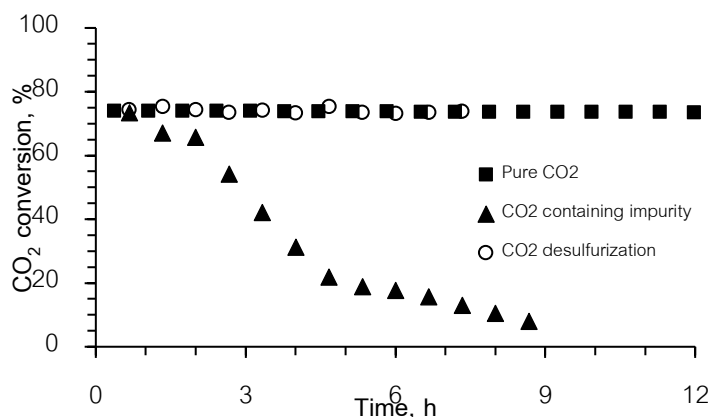


Figure 3.  $\text{CO}_2$  conversion change with  $\text{H}_2\text{S}$  present in  $\text{CO}_2$  steam.

2. Fouling and coking are the main problems of catalyst deactivation in  $\text{CO}_2$  methanation [23]. They are the physical deposition of C species at the active surface, resulting in activity loss due to the blockage of sites and pores. Carbon deposition can occur at a ratio of the hydrogen atom and carbon atom (H/C) in the range of 0.5–1 and operated at a temperature more than 500 °C. It can be called black or hard coke. Regarding white or soft coke, it preferentially formed at the low reaction temperature. Besides, a ratio of H/C and temperature, long time on stream, more acidic sited or high aluminum content, and more basic hydrocarbon encourages the formation of more coke components covering the surface of catalysts with low H/C. To prevent the carbon deposition, the optimization of operating conditions, such as changing pressure or temperature, increasing H/C ratio, and adding steam and the development of catalysts by formation of alloy and adding promoter, were reported.

3. Sintering is the process of merging active metals that results in a lower surface area, as shown in Figure 4. Several researchers supported that sintering of supported Ni catalysts generally can occur at a temperature higher than 500 °C [35–38]. In addition, the water can further accelerate the sintering process. Ni sintering can be developed by increasing the metal-support interaction, adding promoters, improving preparation methods, and operating temperature at less than 30%–40% of the melting point of the used active metal [20].

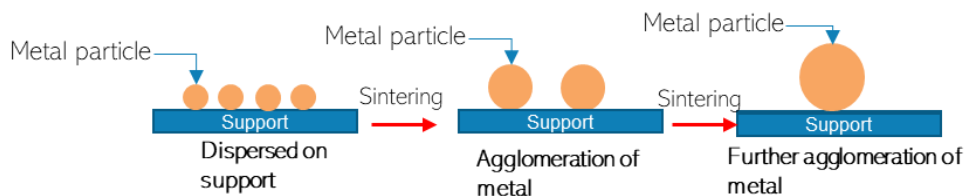


Figure 4. Schematic representation of supported metal catalysts sintering

4. Mechanism failure of catalysts can happen by attrition and/or thermal stress. Attrition is crashing of each other catalyst particles or crashing with the reactor wall and losing some part of the catalyst or loss active surface area. Thermal stress is caused by magnified by temperature gradients across particles and by differences in thermal expansion coefficients at the interface of two different materials, for example, catalyst coating/monolith interface [20].

## 2.7. Effect of temperature

Since the Sabatier process is an exothermic reaction, temperature and pressure are important parameters. Some researchers found that CO<sub>2</sub> methanation is favored at a temperature range between 200–400 °C [23, 29, 39]. However, Thema et al. (2019) reported that the Sabatier process operated at high temperatures (200–550 °C) and high pressure because the CO<sub>2</sub> methanation reaction is thermodynamically more favorable at high operating pressure. At any rate, it depends on the optimal activity of the catalysts [40]. The reaction rate of methane will be increased when the temperature increases. However, it has to be noticed that operating at high temperature (more than 500 °C) can obtain more CO concentration because of the RWGS reaction [29] and the carbon deposited process leading to catalyst deactivation. Jaijian and Gu (2012) focused on carbon oxide (CO and CO<sub>2</sub>) methanation reaction. They reported that the CO<sub>2</sub> conversion decreases with increasing temperature and increases with the pressure [41]. Siakavelas et al. (2021) focused on catalytic performance for the methanation of CO<sub>2</sub> over Ni catalysts supported on cerium (IV) oxide (CeO<sub>2</sub>) and CeO<sub>2</sub>-based oxides at atmospheric pressure, 200-500 °C, 240 mg of catalyst loading, GHSV of 25,000 mLg<sup>-1</sup> h<sup>-1</sup>, H<sub>2</sub>/CO<sub>2</sub> molar ratio equal to 4, and feeding 50% Ar in a continuous flow fixed bed tubular reactor. They found that CO<sub>2</sub> conversion is increased at the range of temperature 200–400 °C and decreased at 500 °C as well as CH<sub>4</sub> yield. For selectivity, CH<sub>4</sub> selectivity is almost reached 100% until 400 °C, and it is decreased at temperature more than 450 °C, resulting from increasing CO selectivity because of the endothermic character of the RWGS reaction. In addition, at the high operating temperature may be occurred the sintering of nickel [39]. Bukhari et al. (2021) studied the catalytic performance of the Ni supported on fibrous type SBA-15 in CO<sub>2</sub> methanation using a packed-bed reactor at 250–450 °C, atmospheric pressure, catalysts loading of 200 mg, ratio of H<sub>2</sub>/CO<sub>2</sub> equal to 4, and GHSV of 24,900 mL g<sup>-1</sup> h<sup>-1</sup>. The results showed that CH<sub>4</sub> yield and CO<sub>2</sub> conversion were decreased with operating temperature more than 400 °C due to the exothermic nature of CO<sub>2</sub> methanation [42]. Regard to Kesavan et al. (2018), who reported the catalytic conversion of CO<sub>2</sub> to synthetic CH<sub>4</sub> on Ni/YSZ in a fixed bed quartz reactor with 100 mg of catalyst loading, operating temperature equal to 500 °C to 250 °C at atmospheric pressure, and 81600 h<sup>-1</sup> of GHSV. As a

result, above 500 °C, the CO<sub>2</sub> converts to CO instead of CH<sub>4</sub> because of RWGS reaction is favored at high operating temperature. However, CO<sub>2</sub> conversion is continuously increased from 52% to 58% with 375 to 500°C, respectively [43].

## 2.8. Effect of gas hourly space velocity (GHSV)

GHSV is defined as the ratio of the volumetric flow rate of gas feed streams as reactants at standard conditions to the total catalyst volume or total catalyst weight [23]. High GHSV results in low CO<sub>2</sub> conversion and CH<sub>4</sub> selectivity because higher GHSV implies a shorter residence time in the reactor [44]. According to Shafiee et al. (2021), who investigated performance of Ni/Al<sub>2</sub>O<sub>3</sub> catalysts via CO<sub>2</sub> methanation in a quartz fixed bed microreactor. GHSV was studied in the range of 6000 mlg<sup>-1</sup>h<sup>-1</sup> to 30,000 mlg<sup>-1</sup>h<sup>-1</sup> by using 200 mg of catalyst loading and a feed stream containing H<sub>2</sub> and CO<sub>2</sub> (H<sub>2</sub>/CO<sub>2</sub> 4/1). The results showed that a decrease of CO<sub>2</sub> conversion was caused by an increase in GHSV due to the shorter contact time and a lower amount of adsorbed CO<sub>2</sub> or H<sub>2</sub> on the surface of the catalyst; however, the increase in GHSV does not effect on CH<sub>4</sub> selectivity [44]. A similar result was done by Gholami et al. (2021) which the Ni/Cr<sub>2</sub>O<sub>3</sub> catalysts were evaluated in CO<sub>2</sub> methanation reactions via fixed bed continuous flow quartz reactor [45]. Like Taherian et al. (2020), who reported that the conversion of CO<sub>2</sub> declined with an increase in the GHSV due to decreasing contact time between feed gases and catalysts, but methane selectivity is not changed by changing GHSV [46].

## 2.9. Effect of H<sub>2</sub>/CO<sub>2</sub> ratio

The stoichiometric ratio of H<sub>2</sub> and CO<sub>2</sub> in the Sabatier reactor is 4/1, so the molar ratio of H<sub>2</sub>/CO<sub>2</sub> in feed stream should be consumed in CO<sub>2</sub> methanation reaction at less than 4/1. Jaffar et al. (2019) studied the influence of H<sub>2</sub>/CO<sub>2</sub> ratio within the range of 2/1–4/1 at a catalyst temperature of 360 °C using 10wt%Ni/Al<sub>2</sub>O<sub>3</sub> catalysts at a total GHSV of 6000 mLg<sup>-1</sup>h<sup>-1</sup> in fixed bed catalytic reactor. They reported that the optimum H<sub>2</sub>/CO<sub>2</sub> ratio was 4/1 because an optimum H<sub>2</sub>/CO<sub>2</sub> ratio of 4/1 is required [47]. Like Aziz et al. (2014), who reported the same suitable H<sub>2</sub>/CO<sub>2</sub> molar ratio of 4/1 using Ni-based catalysts in a quartz fixed bed reactor [48]. Similarly, Zhou et al. (2015) investigated the effect of H<sub>2</sub>/CO<sub>2</sub> molar ratio within the range of 1/1 to 7/1. They reported that CO<sub>2</sub> conversion and CH<sub>4</sub> selectivity is achieved at the desired level when H<sub>2</sub>/CO<sub>2</sub> molar ratio reached up to 4 which the 2.5Ce–10Ni/γ-Al<sub>2</sub>O<sub>3</sub> catalyst was carried out in a fixed bed reactor with an operating temperature of 400 °C, at pressure of 0.1 MPa and GHSV of 7,200 h<sup>-1</sup> [49]. However, these results conflict with Hatzisymeon et al. (2021), who focused on CO<sub>2</sub> hydrogenation over supported Ni and Ru catalysts using fixed bed reactor. The effect

of H<sub>2</sub>/CO<sub>2</sub> ratio in the feed was investigated over 5wt%Ni/CeO<sub>2</sub> catalyst under a GHSV of 22,750 h<sup>-1</sup>. They found that the CH<sub>4</sub> selectivity was improved with increasing the H<sub>2</sub>/CO<sub>2</sub> molar ratio, indicating that higher amount of H<sub>2</sub> in the feed stream favors the conversion of CO<sub>2</sub> to CH<sub>4</sub> [50]. As the same result with Konsolakis et al. (2019), The effect of the H<sub>2</sub>/CO<sub>2</sub> feed ratio was evacuated over Cu/CeO<sub>2</sub>-NR via quartz fixed bed U-shaped reactor with a mixture of 200 mg catalyst diluted with 200 mg of inert SiO<sub>2</sub>, operated at atmospheric pressure, GHSV of 20,000 h<sup>-1</sup> and H<sub>2</sub>/CO<sub>2</sub> molar ratio of 1–9. With regard to the result, higher H<sub>2</sub>/CO<sub>2</sub> feed ratios are probably to produce methane instead of the CO formation because the Sabatier reactor is more dependent on hydrogen [51]. Also, comparable results have been reported by Han et al. (2020), who studied the effect of H<sub>2</sub>/CO<sub>2</sub> ratio in the range of 3.5 to 5 in CO<sub>2</sub> methanation using 20wt%Ni-Mg-Al catalysts at operating condition following, operating temperature 350 °C at a GHSV of 30,000 h<sup>-1</sup> and 500 mg of the catalyst loading. They reported that increasing the concentration of H<sub>2</sub> in the feed stream results in increasing of CO<sub>2</sub> conversion and CH<sub>4</sub> yield, whereas the CH<sub>4</sub> selectivity remained almost constant [52]. According to the conclusions from these studies, the different H<sub>2</sub>/CO<sub>2</sub> molar ratios required in CO<sub>2</sub> methanation reaction may have considerable effects on the reaction behavior and the dominance of a specific reaction pathway.

## 2.10. Mechanism

Mebrahtu et al. (2019) compiled and categorized the CO<sub>2</sub> methanation reaction mechanisms into two categories. There are an CO<sub>2</sub> associative and a CO<sub>2</sub> dissociative mechanism. In an associative scheme [21], the first mechanism is the CO<sub>2</sub> adsorption on the support and reacts with adsorbed hydrogen atoms (H), then formed in metal to form oxygenates such as formate species (COOH\*) at the metal-support interface. The COOH\* can give rich carbonyl species (CO\*) hydrogenated to methane [53]. It can be noticed that the CO intermediate formation is not taking place in this sequence. On the other hand, a dissociative scheme starts with CO<sub>2</sub> dissociation into carbonyl (CO\*) and an oxygen atom on the metal surface. The carbonyl is then hydrogenated step by step to form methane [21]. However, Zhu et al. (2020) reported mechanisms CO<sub>2</sub> methanation via RWGS reaction into two mechanisms. One is redox mechanism that metal catalyst is oxidized by CO<sub>2</sub> to occur CO, and then H<sub>2</sub> reduces the catalyst to produce CH<sub>4</sub> and H<sub>2</sub>O. The catalyst used in this process must be reducible oxides, which can be reduced and oxidized under reaction conditions. Another is association mechanism that is CO<sub>2</sub> adsorption on the surface of catalysts and reacts with dissociated H to form an intermediate species such as COOH\*, carbonate (CO<sub>3</sub><sup>2-</sup>), carboxyl (\*COOH), and bicarbonate (HCO<sub>3</sub><sup>-</sup>), which is decomposed to CO and H<sub>2</sub>O [54]. Xu et al. (2021) proposed CO<sub>2</sub> methanation mechanism over Ni/ZrO<sub>2</sub> via two experiments, including in-situ Fourier transform

infrared spectroscopy (FTIR) experiments (absence of H<sub>2</sub>) and spin polarized DFT calculations. As regards In-situ FTIR experiments in the absence of H<sub>2</sub>, bidentate carbonates and monodentate carbonates group bands appear at temperatures ranging from 50 to 400 °C, which gradually increase with increasing temperature. Bicarbonate species (CO<sub>3</sub>H\*) are formed at lower temperature and start disappearing at 150 °C along with the HCOO\* formation. HCOO\* rapidly increase at temperatures ranging from 150 °C to 250 °C and then decrease and clearly disappear at 310 °C, while HCOO\* decrease. Methane species (CH<sub>4</sub>\*) will appear at 280 °C. CO\* are produced via transformation of CO<sub>2</sub>\*-Ni species (reaction on metal area) around 340 °C. As for the results via combination In-situ FTIR and DFT calculations show that the interaction between CO<sub>2</sub> and OH sites produce CO<sub>3</sub>H\*, which are formed into CO<sub>2</sub>\* adsorbed state on the Ni/ZrO<sub>2</sub> interface followed by hydrogenated to CH<sub>4</sub>. However, the CO<sub>2</sub> interacting with surface Ni sites are hydrogenated to CO\* as a byproduct more than an intermediate for CO<sub>2</sub> methanation. Moreover, they reported the optimal pathway of CO<sub>2</sub> methanation on the Ni/ZrO<sub>2</sub> catalyst follows the HCOO\* pathway that go through CO<sub>3</sub>H\* → CO<sub>2</sub>\*-interface → HCOO\* → H<sub>2</sub>COO\* → H<sub>2</sub>COOH\* → H<sub>2</sub>CO\* → CH<sub>2</sub>\* → CH<sub>3</sub>\* → CH<sub>4</sub>\* with the rate determining step is the HCOO\* hydrogenation to H<sub>2</sub>COO\*[55].

In the same result with Bian et al. (2020), who reported that possible CO<sub>2</sub> methanation reaction steps over Ni/CeO<sub>2</sub> might come from COOH\* intermediate formation that proposed mechanism in Table 2, where O\* is the oxygen active site (oxygen vacancy) and \*<sub>M</sub> is the Ni active site at the Ni-ceria interface. The kinetic model has been derived via S-4, S-6, and S-10 as rate determining step (RDS) [56]. Similarly, Takano et al. (2016) found the adsorbed COOH\* species formed on the catalysts in the Operando DRIFT study and reported that bidentate carbonate is the most important intermediate on the Ni/Y-doped ZrO<sub>2</sub> catalysts [57].

*Table 2. Propose mechanism over Ni/CeO<sub>2</sub> catalysts via formate intermediate [56]*

Reaction steps	Step
$H_2 + 2^*_{M} \rightarrow 2H^*_{M}$	S-1
$H^*_{M} + O^* \rightarrow OH^* + ^*_{M}$	S-2
$CO_2 + O^* \rightarrow OCO_2^*$	S-3
$OCO_2^* + OH^* \rightarrow OCOOH^* + O^*$	S-4 RDS
$OCOOH^* + H_2 \rightarrow OCOH^* + H_2O$	S-5
$OCOH^* + H_2 \rightarrow OCH_2OH^*$	S-6 RDS
$OCH_2OH^* + H_2 \rightarrow OCH_3^* + H_2O$	S-7
$OCH_3^* + H_2 \rightarrow CH_4 + OH^*$	S-8
$OCO_2^* + H_2 \rightarrow OCO^* + H_2O$	S-9
$OCOH^* + OCO_2^* \rightarrow OCO^* + OCOOH^*$	S-10 RDS
$OCOH^* + O^* \rightarrow OCO^* + OH^*$	S-11
$OCOOH^* + OH^* \rightarrow OCO^* + H_2O$	S-12
$OCO^* \rightarrow CO + O^*$	S-13



Cárdenas-Arenas et al. (2021) revealed CO<sub>2</sub> methanation mechanism on Ni/Al<sub>2</sub>O<sub>3</sub> and Ni/CeO<sub>2</sub> catalysts using diffuse reflectance infrared Fourier transform spectroscopy (DRIFTS) experiment. The results showed that CO<sub>2</sub> methanation on the Ni/Al<sub>2</sub>O<sub>3</sub> catalysts follows the formate species (HCOO\*). The CH<sub>4</sub> production on Ni/Al<sub>2</sub>O<sub>3</sub> takes place with CO<sub>2</sub> chemisorption on hydroxyl groups presence bicarbonate (CO<sub>3</sub>H\*) group band at 150 °C, which slowly decreases along with HCOO\* increasing and they are got negative group bands at 350 °C. In contrast with the behavior of Ni/CeO<sub>2</sub>, the HCOO\* are not shown in DRIFTS result. The spectrum of this catalyst shows bidentate carbonates and monodentate carbonates at 150 °C and disappear under reaction conditions [58].

Ren et al. (2015) reported that the best mechanism for CO<sub>2</sub> methanation over Ni(111) surface by density functional theory (DFT) is  $\text{CO}_2 \rightarrow \text{CO} + \text{O} \rightarrow \text{C} + \text{O} + 4\text{H} \rightarrow \text{CH}_2 + 2\text{H} \rightarrow \text{CH}_3 + \text{H} \rightarrow \text{CH}_4$ , that starts with CO<sub>2</sub> dissociation into CO and O, CO decomposition into C and O species and C species hydrogenation to form CH<sub>4</sub> [59].

Jia et al. (2019) proposed CO<sub>2</sub> methanation mechanism over plasma decomposed Ni/ZrO<sub>2</sub> (Ni/ZrO<sub>2</sub>-P) catalysts compared with Ni/ZrO<sub>2</sub> catalysts synthesis via incipient wetness impregnation method (Ni/ZrO<sub>2</sub>-C) using the Operando DRIFT calculation. The results showed that the Ni/ZrO<sub>2</sub>-P catalysts produced CH<sub>4</sub> via the CO-hydrogenation route and formate-hydrogenation route via Ni/ZrO<sub>2</sub>-C catalysts. According to route of CO<sub>2</sub> hydrogenation over Ni/ZrO<sub>2</sub>-P catalysts, there are two possible routes. First route is CO<sub>2</sub> reacts with OH groups on surface of supports to produce bidentate bicarbonates, while H<sub>2</sub> is dissociated into H atom on Ni active phase. These H atoms react with (bi)carbonates to produce bidentate formate and water. Another route is CO<sub>2</sub> reacts with adsorbed O<sup>2-</sup> that formed by CO<sub>2</sub> chemisorption and dissociation to produce monodentate carbonates, then react with H atom to produce monodentate formates and water. After that, the formates are transformed into adsorbed CO, and hydrogenated to build CH<sub>4</sub>. About Ni/ZrO<sub>2</sub>-C catalysts that take place HCOO\* route, it is similar to the first route mechanism over Ni/ZrO<sub>2</sub>-P, but HCOO\* are hydrogenated to CH<sub>4</sub> directly not present in CO intermediate [60].

Baraj et al. (2016), Low (2020), and Jalama (2017) reported the CO<sub>2</sub> methanation mechanism via carbon intermediate mechanism shown in Table 3 that proposed in 12 steps. The first step of CO<sub>2</sub> hydrogenation is both dissociation and adsorption of H<sub>2</sub> to hydrogen atom (H) and CO<sub>2</sub> to CO and oxygen (O) atoms arising carbonyl species (CO\*) (steps 1–3). The CO\* adsorbed on the active site further dissociates into C\* and O\* (step 4), subsequently the C\* reacts with hydrogen atom to produce HC\*, methanediyl (CH<sub>2</sub>\*), methyl (CH<sub>3</sub>\*), and finally converting into methane (steps 5–9). The oxygen atom is hydrogenated to form water (steps 10–12)[61-64].

Table 3. Propose mechanism via carbon intermediate [61-64]

Reaction steps	Step
$H_2 + 2^* \rightarrow 2H^*$	S-1
$CO_2 + 2^* \rightarrow CO^* + O^*$	S-2
$CO^* \rightarrow CO + ^*$	S-3
$CO^* + ^* \rightarrow C^* + O^*$	S-4
$C^* + H^* \rightarrow CH^* + 4^*$	S-5
$CH^* + H^* \rightarrow CH_2^* + 4^*$	S-6
$CH_2^* + H^* \rightarrow CH_3^* + 4^*$	S-7
$CH_3^* + H^* \rightarrow CH_4^* + 4^*$	S-8
$CH_4^* \rightarrow CH_4 + ^*$	S-9
$O^* + H^* \rightarrow OH^* + ^*$	S-10
$OH^* + H^* \rightarrow H_2O + ^*$	S-11
$H_2O + ^* \rightarrow H_2O + ^*$	S-12

Table 4. Propose mechanism via formyl intermediate [64]

Reaction steps	Step
$CO_2 + 2^* \rightarrow CO^* + O^*$	S-1
$H_2 + 2^* \rightarrow 2H^*$	S-2
$CO^* + H^* \rightarrow CHO^* + ^*$	S-3
$CHO^* + ^* \rightarrow CH^* + O^*$	S-4
$CH^* + 3H^* \rightarrow CH_4^* + 3^*$	S-5
$CH_4^* \rightarrow CH_4 + ^*$	S-6
$O^* + H^* \rightarrow OH^* + ^*$	S-7
$OH^* + H^* \rightarrow H_2O + ^*$	S-8
$H_2O + ^* \rightarrow H_2O + ^*$	S-9

Although numerous efforts have been done, the reaction mechanism is ambiguous. It is probably because the different catalyst used, different types of reactor used and different reaction conditions such as temperature and partial pressure influences on different purpose CO<sub>2</sub> methanation mechanism [65]. As for the above reviews, the CO<sub>2</sub> methanation over supported Ni catalysts usually undergoes formate intermediate using FTIR measurement or/and DFT calculation to propose mechanisms. The possible species were displayed in the FTIR result, as shown in Figure 5.

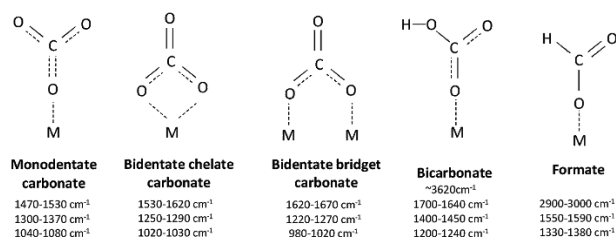


Figure 5. Carbon species and adsorption regions in infrared spectra [58]

## 2.11. Kinetic study

Although kinetics models for CO<sub>2</sub> methanation have been published since Binder and White (1950), the reaction mechanism, surface intermediates, and RDS of this reaction are still debatable [65]. The rate equations for heterogeneous catalyst at surface catalyst were derived with different adsorb mechanisms.

**Monomolecular mechanism:** This is the simplest mechanism derived based on assumptions of one reactant A to produce one product B. Furthermore, reactant A exhibits adsorption on the surface of catalyst as Langmuir isotherm. The derived equation of monomolecular mechanism is shown in Eq.2.9.

$$r = \frac{k_s K_{ads,A} p_A}{1 + K_{ads,A} p_A} \quad \text{Eq. 2.9}$$

**Langmuir-Hinshelwood mechanism:** This mechanism is widely used to explain the kinetics of heterogeneous catalyst. The assumption to derive the equation is both reactants (A and B) adsorbed on the equilibrium surface. Prins (2018) derived elementary rate equation in assumption of catalytic reaction between adsorbed reactant A and B to produce product C and D showing in Eq.2.10 [66].

$$r = k_s \theta_A \theta_B = k_s \frac{K_{ads,A} K_{ads,B} p_A p_B - K^{-1} K_{ads,C} K_{ads,D} p_C p_D}{(1 + K_{ads,A} p_A + K_{ads,B} p_B + K_{ads,C} p_C + K_{ads,D} p_D)^2} \quad \text{Eq. 2.10}$$

**Eley-Rideal mechanism [66]:** This expression equation was derived by the following assumptions. The adsorbed reactant A reacts with non-adsorbed reactant B to produce product C. The basically derived rate equation for the Eley-Rideal mechanism was demonstrated in Eq.2.11 [67].

$$r = k_s \theta_A p_B = k_s \frac{K_{ads,A} p_A p_B}{1 + K_{ads,B} p_B} \quad \text{Eq. 2.11}$$

**Power law model [68]:** Three cases can be discerned: (a) RDS is a hydrogen-assisted dissociation of CO [17]; (b) the RDS is the formation of an oxygen-containing intermediate [18]; (c) the RDS is hydrogenolysis of the oxygen-containing intermediate [19]. All the kinetic models just mentioned leading to an approximate power rate law.

$$r = k_s p_A^\alpha p_B^\beta \quad \text{Eq. 2.12}$$

Several published kinetics are based on Langmuir-Hinshelwood or power law approach. Chiang and Hopper (1983) studied the kinetics of the CO<sub>2</sub> hydrogenation to methane using 58% Ni/kieselguhr catalysts and conducted in a continuous-flow tubular reactor system with a fluidized sand bath to maintain a temperature. They compared the power law rate equation (PL) with a Langmuir–Hinshelwood–Hougen–Watson (LHHW) adsorption type model, and they found that PL is more valuable because of the simplicity [69].

Table 5. CO<sub>2</sub> methanation over supported Ni catalysts rate equations proposed

Rate equations	Kinetic approaches	Ref
$r_{CH_4} = \frac{kP_{H_2}^{0.5}P_{CO_2}^{1/3}}{(1+K_{H_2}P_{H_2}^{0.5}+K_{CO_2}P_{CO_2}^{0.5})^2}$ : Differential reactor	LH	[72]
$r_{CH_4} = \frac{kP_{H_2}^{0.5}P_{CO_2}^{1/3}}{(1+K_{H_2}P_{H_2}^{0.5}+K_{CO_2}P_{CO_2}^{0.5}+K_{H_2O}P_{H_2O})^2}$ : Integral reactor		
$r_{CH_4} = \frac{kP_{H_2}^{1/3}P_{CO_2}^{0.5}}{(1+K_{H_2}P_{H_2}^{0.5}+K'_{CO_2}P_{CO_2}^{1/3}+K''_{CO_2}P_{CO_2}^{2/3}+K_{H_2O}P_{H_2O})^2}$	LH	[73]
$r_{CH_4} = 1.19 \times 10^6 \exp\left[-\frac{14600}{RT}\right]P_{H_2}^{0.21}P_{CO_2}^{0.66}$	PL	[69]
$r_{CH_4} = \frac{\left(\frac{K_1K_2K_{10}k_4k_{11}}{2}\right)^{0.5}L^2P_{H_2}^{0.5}P_{CO_2}^{0.5}}{\left(1+\left(\frac{2K_2k_4}{K_1K_{10}k_{11}}\right)^{0.5}\frac{P_{CO_2}^{0.5}}{P_{H_2}^{0.5}}+\left(\frac{K_1K_2K_{10}k_{11}}{2k_4}\right)^{0.5}P_{CO_2}^{0.5}P_{H_2}^{0.5}+\frac{P_{CO_2}}{K_3}\right)^2}$	LH	[70]
$r_{CH_4} = \frac{kP_{H_2}^{0.5}P_{CO_2}^{0.5}\left(1-\frac{P_{CH_4}P_{H_2O}^2}{K_{eq}P_{CO_2}P_{H_2}^4}\right)}{\left(1+\sqrt{K_{H_2}P_{H_2}}+K_{mix}P_{CO_2}^{0.5}+K_{H_2O}P_{H_2O}\right)^2}$	LHHW	[64]
$r_{CH_4} = \frac{k_1K_{HCOO}P_{CO_2}K_{H_2}^{0.5}P_{H_2}^{0.5}\left(1-\frac{P_{CH_4}P_{H_2O}^2}{K_{eq}P_{CO_2}P_{H_2}^4}\right)}{\left(1+K_{HCOO}P_{CO_2}\sqrt{K_H P_{H_2}}+\sqrt{K_{H_2}P_{H_2}}+K_{OH}\frac{P_{H_2O}}{\sqrt{P_{H_2}}}\right)^2}$	LH	[65]
$r_{CH_4} = \frac{kP_{H_2}^{0.5}P_{CO_2}^{0.5}}{\left(1+K_{OH}\frac{P_{H_2O}}{P_{H_2}^{0.5}}\right)^2}\left(1-\frac{P_{CH_4}P_{H_2O}^2}{P_{CO_2}P_{H_2}^4K_{eq}}\right)$	-	[71]
$r_{CH_4} = \frac{a_{II}P_{H_2}^{0.5}P_{CO_2}^{0.5}}{\left(1+b_{II}\left(\frac{P_{CO_2}}{P_{H_2}}\right)^{0.5}+c_{II}P_{CO_2}^{0.5}P_{H_2}^{0.5}+d_{II}P_{H_2}\right)^2}$	LH	[74]
$r_{CH_4} = \frac{k_4K_1^{0.5}K_2K_3P_{CO_2}P_{H_2}^{0.5}}{\left(1+\frac{k_4K_1^{0.5}K_2K_3}{k_6}P_{CO_2}P_{H_2}^{-0.5}\right)^2}$	LH	[56]
$r_{CH_4} = \frac{kP_{CO_2}^{0.5}P_{H_2}^{3/2}}{(P_{H_2}^{0.5}+K_1P_{CO_2}^{0.5}+K_2P_{H_2}P_{CO_2}^{0.5})^2}$	LH	[75]

In contrast with Weatherbee et al. (1982), who observed the kinetic on CO<sub>2</sub> methanation using Ni/SiO<sub>2</sub> catalysts. Kinetic equations for the methanation of CO<sub>2</sub> were proposed using Langmuir-Hinshelwood (LH) and PL. The results showed that LH rate expression was more fitting to experimental data. They also realized that the rate of CO<sub>2</sub> hydrogenation is sensitive to reaction conditions with the low partial pressure of CO<sub>2</sub> and H<sub>2</sub>, while reaction order is zero order with respect to H<sub>2</sub> [70]. According to Hernandez Lalinde et al. (2020), who chose LH type approach to learn kinetics of CO<sub>2</sub> methanation over Ni/Al<sub>2</sub>O<sub>3</sub> catalysts using packed bed reactors. The LH rate equations were derived based on three different mechanisms, direct

dissociation ( $\text{CO}^*$  intermediated), hydrogen assisted dissociation ( $\text{COH}^*$  or  $\text{HCOO}^*$  intermediated), and a combination of two mechanisms. As for the results, hydrogen assisted dissociation is in excellent agreement with the experimental data [65]. Similarly, Miguel et al. (2018) compared the rate equation via three following literature mechanisms. They found that the formyl species ( $\text{COH}^*$ ) mechanism showed an excellent fit to the experimental data [71]. The published kinetic models were expressed in Table 5.

## 2.12. Reactor for kinetic study

Two reactor types can be used for methanation reactions. There are two-phase fixed bed reactors and fluidized bed reactors [76]. The fluidization of catalyst particles in fluidized bed reactors results in high mechanical stress of the particles and reactor walls, leading to catalyst loss and shorter reactor life [27]. Then, a fixed bed reactor is mainly used in  $\text{CO}_2$  methanation. For investigated kinetics of the reaction, type of reactors can categorize into the differential reactor and integral reactor. The differential reactor is used to study kinetic with low product concentration [77] and a few grams of catalyst [78]. The differential reactor is usually diluted reactants fed with 90% inert gas and diluted catalysts with inactive catalysts to prevent excessive temperature [78]. In contrast, the integral reactor operates at a thick catalyst with a high concentration of products [79, 80]. Therefore, it is emphasized in the industrial section for  $\text{CO}_2$  methanation reaction [81]. Another advantage of the integral reactor is easy to install, but it is challenging to observe the kinetics of reaction because the reaction mechanism changes with changing temperature along the length of the reactor [82].

A few studies have been done kinetic experiments by using differential reactors. Dry et al. (1972) studied Fisher-Tropsch reaction over iron catalysts in the differential reactor. The initial gases were fed in the reactor, including  $\text{H}_2/\text{CO}$  molar ratio (1/1 to 7/1) containing 12%  $\text{CH}_4$  and 0.7%  $\text{CO}_2$  [83]. According to Lunde and Kester (1974), who investigated  $\text{CO}_2$  methanation on a Ru catalyst in differential reactor. The inlet gases with followed factitious  $\text{CO}_2$  conversion were fed at 0 to 0.85 with molar ratios 2/1 to nearly 4/1 of  $\text{H}_2/\text{CO}_2$ , and reaction temperatures of 204 to 370 °C were investigated [84]. Researchers indicate differential reactor by percent of conversion, which either study reported different value. Lim et al. (2020) said that  $\text{CO}_2$  methanation was conducted in the range of  $\text{CO}_2$  conversion below 15% [85], consistent with Karemore et al. (2021) [86]. Lower than that, Pandey et al. (2018) reported below 8% [87]. The lowest conversions during kinetic tests were kept at a lower than 1% [88, 89].

For integral reactor, Zhao et al. (2012) focused on syngas methanation over  $\text{Ni}/\text{Al}_2\text{O}_3$  catalysts using a fixed-bed integral reactor. The catalysts were operated at over 140 mm of temperature zone, 500 mg of catalyst loading was diluted with inert

$\text{Al}_2\text{O}_3$ , and  $100 \text{ mLmin}^{-1}$  of total gas flow rate. More than 90% of conversions were received in this study [90]. Barrientos et al. (2016) estimated rate constant of CO methanation reaction in the integral reactor. The 50–100 mg of catalyst loading diluted with 5 g of SiC was carried out in a fixed bed reactor with the total gas flow equal to  $15 \text{ NLh}^{-1}$  and 3/1 of  $\text{H}_2/\text{CO}$  molar ratio. The results showed that conversions of CO over Ni/ $\gamma\text{-Al}_2\text{O}_3$  were lower than 50% [91]. Similar reaction to Irankhah et al. (2007), they deserved the CO conversion around 50–70% over cobalt supported catalysts in supercritical phase [92]. Hadjigeorghiou and Richardson (1986) reported an integral reactor in Fischer-Tropsch synthesis over Ni/ $\text{Al}_2\text{O}_3$  catalysts to appear in temperature reaction above  $267 \text{ }^\circ\text{C}$  to get CO conversion over 90% [93].

Whereas the differential and integral reactors were reported in different limitations, a few publish were publicized in combined reactors to estimate the kinetic parameters. Kai, Forusaki, and Yamamoto (1984) studied the kinetics of CO methanation over Ni/ $\text{Al}_2\text{O}_3$  catalysts using differential and integral reactors. Both reactor tests were carried out with diluted catalysts by inactive alumina particles. In the differential reactor study, measurements kept  $\text{CO}_2$  conversion less than 1% by diluting partial pressure of reactants ( $\text{CO}_2$  and  $\text{H}_2$ ) with nitrogen gas. The  $\text{H}_2/\text{CO}_2$  molar ratio in differential reactor study is 1.2/1 and 16/1. Determinations in the integral reactor were related at  $\text{H}_2/\text{CO}_2$  molar ratio is 1.3/1 to 5/1 with a high and wide range of conversion [89]. Four years later, Kai and Takahashi researched a similar study. They focused on the kinetics of  $\text{CO}_2$  methanation over Ni/ $\text{La}_2\text{O}_3$  catalysts. The differential reactor study is kept  $\text{CO}_2$  conversion less than 3% with diluting nitrogen gas in reaction owing to changing partial pressure of reactants, and the molar ratio of  $\text{H}_2/\text{CO}_2$  was 0.6/1 to 30/1. In the integral reactor study, the  $\text{CO}_2$  methanation reaction was performed at a molar ratio of 4 without diluting nitrogen gas [72]. Karemore et al. (2021) used two reactors for different influence studies over Ni–K/ $\text{CeO}_2\text{-Al}_2\text{O}_3$  catalyst, the reaction condition in an integral reactor is  $\text{CH}_4/\text{H}_2\text{O}/\text{CO}_2$  equal to 3/2/1, space-time ( $W/Q_0$ ) between 0.08 and  $0.33 \text{ ghL}^{-1}$ , and 0.2–0.5 mol/mol of steam to carbon ratio. In the differential reactor, influence of the partial pressures ( $\text{CH}_4$ ,  $\text{H}_2\text{O}$ , and  $\text{CO}_2$ ) was investigated with diluting by 72 %  $\text{N}_2$ . The data were evaluated kinetic by Power law rate equation [86].

### 2.13. Related literatures

Weatherbee and Bartholomew [70] studied kinetics and mechanism of  $\text{CO}_2$  methanation over 3wt%Ni/ $\text{SiO}_2$  catalyst. Experimental data were achieved under reaction temperature of 226 to  $326 \text{ }^\circ\text{C}$  and low pressure 0.14 to 0.175 MPa using an isothermal differential tubular reactor with 1 cm inner diameter.  $\text{CO}_2$  conversion was emphasized at less than 10%. They realized that the data suited Langmuir-Hinshelwood (LH) with a  $\text{CO}_2$  dissociated to carbon mechanism.

Chiang and Hopper [69] emphasized the kinetics of the CO<sub>2</sub> hydrogenation to methane over 58%Ni/kieselguhr catalyst using a continuous-flow tubular reactor with a fluidized sand bath maintaining a temperature. The kinetic characterizations were investigated between reaction temperature 278 to 317 °C and a total pressure range from 1.16 to 1.82 MPa with a constant catalyst weight of 15 mg. The results showed that the power law model is the best described kinetics because of the uncomplicated mechanism.

Kai and Takahashi [72] Ni-La<sub>2</sub>O<sub>3</sub> catalyst no effects of pore diffusion were observed. The catalyst particles were diluted by inert alumina in the same particle size to avoid a temperature rise due to the heat of the reaction. Kinetic data for the methanation of CO<sub>2</sub> were obtained using differential and integral reactors. The measurements were carried out in the differential reactor study while keeping CO<sub>2</sub> conversions less than 3 %. The partial pressure was varied by diluting the feeds with N<sub>2</sub>. The molar ratio of H<sub>2</sub>/CO<sub>2</sub> was varied between 0.6 and 30. In the integral reactor study, the non-diluted gases were fed with a molar ratio of 4. For both types of reactor tests, the temperature was studied between 513 K and 593 K.

Koschany, Schlereth, and Hinrichsen [64] compared two approaches of kinetic rate equations, power law and Langmuir–Hinshelwood–Hougen–Watson (LHHW) models. The NiAl(O)<sub>x</sub> catalysts diluted with purified SiC in the catalyst-to-SiC ratio of 1/9 were conducted in a differential-integral fixed bed reactor. The kinetic data were observed with catalysts loading of 25 mg in the temperature range of 250 to 340 °C, and 75 mg between 180 and 240 °C with different feed ratios of H<sub>2</sub>/CO<sub>2</sub>/CH<sub>4</sub>/H<sub>2</sub>O/Ar. The results showed that the power law rate equations were not suitable for Koschany's study because the reaction rate was overestimating while the larger amounts of product gases were present. These equations are probably more suitable for the differential conversion in the vary low product gases process. For LHHW, the data are predicted very well with the LHHW model, and rate equations can be reflected from the differential to almost complete conversion for all reaction conditions applied in this study. So, LHHW rate equations are fitted to describe the kinetics compared to PL rate equations.

Marocco et al. [94] followed the kinetic models from Koschany et al. [64]. The kinetic studies were focused on Ni/Al hydrotalcite catalyst over a differential reactor. The experimental conditions were carried out at temperatures of 270–390 °C, atmospheric pressure, and total flow rates of 200 and 300 mL/min. The catalyst was diluted by inert SiO<sub>2</sub> in the ratio of 1/3 (active/inactive catalyst) to suppress the temperature rise caused by the naturally exothermic reaction. The results demonstrated the the combination of power law and LHHW models showed better fitting with inhibiting influence adsorption of water and formyl formation as RDS.

Champon et al. [75] considered a single step (Sabatier reaction) and second steps (combination between RWGS and CO methanation) in the absence of transport limitation. Kinetics over commercial 14–17%wt Ni/Al<sub>2</sub>O<sub>3</sub> catalyst were studied in the isothermal plug-flow reactor at temperatures of 350 to 450 °C and atmospheric pressure. At first, the reaction orders were determined from kinetic data obtained from

differential mode. Then, the kinetic parameters were estimated using data obtained from the integral and differential conditions by applying the ideal plug flow reactor (PFR) model.

Lalinde et al. [65] derived kinetic models for CO<sub>2</sub> methanation and RWGS reactions from the LH approach. The kinetic experiments were conducted at 320–420 °C, total pressures of 0.1–0.7 MPa, and 50–150 mL/min flow rates with 30 wt% Ni/Al<sub>2</sub>O<sub>3</sub> catalyst loadings at 77 to 113 mg. They found that the suitable model to describe the kinetics over this catalyst was a hybrid mechanism between CO intermediate and formyl intermediated with dissociation of formyl as RDS.

This work aims to determine kinetic parameters and predict the mechanism of CO<sub>2</sub> methanation reaction over commercial catalyst using an isothermal differential fixed bed reactor without diffusional limitation.





## CHAPTER III

### RESEARCH PROCEDER

#### 3.1. Kinetic measurements

A commercial catalyst, 17–23%wt Ni/SiO<sub>2</sub> provided by GL science (1050-12100), was used for the kinetic studies. The catalyst contains 17–23% Ni and 34–42% NiO. Note that Ni is not the only metal in the catalyst. CuO is also dispersed, although the concentration is low at 2%. Other components are 24–28% SiO<sub>2</sub> and water content. The 20 mg Ni/SiO<sub>2</sub> catalyst was diluted with inactive  $\gamma$ -Al<sub>2</sub>O<sub>3</sub> particles of 180 mg. Particles were sieved to 212–300  $\mu$ m and filled in the center of a tubular quartz tube inner diameter of 5 mm. After that, the catalyst was reduced to transform nickel oxide (NiO) into Ni<sup>0</sup> with a flow H<sub>2</sub>/Ar mixture at 200 mL/min. It was kept at 500 °C for 5 h to reduce the catalyst completely. Then, in order to prevent the deactivation of the catalyst during the kinetic test, the catalyst was aged at atmospheric pressure and 500 °C for 35 h with flow of H<sub>2</sub>/CO<sub>2</sub>/CH<sub>4</sub>/H<sub>2</sub>O/Ar mixture at the equilibrium state. The total flow rate was kept at 200 mL/min. Stable activity during the kinetic tests was observed by monitoring it before and after each measurement set at reference points (300–350 °C, H<sub>2</sub>/CO<sub>2</sub>/Ar = 4/1/5). To design a differential reactor, the effect of temperature, total flowrate, dilution of catalyst should be considered. In a preliminary work, the conditions for kinetic measurements were determined as total flow rate of 200 mL/min at 300–350 °C. Initial feed composition was determined by following the stoichiometry of the Sabatier reaction (H<sub>2</sub>/CO<sub>2</sub> = 4/1, CH<sub>4</sub>/H<sub>2</sub>O = 1/2) at  $X'_{CO_2}$  equal to 0–0.7. Non-stoichiometric H<sub>2</sub>/CO<sub>2</sub> ratios of 1/1, 2/1 and 5/1 were also considered to estimate reaction orders, followed by addition of methane and steam at H<sub>2</sub>/CO<sub>2</sub>/CH<sub>4</sub>/H<sub>2</sub>O/Ar = 1/1/0.4/0.8/0.8 and 1/1/0.4/1.2/0.4. The gases were diluted by argon to constrain CO<sub>2</sub> conversion and eliminate transport phenomena. The conditions for kinetic measurements are shown in Table 6.

Table 6. Experimental condition for kinetic study

ID	Flowrate (mL/min)	Stoichiometric composition				Temperature (°C)	Pressure (MPa)
	H <sub>2</sub>	CO <sub>2</sub>	CH <sub>4</sub>	H <sub>2</sub> O	Ar		
01	80	20	0	0	100	300–350	0.1–0.9
02	112	28	0	0	60		
03	144	36	0	0	20		
04	108	27	19	38	8		
05	80	20	20	40	40		
06	80	20	30	60	10		
07	64	16	37	74	9		
		Non-stoichiometric composition					
08	50	50	0	0	100	300–350	0.1–0.9
09	75	75	0	0	50		
10	40	20	0	0	140		
11	66.7	33.3	0	0	100		
12	125	25	0	0	50		
13	50	50	20	40	40		
14	50	50	20	60	20		

### 3.2. Reactor operation

The process flow diagram for CO<sub>2</sub> methanation process is shown in Figure 6. Firstly, the gases (CO<sub>2</sub>, H<sub>2</sub>, CH<sub>4</sub>, and Ar) and water were fed into the evaporator that contained the glass beads, and it was heated at 200 °C to vaporize the water and preliminary heat of mixed gas. The gases were controlled by mass flow controllers (HM1000B MFCs from HEMMI Slide Rule CO., Ltd) and the liquid water was fed by liquid pump (NP-KX-201 series). To prevent the condensing, the stainless-steel line was wrapped by insulation to maintain the temperature at 200 °C from the downstream of evaporator to upstream of reactor. The mixed gases and water vapor were induced in the tubular quartz tube reactor, which was covered by a stainless-steel tube with a gap to allow pressurization. As for the temperature measurement, there are 11 thermocouples were installed in the apparatus, as shown in Appendix F, including thermocouples at evaporator, downstream of evaporator, upstream and downstream of the reaction zone, and the others for GC part. However, three temperatures were investigated and shown in the monitor in real-time. The first thermocouple located in the center of furnace was used to set the furnace temperature. Another thermocouple was installed at the bottom of catalyst bed, which was inserted passing through the milli-hold at the center of sinter filter to prevent heating loss from thermocouple measurement. The temperature from this located thermocouple was called “T<sub>bottom</sub>”,

and the last thermocouple was installed on the top of catalyst bed (so-called “ $T_{top}$ ”). These two were monitored to investigate the characteristic of isothermal reactor. The accepted different temperature of the upper part and the bottom part of catalyst bed for isothermal reactor is  $5^{\circ}\text{C}$ . Besides the temperature monitoring, the pressure was observed upstream of the catalyst bed and shown at the same monitor. The pressure was controlled by closing the needle valve and adjusting the back-pressure valve downstream of the reaction part. The catalyst was kept at each condition for 40 min to ensure a steady state. The product gases were measured by two gas chromatographs (GC2014, Shimadzu), one (GC1) for detecting the concentration of Ar,  $\text{H}_2$ , CO,  $\text{CH}_4$ ,  $\text{CO}_2$  and the other (GC2) for detecting the  $\text{H}_2\text{O}$  vapor. These were installed with packed columns from Shinwa Chemical Industries Ltd., Shincarbon-ST and Sunpak-A for GC1 and GC2, respectively.

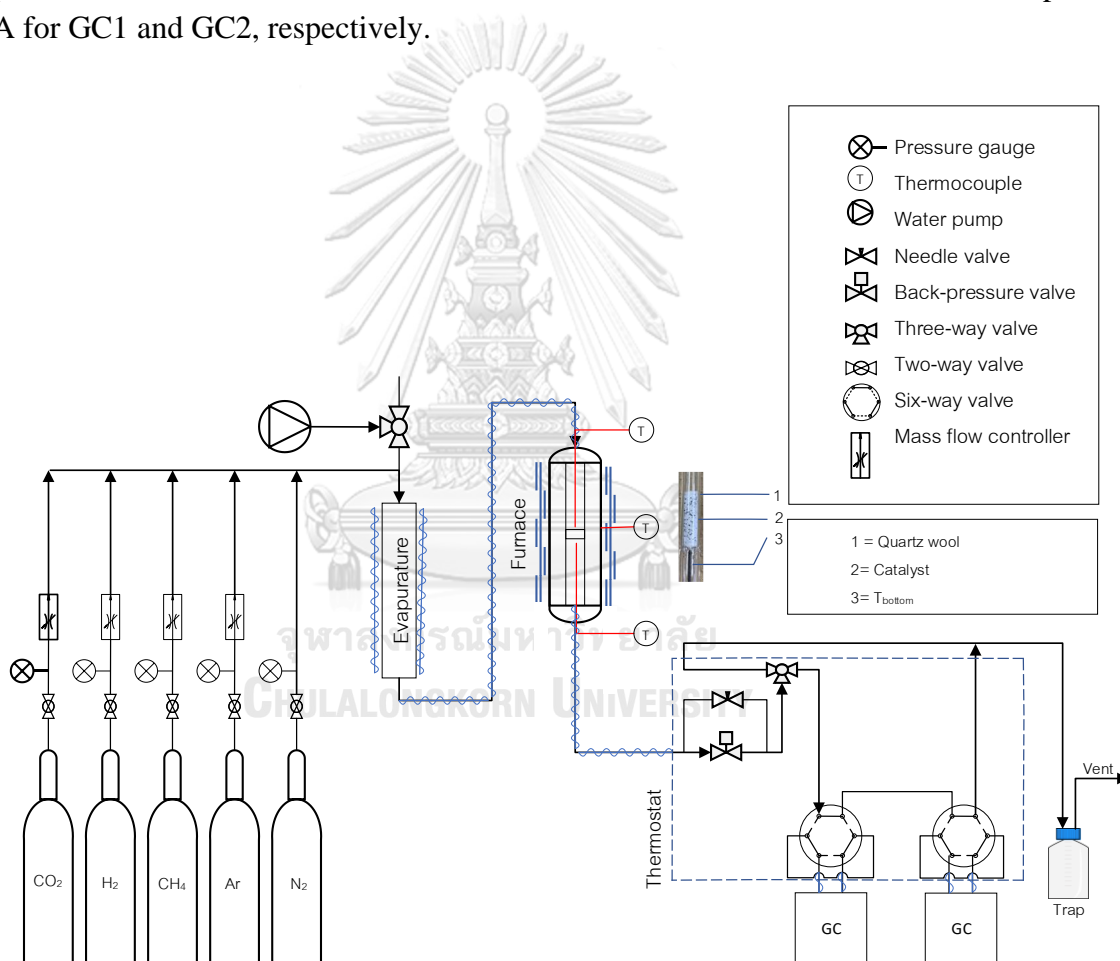


Figure 6. Schematic diagram of the  $\text{CO}_2$  methanation reactor

### 3.3. Assessment of diffusional limitations

The kinetic data must be obtained in the absence of transport limitations to ensure an intrinsic kinetic reaction. Internal and external mass transfer limitations can be theoretically assessed by the Weisz-Prater criteria. Anderson and Mears proposed the criteria for internal and external heat transfer limitations [67], as shown in Table 7. The decreasing particle diameter and diluting with an inert  $\gamma\text{Al}_2\text{O}_3$  catalyst assist in meeting the criteria [95]. The axial and radial dispersion, radial heat transfer limitation, volumetric dilution ratio, and pressure drop were also considered, as shown in Table 8. The axial dispersion can be simply assessed by  $\frac{H}{R_p} > 50$  [95], where  $R_p$  and  $H$  stand for the radius of catalyst particle and catalyst bed height, respectively. The transport limitation assessment is not only calculated from the equation but also evaluated from the experiment [15, 71, 75].

Table 7. Criteria equation to assess transport limitation [67]

	Mass transfer limitation	Heat transfer limitation
Internal particle	$\frac{r_{\text{obs}}R_p^2}{D_{\text{CO}_2,e}C_{\text{CO}_2,s}} < \frac{1}{n}$	$\frac{ \Delta H_r r_{\text{obs}}R_p^2}{\lambda_e T} < 0.75 \frac{RT}{E_a}$
External particle	$\frac{r_{\text{obs}}R_p}{k_g C_{\text{CO}_2,b}} < \frac{0.15}{n}$	$\frac{ \Delta H_r r_{\text{obs}}R_p}{hT} < 0.15 \frac{RT}{E_a}$

Table 8. Criteria equation to assess diffusional limitation [96]

Relative pressure drop over the catalyst bed	$\Delta P < \frac{0.2 P}{n}$
Axial dispersion	$\frac{H}{d_p} > \frac{8}{Bo} n \ln \left\{ \frac{1}{1 - X_{\text{CO}_2}} \right\}$
Radial dispersion	$\frac{d_t}{d_p} > 8$
Inert bed dilution	$b < \frac{1}{1 + \frac{10X_{\text{CO}_2}d_p}{H}}$
Radial heat transfer limitation	$\Delta T_{\text{rad}} = \frac{ \Delta H_r r_{\text{obs}}d_t^2(1 - \varepsilon_b)(1 - b)}{32 \lambda_{er}} < 0.05 \frac{RT^2}{E_a}$

### 3.4. Parameter estimation and kinetic equation

The power law models for the Sabatier reaction were taken from Koschany et al. [64], as shown Eqs. 3.1, 3.3, 3.5, and 3.7, and the power law models for RWGS reaction were expressed in Eqs. 3.2, 3.4, 3.6, and 3.8.

Simple power law rate equation (PL)

$$r_1 = k_1 \cdot p_{H_2}^{n_{H_2,1}} p_{CO_2}^{n_{CO_2,1}} \left( 1 - \frac{p_{CH_4} p_{H_2O}^2}{p_{H_2}^4 p_{CO_2} K_{eq,1}} \right) \quad Eq.3.1$$

$$r_2 = k_2 \cdot p_{H_2}^{n_{H_2,2}} p_{CO_2}^{n_{CO_2,2}} \left( 1 - \frac{p_{CO} p_{H_2O}}{p_{H_2} p_{CO_2} K_{eq,2}} \right) \quad Eq.3.2$$

The following parameters should be estimated :

$$k_{1,0,ref}, E_{a,1}, k_{2,0,ref}, E_{a,2}, n_{H_2,1}, n_{CO_2,1}, n_{H_2,2}, n_{CO_2,2}$$

Power law rate equation with inhibiting influence of water (PL-H<sub>2</sub>O)

$$r_1 = k_1 \frac{p_{H_2}^{n_{H_2,1}} p_{CO_2}^{n_{CO_2,1}}}{p_{H_2O}^{n_{H_2O,1}}} \left( 1 - \frac{p_{CH_4} p_{H_2O}^2}{p_{H_2}^4 p_{CO_2} K_{eq,1}} \right) \quad Eq.3.3$$

$$r_2 = k_2 \frac{p_{H_2}^{n_{H_2,2}} p_{CO_2}^{n_{CO_2,2}}}{p_{H_2O}^{n_{H_2O,2}}} \left( 1 - \frac{p_{CO} p_{H_2O}}{p_{H_2} p_{CO_2} K_{eq,2}} \right) \quad Eq.3.4$$

The following parameters should be estimated :

$$k_{1,0,ref}, E_{a,1}, k_{2,0,ref}, E_{a,2}, n_{H_2,1}, n_{CO_2,1}, n_{H_2O,1}, n_{H_2,2}, n_{CO_2,2}, n_{H_2O,2}$$

Power law rate equation with inhibition by adsorbed water (PL-WI)

$$r_1 = k_1 \frac{p_{H_2}^{n_{H_2,1}} p_{CO_2}^{n_{CO_2,1}}}{1 + K_{H_2O} p_{H_2O}} \left( 1 - \frac{p_{CH_4} p_{H_2O}^2}{p_{H_2}^4 p_{CO_2} K_{eq,1}} \right) \quad Eq.3.5$$

$$r_2 = k_2 \frac{p_{H_2}^{n_{H_2,2}} p_{CO_2}^{n_{CO_2,2}}}{1 + K_{H_2O} p_{H_2O}} \left( 1 - \frac{p_{CO} p_{H_2O}}{p_{H_2} p_{CO_2} K_{eq,2}} \right) \quad Eq.3.6$$

The following parameters should be estimated :

$$k_{1,0,ref}, E_{a,1}, k_{2,0,ref}, E_{a,2}, n_{H_2,1}, n_{CO_2,1}, n_{H_2,2}, n_{CO_2,2}, K_{H_2O,0,ref}, \Delta H_{H_2O}$$

Power law rate equation with inhibition adsorbed hydroxyl (PL-HI)

$$r_1 = k_1 \frac{p_{H_2}^{n_{H_2,1}} p_{CO_2}^{n_{CO_2,1}}}{1 + K_{OH} \frac{p_{H_2O}}{p_{H_2}^{0.5}}} \left( 1 - \frac{p_{CH_4} p_{H_2O}^2}{p_{H_2}^4 p_{CO_2} K_{eq,1}} \right) \quad Eq.3.7$$

$$r_2 = k_2 \frac{p_{H_2}^{n_{H_2,2}} p_{CO_2}^{n_{CO_2,2}}}{1 + K_{OH} \frac{p_{H_2O}}{p_{H_2}^{0.5}}} \left( 1 - \frac{p_{CO} p_{H_2O}}{p_{H_2} p_{CO_2} K_{eq,2}} \right) \quad Eq.3.8$$

The following parameters should be estimated :

$$k_{1,0,ref}, E_{a,1}, k_{2,0,ref}, E_{a,2}, n_{H_2,1}, n_{CO_2,1}, n_{H_2,2}, n_{CO_2,2}, K_{OH,0,ref}, \Delta H_{OH}$$

The equation derived from Hernandez Lalinde et al. [65] was taken into account to describe the mechanism. The CO\* intermediated [21, 59, 61-63] and HCOO\* intermediated mechanisms [53, 55-58, 60] was assumed for deriving the LH models because it popularly reported in CO<sub>2</sub> methanation over a Ni-based catalyst. The assumption mechanisms proposed by Lalind and group [65] were demonstrated in Tables 9, 10, and 11 for mechanism A (the CO\* intermediated) , mechanism A (the HCOO\* intermediated) and hybrid mechanism between mechanism A and B, respectively.

Table 9. CO<sub>2</sub> methanation via CO intermediated formation-Mechanism A [65]

Reaction	Description	Step	Reaction
H <sub>2</sub> + 2* ↔ 2H*			A1
CO <sub>2</sub> + * ↔ CO <sub>2</sub> *	RDS	Adsorption of CO <sub>2</sub>	A2
CO <sub>2</sub> * + * ↔ CO* + O*	RDS	Dissociation of CO <sub>2</sub>	A3
CO* + * ↔ C* + O*	RDS	Dissociation of CO to surface C	A4
C* + H* ↔ CH* + *	RDS	Hydrogenation of C	A5
CH* + H* ↔ CH <sub>2</sub> * + *	RDS	Hydrogenation of CH	A6
CH <sub>2</sub> * + H* ↔ CH <sub>3</sub> * + *	RDS	Hydrogenation of CH <sub>2</sub>	A7
CH <sub>3</sub> * + H* ↔ CH <sub>4</sub> * + *		Hydrogenation of CH <sub>3</sub>	A8
CH <sub>4</sub> * ↔ CH <sub>4</sub> (g) + *		Desorption of CH <sub>4</sub>	A9
O* + H* ↔ OH* + *		OH formation	A10
OH* + H* ↔ H <sub>2</sub> O* + *		H <sub>2</sub> O formation	A11
CO* ↔ CO(g) + *		Desorption of CO	A12
H <sub>2</sub> O* ↔ H <sub>2</sub> O(g) + *		H <sub>2</sub> O desorption	A13

Table 10. CO<sub>2</sub> methanation via HCOO intermediated formation-Mechanism B [65]

Reaction	Description	Step	Reaction
$H_2 + 2* \leftrightarrow 2H^*$			B1
$CO_2 + * \leftrightarrow CO_2^*$	RDS	Adsorption of CO <sub>2</sub>	B2
$CO_2^* + H^* \leftrightarrow HCOO^* + *$	RDS	Formation of formates	B3
$HCOO^* + * \leftrightarrow CO^* + OH^*$	RDS	Dissociation of formates to CO	B4
$HCOO^* + H^* \leftrightarrow COH^* + OH^*$	RDS	Dissociation of formates to COH	B5
$COH^* + H^* \leftrightarrow CH^* + OH^*$	RDS	Dissociation of formyl	B6
$COH^* + * \leftrightarrow C^* + OH^*$	RDS	Dissociation of formyl	B7
$CH^* + H^* \leftrightarrow CH_2^* + *$	RDS	Hydrogenation of CH	B8
$CH_2^* + H^* \leftrightarrow CH_3^* + *$	RDS	Hydrogenation of CH <sub>2</sub>	B9
$CH_3^* + H^* \leftrightarrow CH_4^* + *$	RDS	Hydrogenation of CH <sub>3</sub>	B10
$CH_4^* \leftrightarrow CH_4(g) + *$		Desorption of CH <sub>4</sub>	B11
$O^* + H^* \leftrightarrow OH^* + *$		OH formation	B12
$OH^* + H^* \leftrightarrow H_2O^* + *$		H <sub>2</sub> O formation	B13
$H_2O^* \leftrightarrow H_2O(g) + *$		H <sub>2</sub> O desorption	B14
$CO^* \leftrightarrow CO(g) + *$		Desorption of CO	B15

Table 11. CO<sub>2</sub> methanation via hybrid mechanism-Mechanism AB [65]

Reaction	Description	Step	Reaction
$H_2 + 2* \leftrightarrow 2H^*$			AB1
$CO_2 + * \leftrightarrow CO_2^*$		Adsorption of CO <sub>2</sub>	AB2
$CO_2^* + * \leftrightarrow CO^* + O^*$		Dissociation of CO <sub>2</sub>	AB3
$CO^* + H^* \leftrightarrow COH^* + *$	RDS	Formation of formyl	AB4
$CO^* + 2H^* \leftrightarrow COH_2^* + 2*$	RDS	Formation of di-hydrogenated CO	AB5
$COH^* + * \leftrightarrow CH^* + O^*$	RDS	Dissociation of formyl	AB6
$COH^* + H^* \leftrightarrow CH^* + OH^*$	RDS	Dissociation of formyl	AB7
$COH_2^* + * \leftrightarrow CH^* + OH^*$	RDS	Formation of CH species	AB8
$CH^* + H^* \leftrightarrow CH_2^* + *$	RDS	Hydrogenation of CH	AB9
$CH_2^* + H^* \leftrightarrow CH_3^* + *$	RDS	Hydrogenation of CH <sub>2</sub>	AB10
$CH_3^* + H^* \leftrightarrow CH_4^* + *$		Hydrogenation of CH <sub>3</sub>	AB11
$CH_4^* \leftrightarrow CH_4(g) + *$		Desorption of CH <sub>4</sub>	AB12
$O^* + H^* \leftrightarrow OH^* + *$		OH formation	AB13
$OH^* + H^* \leftrightarrow H_2O^* + *$		H <sub>2</sub> O formation	AB14
$H_2O^* \leftrightarrow H_2O(g) + *$		H <sub>2</sub> O desorption	AB15
$CO^* \leftrightarrow CO(g) + *$		Desorption of CO	AB16

The models were derived based on LH adsorption type and all models can be summarized in one generalized form, see in Eq.3.9, which the 20 different sets of exponents are shown in Table 12. The mechanism assumptions were described later.

$$r_1 = \frac{k_1 \cdot K_{Ae} p_{CO_2}^a K_{H_2}^b p_{H_2}^c p_{H_2O}^d \left(1 - \frac{p_{CH_4} p_{H_2O}^2}{p_{CO_2} p_{H_2}^4 K_{eq,1}}\right)}{\left(1 + K_{Ae} p_{CO_2}^e K_{H_2}^f p_{H_2}^g p_{H_2O}^h + K_{H_2}^{0.5} p_{H_2}^{0.5} + K_{OH} \frac{p_{H_2O}}{p_{H_2}^{0.5}}\right)} \quad Eq.3.9$$

The following parameters should be estimated :

$$k_{1,0,ref}, E_{a,1}, K_{Ae,0,ref}, \Delta H_{Ae}, K_{H_2,0,ref}, \Delta H_{H_2}, K_{OH,0,ref}, \Delta H_{OH}$$

Table 12. Exponents of Eq.3.9.

NO.	Mech	$K_{Ae}$	$a$	$b$	$c$	$d$	$e$	$f$	$g$	$h$	$i$
1	A, AB, B	–	1.0	–	–	–	–	–	–	–	1.0
2	A, AB, B	–	1.0	–	–	–	–	–	–	–	2.0
3	A3, AB3	$K_{CO_2}$	1.0	–	–	–	1.0	–	–	–	2.0
4	A4	$K_{CO}$	0.5	–	–	–	0.5	–	–	–	2.0
5	A5	$K_C$	0.33	0.5	0.5	–	0.33	–	–	–	2.0
6	A6	$K_{CH}$	0.33	1.0	1.0	–	0.33	0.5	0.5	–	2.0
7	A7	$K_{CH_2}$	0.33	1.5	1.5	–	0.33	1.0	1.0	–	2.0
8	AB4	$K_{CO}$	0.5	0.5	0.5	–	0.5	–	–	–	2.0
9	AB5	$K_{CO}$	0.5	1.0	1.0	–	0.5	–	–	–	3.0
10	AB6	$K_{COH}$	0.5	0.5	0.5	–	0.5	0.5	0.5	–	2.0
11	AB7	$K_{COH}$	0.5	1.0	1.0	–	0.5	0.5	0.5	–	2.0
12	AB8	$K_{COH_2}$	0.5	1.0	1.0	–	0.5	1.0	1.0	–	2.0
13	AB9	$K_{CH}$	0.25	1.0	1.0	–	0.25	0.5	0.5	–	2.0
14	AB10	$K_{CH_2}$	0.25	1.5	1.5	–	0.25	1.0	1.0	–	2.0
15	B4	$K_{HCOO}$	1.0	0.5	0.5	–	1.0	0.5	0.5	–	2.0
16	B5	$K_{HCOO}$	1.0	1.0	1.0	–	1.0	0.5	0.5	–	2.0
17	B6	$K_{COH}$	1.0	1.5	2.0	–1.0	1.0	1.0	1.5	–1.0	2.0
18	B7	$K_{COH}$	1.0	1.0	1.5	–1.0	1.0	1.0	1.5	–1.0	2.0
19	B8	$K_{CH}$	1.0	2.0	3.0	–2.0	1.0	1.5	2.5	–2.0	2.0
20	B9	$K_{CH_2}$	1.0	2.5	3.5	–2.0	1.0	2.0	3.0	–2.0	2.0

The subscript “1“ and “2“ in Eqs. 3.1 to 3.9 stand for Sabatier and RWGS reactions, respectively. The reaction rate constants of reaction  $i$  ( $k_1$  and  $k_2$ ) were replaced by the Arrhenius equation, as shown in Eq.3.10. The Adsorption equilibrium constants of component  $j$  ( $K_{H_2O}$ ,  $K_{OH}$ ,  $K_{Ae}$ ,  $K_{H_2}$ ) expressed in the Vant't Hoff equation ( Eq.3.11).  $p_j$  and  $n_{j,i}$  stand for partial pressure and reaction order.

$$k_i = k_{i,0,ref} e^{\left(\frac{E_{a,i}}{R} \left(\frac{1}{T_{ref}} - \frac{1}{T}\right)\right)} \quad Eq.3.10$$

$$K_j = K_{j,0,ref} e^{\left(\frac{\Delta H_j}{R} \left(\frac{1}{T_{ref}} - \frac{1}{T}\right)\right)} \quad Eq.3.11$$



$k_{i,0,ref}$  and  $K_{j,0,ref}$  represent pre-exponential factors or frequency factors at referent temperature.  $E_{a,i}$  and  $\Delta H_j$  are the activation energy of reaction  $i$  and enthalpy change of adsorption of component  $j$ , respectively. The equilibrium constant of Sabatier reaction ( $K_{eq,1}$ ) followed Koschany et al. [64], as given in Eq.3.12. As for the equilibrium constant of RWGS ( $K_{eq,2}$ ), it is possible calculated from rewest of the equilibrium constant of WGS reaction reported by Aparicio [97] and Smith et al. [98], as demonstrated in Eq.3.13 and 3.14.

$$K_{eq,1} = 137T^{-3.998} e^{\frac{158.7kJ/mol}{RT}} \quad Eq.3.12$$

$$K_{eq,WGS} = 9.01 \times 10^{-6} T^{0.968} e^{\frac{43.6 kJ/mol}{RT}} \quad Eq.3.13$$

$$K_{eq,2} = 1/K_{eq,WGS} \quad Eq.3.14$$

Parameters were estimated using the lmfit package from Python software, and the least-square method was applied to minimize the residual value. The lmfit package is applicable for complex models. Code for parameter estimation was expressed in Apendix E.

### 3.5. Model discrimination and thermodynamic consistency

Model discrimination was assessed by thermodynamic consistency of estimated kinetic parameter, statistically significant and adequacy fitting of kinetic model. The satisfaction of overall rate equation was test by the AIC and BIC with 95% confidence interval. AIC and BIC stand for Akaike information criterion and Bayesian information criterion, respectively. The AIC can be directly calculated from Eq.3.15 [99].

$$AIC = 2k + n \ln\left(\frac{\sum_{i=1}^n [r_{i,exp} - r_{i,pred}]^2}{n}\right) \quad Eq.3.15$$

In case  $n/k < 40$ , the correction term must be complied, as shown in Eq.3.16, where  $n$  and  $k$  stand for number of sample and number of parameters, respectively.

$$AIC = 2k + n \ln\left(\frac{\sum_{i=1}^n [r_{i,exp} - r_{i,pred}]^2}{n}\right) + \frac{2k(k+1)}{n-k-1} \quad Eq.3.16$$

BIC is similar to AIC derived from the same assumption, which depends on  $n$  and  $k$ .

$$BIC = k \ln n + n \ln \left( \frac{\sum_{i=1}^n [r_{i,exp} - r_{i,pred}]^2}{n} \right) \quad Eq.3.17$$

Where  $r_{i,exp}$  is reaction rate values obtained from the experiment and  $r_{i,pred}$  represents reaction rate values from prediction. Although AIC and BIC are applicable criteria, these are difficult to judge which criteria are better. It depends on the type of problem. Then, AIC and BIC were focused on this work. Furthermore, the estimated parameters were checked the thermodynamic consistency from these two criteria [100].

Criteria 1: The adsorption entropy ( $\Delta S_j^0$ ) must be negative, or the ( $A(K_j)$ ) values should be lower than 1.

$$\Delta S_j^0 < 0$$

$$\exp\left(\frac{\Delta S_j^0}{R}\right) = A(K_j) < 1 \text{ and } > 0$$

$$A(K_j) = K_{j,0} e^{\left(\frac{\Delta H_j}{RT}\right)}$$

Criterion 2: The adsorption entropy of each component shall satisfy the following rule.

$$\Delta S_j^0 \geq 0.0014 \Delta H_j - 12.2 \quad \text{or}$$

$$\ln A(K_j) = -\frac{\Delta S_j^0}{R} \leq \frac{12.2 - 0.0014 \Delta H_j}{R}$$

## CHAPTER IV

### RESULTS AND DISCUSSION

#### 4.1. Catalyst deactivation

The kinetic characterization should be studied at the stable catalyst activity in order to compare the realistic kinetics of the reaction and eliminate the influence of catalyst deactivation. Herein, the feed gas composition for ageing was determined from the equilibrium at 500 °C, considering four species, i.e., H<sub>2</sub>, H<sub>2</sub>O, CO<sub>2</sub>, and CH<sub>4</sub> at atmospheric pressure. In some literature, the catalyst was aged by feeding only H<sub>2</sub> and CO<sub>2</sub> [101]. It is possible, though it takes much time to stabilize catalyst activity. Besides reducing the time consumption, product gases feeding did not cause catalyst deactivation during the kinetic measurements. During catalyst ageing, the catalyst activity was periodically analyzed at the referent temperatures (300, 325, and 350 °C) with feeding ratio of H<sub>2</sub>/CO<sub>2</sub>/Ar at 4/1/5 and atmospheric pressure. Therefore, at the 350 °C provided the highest CO<sub>2</sub> conversion, the stability was more emphasized. According to Figure 7 at 350 °C, the first point was analyzed with non-ageing catalyst and received 10.7% of  $X_{CO_2}$ . After feeding ageing gas composition, the  $X_{CO_2}$  showed expeditiously decreased from 10.7% to 8.5% at 5 h. In other words, catalyst activation was reduced by 20%. Further, it slightly decreased until 25 h, and it seemed pretty stable from 25 to 35 h. Numerically assessed, the reducing of activity at 25 h, 30 h and 35 h showed lower than 0.05%. Even though the total reaction from the aging process is an exothermic reaction, the CO<sub>2</sub> conversions still increase with the temperature because the reaction did not reach equilibrium conversion.

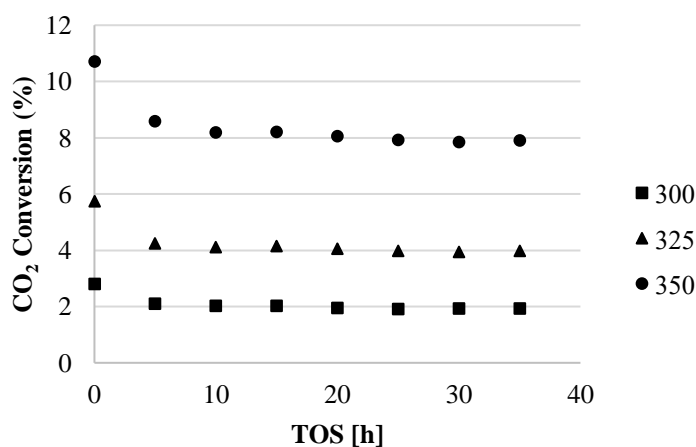


Figure 7. Deactivation of the catalyst during ageing

## 4.2. Isothermal operation

Designing an isothermal reactor in a strongly exothermic reaction is challenging, especially at a high catalyst bed. However, it was successfully operated in this work, as proved by Figure 8. The temperature data were observed and automatically recorded every 10 seconds in an excel file for 40 min. Then, the stable temperature data were averaged and plotted in Figure 8. The temperature furnace at 300 °C showed nearly identical isothermal reactor. For 325 and 350 °C, these presented higher temperature differences between  $T_{top}$  and  $T_{bottom}$  because of higher temperature furnace settings. At 350 °C, the different temperatures higher than 5 °C were observed at 0.9 MPa and gas composition  $H_2/CO_2/Ar = 1/4/2.14$ ,  $1/4/0.55$  and  $1/1/0.66$  because of low concentration of Ar.

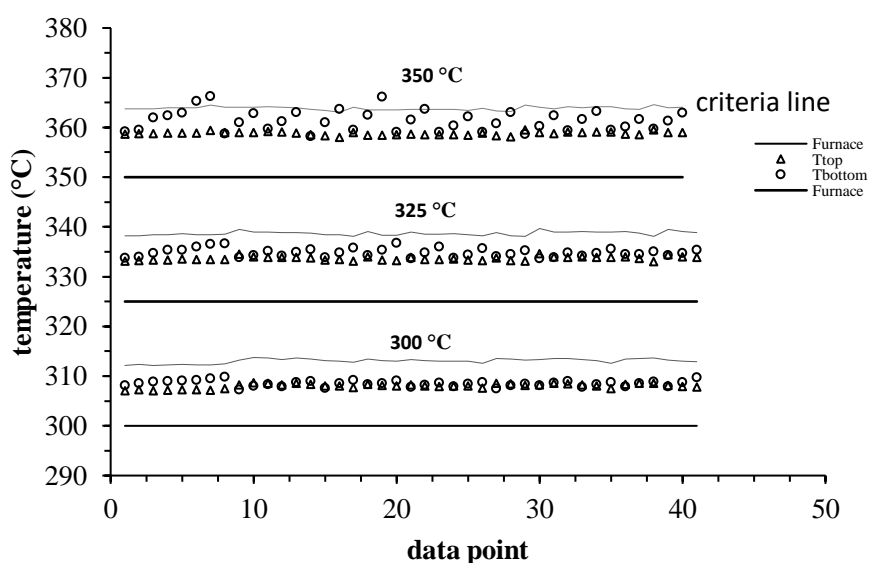


Figure 8. Temperature difference under furnace temperature 300–350 °C

## 4.3. Diffusional limitation

The internal (intra-particle) and external (extra-particle) mass and heat transfer limitations were assessed based on the criterion in Table 7, and the dispersion limitations were evaluated using the equations containing in Table 8. The property of particles, experimental observations and assumption values were expressed in Table 13.

Table 13. Parameters used in the assessment of diffusional limitation

Parameters	Symbols	Values	Units
$r_{CO_2}$ from experiment	$r_{obs}$	8.84E-01	mol m <sup>-3</sup> s <sup>-1</sup>
Particle radius	$R_p$	1.28E-04	m
Particle diameter	$d_p$	2.56 E-04	m
Reaction order (Assumption values)	$n$	1	-
Bed tortuosity (Assumption values)	$\tau_g$	4	-
Bed porosity (Assumption values)	$\varepsilon_p$	0.4	-
Activation energy (Assumption values)	$E_a$	100	kJ mol <sup>-1</sup>
Thermal conductivity of catalyst (Ni/SiO <sub>2</sub> )	$\lambda_s$	0.14	W m <sup>-1</sup> K <sup>-1</sup>
Thermal conductivity of inert ( $\gamma$ Al <sub>2</sub> O <sub>3</sub> )	$\lambda_{inert}$	35	W m <sup>-1</sup> K <sup>-1</sup>
Bulk density of catalyst bed	$\rho_b$	61.99	kg m <sup>-3</sup>
Bulk density of inert material	$\rho_{inert}$	562.13	kg m <sup>-3</sup>
Catalyst bed heigh	$H$	0.0163	m
Catalyst bed diameter	$d_t$	0.005	m
Total pressure	$P$	1.14	atm
CO <sub>2</sub> conversion	$X_{CO_2}$	0.015	-
Amount of catalyst (Ni/SiO <sub>2</sub> ) material	$W_{cat}$	19.84	mg
Amount of Inert ( $\gamma$ Al <sub>2</sub> O <sub>3</sub> ) material	$W_{inert}$	179.91	mg

Table 14. represents a value from the calculation for feeding gas composition of CO<sub>2</sub>/H<sub>2</sub> = 1/4 and 30 mol% of Ar at temperature 300 °C and atmospheric pressure, as an example. The detail for calculations and equations were given in the Appendix A.

Table 14. Calculated values for diffusional limitation

Parameter	Symbol	Value		Units
		Input	Output	
The density of gas mixture	$\rho_g$	0.46	0.46	kg m <sup>-3</sup>
Fluid superficial velocity	$u_o$	0.289	0.289	m s <sup>-1</sup>
the viscosity of the gas mixture	$\mu_g$	3.17E-05	3.17E-05	Pa · s
Diffusivity of CO <sub>2</sub> in gas mixture	$D_{CO_2,mix}$	8.63E-05	8.63E-06	m <sup>2</sup> s <sup>-1</sup>
Effective diffusivity	$D_{CO_2,e}$	8.63E-06	8.59E-05	m <sup>2</sup> s <sup>-1</sup>
The concentration of CO <sub>2</sub> at the solid surface	$C_{CO_2,s}$	3.30	3.26	mol m <sup>-3</sup>
The concentration of CO <sub>2</sub> at the bulk phase	$C_{CO_2,b}$	3.30	3.26	mol m <sup>-3</sup>
Mass transfer coefficient	$k_g$	1.03	1.03	m s <sup>-1</sup>
Heat of reaction	$\Delta H_r$	-178.3	-178.3	kJ mol <sup>-1</sup>
Effective thermal conductivity of particle	$\lambda_e$	0.12	0.12	W m <sup>-1</sup> K <sup>-1</sup>
Effective radial thermal conductivity in the bed catalyst	$\lambda_{er}$	2.87E-01	2.87E-01	W m <sup>-1</sup> K <sup>-1</sup>
Thermal conductivity of gas mixture	$\lambda_g$	9.46E-02	9.41E-02	W m <sup>-1</sup> K <sup>-1</sup>
Heat transfer coefficient	$h$	1340	1333	W m <sup>-2</sup> K <sup>-1</sup>

The mass and heat transfer limitation assessment with input and output gases properties from the example case were listed in Table 15, and other diffusional

limitations were announced in Table 16. Input and output values were calculated from the left of each formula by taking input and output component properties for calculation. The criteria values were determined from the right of equation contained in Tables 15 and 16.

Table 15. Criteria for mass and heat transfer limitations

Transport process	Formula	Calculated value		
		Input	Output	Criterion
Internal mass transfer limitation	$\frac{r_{obs} R_p^2}{D_{CO_2,e} C_{CO_2,s}} < \frac{1}{n}$	5.08E-04	5.18E-04	1
External mass transfer limitation	$\frac{r_{obs} R_p}{k_g C_{CO_2,b}} < \frac{0.15}{n}$	3.31E-05	3.38E-05	0.15
Internal heat transfer limitation	$\frac{ \Delta H_r  r_{obs} R_p^2}{\lambda_e T} < 0.75 \frac{RT}{E_a}$	3.70E-05	3.70E-05	0.036
External heat transfer limitation	$\frac{ \Delta H_r  r_{obs} R_p}{hT} < 0.15 \frac{RT}{E_a}$	2.59E-05	2.60E-05	7.25E-03

Table 16. Criteria for diffusional limitations

Diffusional limitation	Formular	Calculated value	
		Input/output	Criterion
Relative pressure drop over the catalyst bed	$\Delta P < \frac{0.2P}{n}$	1965.33	2878.33
Axial dispersion	$\frac{H}{d_p} > \frac{8}{Bo} n \ln \left\{ \frac{1}{1 - X_{CO_2}} \right\}$	63.67	0.10
Radial dispersion	$\frac{d_t}{d_p} > 8$	19.53	8
Inert bed dilution	$b < \frac{1}{1 + 10X_{CO_2} d_p / H}$	0.50	0.998
Radial heat transfer limitation	$\Delta T_{rad} = \frac{ \Delta H_r  r_{obs} d_t^2 (1 - \epsilon_p)(1 - b)}{32\lambda_{er}} < 0.05 \frac{RT^2}{E_a}$	1.29E-04	3.95E-01

The results from assessment of all conditions were displayed in Figure 9. These are far from the criteria in exponent  $10^4$ . The results from the assessment of the pressure drop, axial dispersion, volumetric dilution ratio, and radial heat transfer limitation were shown in Figure 10, which can be eliminated radial dispersion with  $d_t/d_p$  equal to 19.5. All experimental observations passed the diffusional limitations, and thus all effects mentioned in Tables 7 and 8 can be neglected.

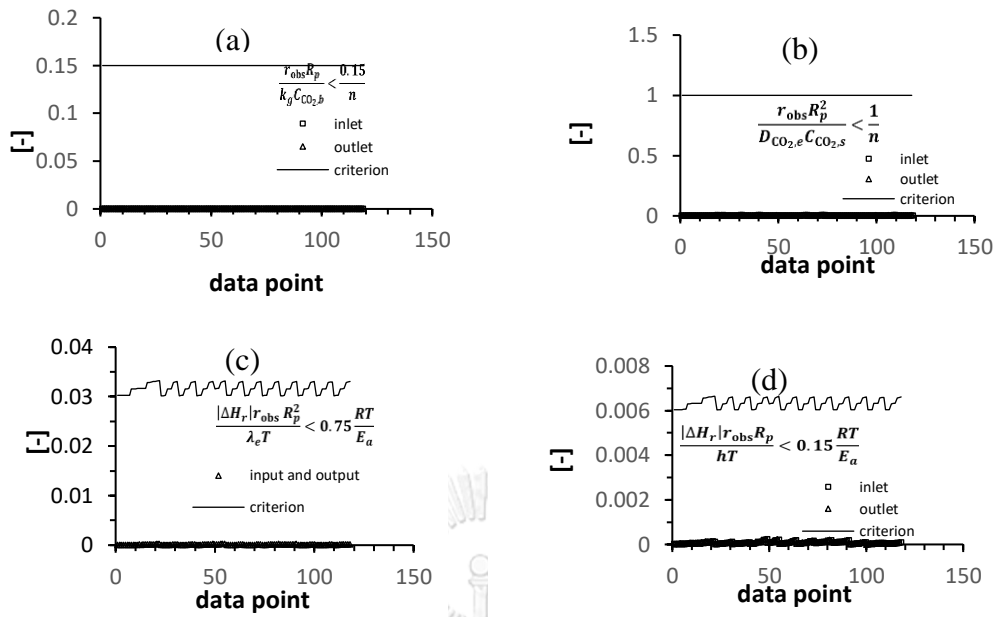


Figure 9. Diffusional limitation results from calculation Table 7: (a) external mass; (b) internal mass; (c) internal heat; (d) internal mass transfer limitations.

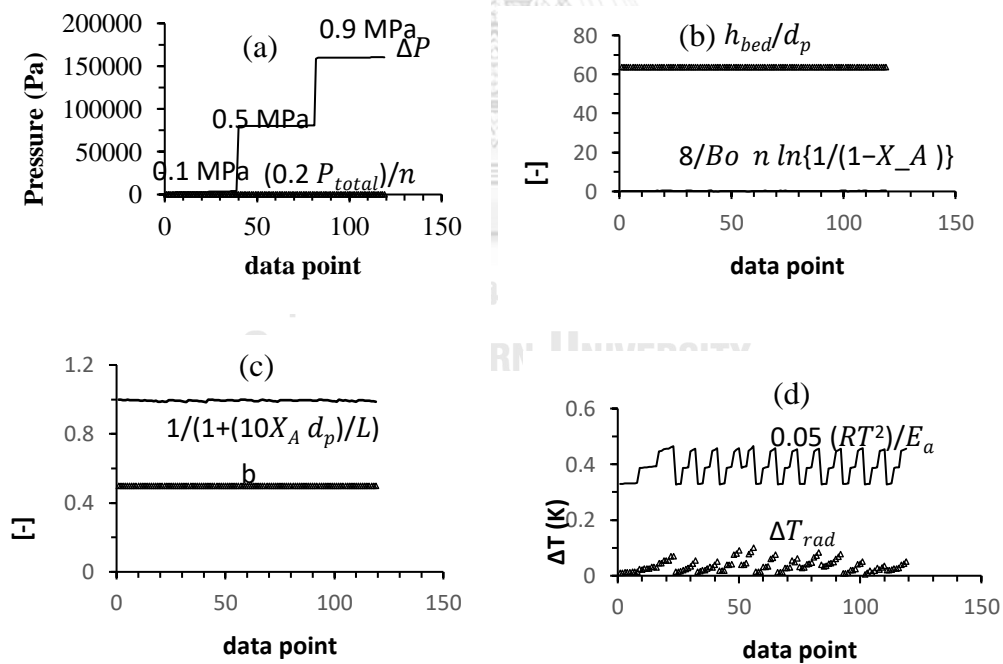


Figure 10. Diffusional limitation results from calculation Table 8: (a) Pressure drop; (b) Axial dispersion; (c) inert bed dilution; (d) Radial heat transfer limitation

#### 4.4. Apparent activation energy and reaction order

The apparent activation energy ( $E_{a,app}$ ) is possible determined using Arrhenius equation by applying reaction rate instead of chemical rate constant ( $k_i$ ). The slope from this graph is  $E_{a,app}/R$ . Herein, the  $E_{a,app}$  for feeding  $H_2/CO_2$  equal to 4/1 with 30% of Ar was reported, as an example. The average temperature between  $T_{top}$  and  $T_{bottom}$  was used for the Arrhenius plot. Figure 11(a) shows the  $E_{a,app}$  of Sabatier reaction at varying total pressure from 0.1 MPa to 0.9 MPa by plotting the natural log of methane reaction rate ( $r_{CH_4}$ ) and  $1/T$  in Kelvin. The averaged  $E_{a,app}$  for all pressures is estimated to be 87 kJ/mol. This value agrees with the literatures, for example, values of 89 kJ/mol are reported for Ni/SiO<sub>2</sub> [70], 70–100 kJ/mol for Ni-based catalyst in CO<sub>2</sub> methanation [102-104]. It was verified of an actual kinetic regime with negligible influence of diffusional limitations [102]. Experimental observations demonstrated a large CO selectivity, then the CO formation cannot be eliminated in this case. The average  $E_{a,app}$  of RWGS reaction at the total pressure 0.1 to 0.9 MPa was 90 kJ/mol, as shown in Figure 11(b), nearly to  $E_{a,app}$  obtained from the Sabatier reaction. This is evidence that the CO formation in CO<sub>2</sub> methanation should be considered to describe the kinetics.

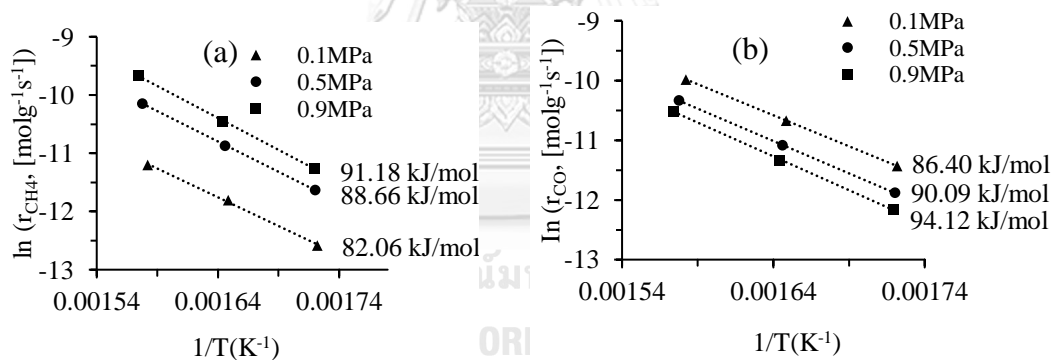


Figure 11. Apparent activation energy with Arrhenius plot ( $H_2/CO_2/Ar = 4/1/2.14$ ): (a) Sabatier reaction; (b) RWGS reaction

The apparent reaction orders were estimated from a simple form of reaction rate,

$r_{1\ or\ 2} = kC_{CO_2}^n$  The slope of log-log plot between reaction rate and CO<sub>2</sub> concentration gave the apparent reaction order with respect to CO<sub>2</sub>. However, it should be noted that the reaction rate obtained from differential mode and absence of transport limitations [105]. In this manuscript, the apparent reaction orders were determined using the experimental observations from non-stoichiometric gas composition feeding ( $H_2/CO_2/Ar = 1/1/2, 1/1/0.67, 2/1/3$  and  $2/1/7$ ) at temperature 300–350 °C and total pressure 0.1–0.9 MPa. Furthermore, these data were unaffected



by the external mass transfer limitation leading to the concentration of  $\text{CO}_2$  at solid phase equal to the concentration of  $\text{CO}_2$  at bulk phase ( $C_{\text{CO}_2,s} = C_{\text{CO}_2,b}$ ). As for Figures 12 and 13, it demonstrated reaction orders at different temperatures and pressures for Sabatier and RWGS reactions, respectively. The average apparent reaction orders with respect to  $\text{CO}_2$  of Sabatier and RWGS reactions are 0.46 and 0.53.

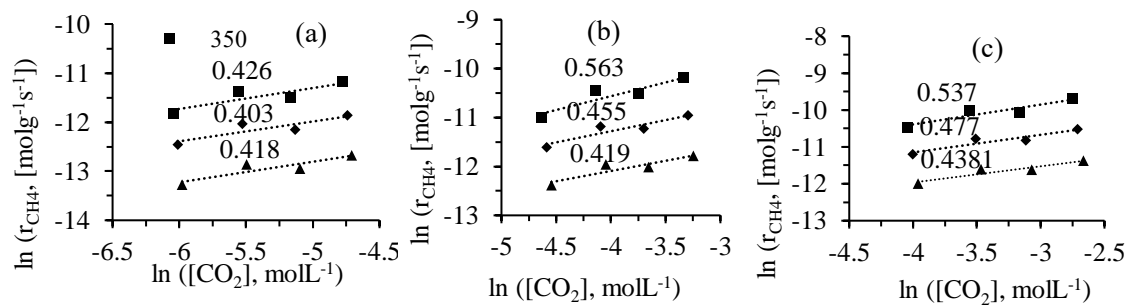


Figure 12. Determining apparent reaction order for Sabatier reaction at different temperatures and total pressures: (a) 0.1MPa; (b) 0.5MPa; and (c) 0.9MPa

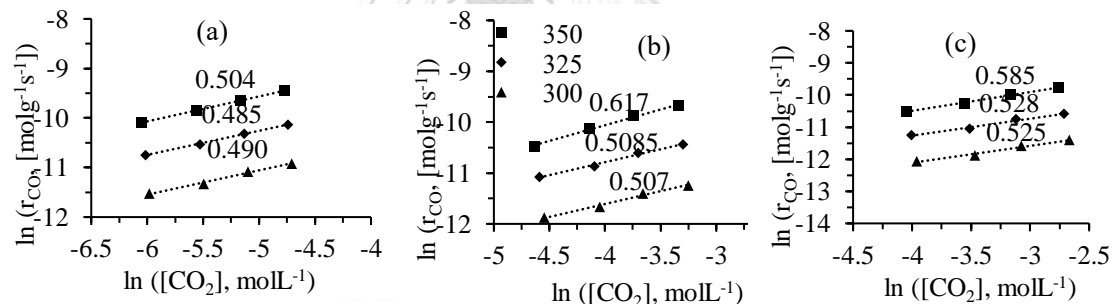


Figure 13. Determining apparent reaction order for RWGS reaction at different temperatures and total pressures: (a) 0.1MPa; (b) 0.5MPa; and (c) 0.9MPa

For the Sabatier reaction, the reaction order of  $\text{H}_2$  was estimated using the Imfit package from Python software. The simple power law equation (Eq.3.1) was adopted for estimation, and the reaction order of  $\text{CO}_2$  was constant at 0.46. The result from fitting is represented in Figure 14, which the reaction order of  $\text{H}_2$  is 0.26. The  $r_{\text{CH}_4,\text{pred}}$  and  $r_{\text{CH}_4,\text{exp}}$  represent methane reaction rate from predictions and experimental observations, respectively.

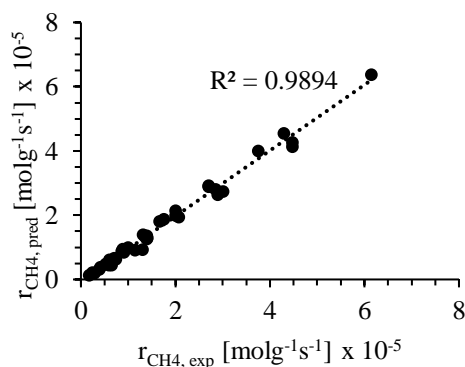


Figure 14. Reaction order of  $H_2$  from estimation: ( $H_2/CO_2/Ar = 1/1/2, 1/1/0.67, 2/1/3, 2/1/7, 5/1/2, T=300-350\text{ }^\circ\text{C}, 0.1-0.9\text{ MPa.}$ )

Moreover, the estimated parameters can provide a similar reaction rate for the data acquired at the stoichiometric conditions ( $H_2/CO_2/Ar = 4/1/5, 4/1/2.1, 4/1/0.5, T=300-350\text{ }^\circ\text{C}, 0.1-0.9\text{ MPa.}$ ), as shown in Figure 15, where  $r_{CH_4,cal}$  stands for the reaction rate of methane from the calculation.

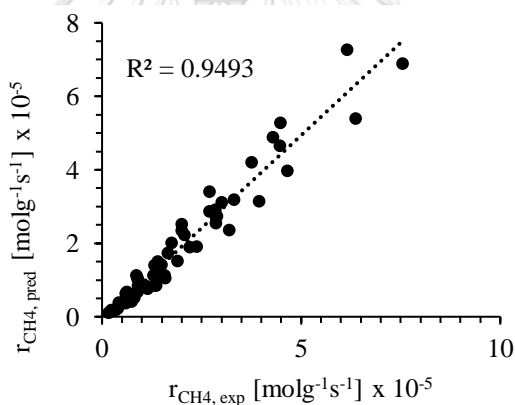


Figure 15. Calculated  $r_{CH_4}$  using estimated parameters from Figure 14.

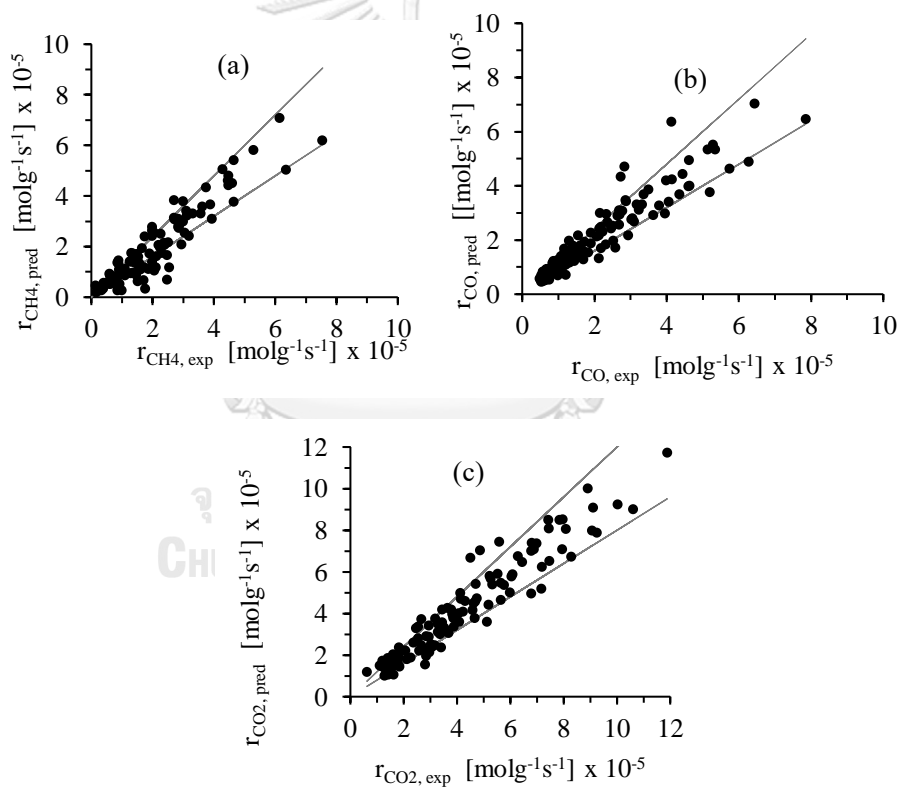
#### 4.5. Kinetic model and parameter estimation

Kinetic parameters were estimated using experimental data obtained from conditions listed in Table 6. Note that using experimental data must be showed non-diffusional transport,  $\Delta T$  lower than  $5\text{ }^\circ\text{C}$ , and  $CO_2$  conversion lower than 10%. The experimental data were first fitted with power law models by considering only the Sabatier reaction. The reaction orders of  $H_2$  and  $CO_2$  were regarded as constant at 0.26 and 0.46, respectively. The results from fitting the power law models are listed in Table 17. The model discrimination was assessed by the lowest chi-square, AIC, and BIC values. Herein, the power law model from inhibiting influence of water (PL- $H_2O$ ) demonstrated the best fitting.

Table 17. The values for model discrimination

	PL	PL-H <sub>2</sub> O	PL-WI	PL-HI
chi-square	3.84x 10 <sup>-9</sup>	3.31 x 10 <sup>-9</sup>	3.84 x 10 <sup>-9</sup>	3.84 x 10 <sup>-9</sup>
AIC	-2745	-2760	-2741	-2741
BIC	-2739	-2751	-2730	-2730

Later, the RWGS reaction was considered using Eq.3.2, 3.4, 3.6, and 3.8. Eq.3.4 (power law without the influence of water) gave the lowest values of AIC and BIC. The parity plots of  $r_{CH_4}$ ,  $r_{CO}$  and  $r_{CO_2}$  ( $r_{CO_2} = r_{CH_4} + r_{CO}$ ) from prediction and experiment were shown in Figure 16, and the estimated parameters were listed in Table 18. Note that the CO methanation reaction was later added to improve the parity plot, however the negative activation energy was observed. Then the CO methanation was not considered in this work.

Figure 16. Results from fitting PL-H<sub>2</sub>O model: (a)  $r_{CH_4}$ ; (b)  $r_{CO}$ ; (c)  $r_{CO_2}$ 

Based on Figure 16(c), Almost all data points were located within an error equal to 20% region, however all data points are within an error of 35% region.

Table 18. Estimated parameter from PL-H<sub>2</sub>O (PL-H<sub>2</sub>O<sub>Sabatier</sub> and PL-H<sub>2</sub>O<sub>RWGS</sub>)

Parameter	Value	Unit
Sabatier reaction		
$k_{1,0,ref}$	$5.29 \times 10^{-6} \pm 5.8 \times 10^{-7}$	$\text{mol g}^{-1} \text{s}^{-1} \text{bar}^{-0.86}$
$E_{a,1}$	$67.14 \pm 4.36$	$\text{kJ mol}^{-1}$
$n_{H_2,1}$	$0.26 \pm 0.02$	-
$n_{CO_2,1}$	$0.46$	-
$n_{H_2O,1}$	$-0.06 \pm 0.014$	-
RWGS reaction		
$k_{2,0,ref}$	$7.52 \times 10^{-6} \pm 7.02 \times 10^{-7}$	$\text{mol g}^{-1} \text{s}^{-1} \text{bar}^{0.49}$
$E_{a,2}$	$89.47 \pm 3.57$	$\text{kJ mol}^{-1}$
$n_{H_2,2}$	$-0.55 \pm 0.026$	-
$n_{CO_2,2}$	$0.18 \pm 0.054$	-
$n_{H_2O,2}$	$-0.12 \pm 0.010$	-

According to Table 18, the apparent reaction orders with respect to CO<sub>2</sub> and H<sub>2</sub> for the Sabatier reaction were 0.46 and 0.26 ± 0.02, respectively, which indicated that the CO<sub>2</sub> concentration had more significant effects on the  $r_{CH_4}$  than H<sub>2</sub> concentration. Furthermore, it can be described by competitive adsorption between H<sub>2</sub> and CO<sub>2</sub>. CO<sub>2</sub> dissociation species adsorb and cover the active surface area more affluent than H atoms [106]. This work observed a reaction order of CO<sub>2</sub> higher than H<sub>2</sub>. Consistent with Chiang and Hopper [69], who reported the reaction orders with respect to CO<sub>2</sub> and H<sub>2</sub> were 0.66 and 0.21, respectively. Similarly, Vidal et al. [107] studied kinetic models of CO<sub>2</sub> methanation over 15 wt%Ni/Mg/Al hydrotalcite coated catalyst. The reaction orders of CO<sub>2</sub> and H<sub>2</sub> of 0.31 and 0.129 were found, respectively. In contrast with other literatures, Garbarino et al. [108] realized that the reaction orders with respect to H<sub>2</sub> and CO<sub>2</sub> over Ni/Al<sub>2</sub>O<sub>3</sub> catalyst were 0.32 and 0.17, respectively. The low reaction orders were observed because of the strong adsorption of CO<sub>2</sub> and hydrogen on the surface of the catalyst. Another work from Garbarino et al. [49] found that the H<sub>2</sub> concentration was more affected than CO<sub>2</sub> concentration in CO<sub>2</sub> methanation using Ni/La-Al<sub>2</sub>O<sub>3</sub>.

As for the observation of negative orders, a negative order indicates that the concentration of that species inversely affects the reaction rate. For negative order of H<sub>2</sub>O, adding steam in CO<sub>2</sub> methanation reaction is normally inhibiting the forward of reaction because atomic water will be mainly adsorbed on active site resulting in lower vacancy site free for CO<sub>2</sub> and H<sub>2</sub> [109]. However, the result from this work observed negative orders of H<sub>2</sub>O because H<sub>2</sub>O did not affect inhibiting the forward of reaction. As for the negative reaction order of H<sub>2</sub> in RWGS reaction, it was suggested that the CH<sub>4</sub> formation competitively inhibited the CO formation. Also, Kikkawa [110] found the same result for achieving the negative reaction order of H<sub>2</sub> in CO<sub>2</sub>

methanation over Ni catalyst with consideration of RWGS reaction. The negative reaction order is also observed in other reactions. For instance, Richardson et al. [111] acknowledged the negative order with respect to CO<sub>2</sub> in CO<sub>2</sub> reforming of methane reaction using Pt–Re catalysts supported on ceramic foam. They suggested that CO<sub>2</sub> strongly adsorbed on the Pt–Re sites. Paksoy et al. [112] studied CO<sub>2</sub> reforming of methane over Co–Ce/ZrO<sub>2</sub> catalysts and observed the small negative order for CO<sub>2</sub>. It can be explained that the CO<sub>2</sub> inhibited the H<sub>2</sub> (and/or CO) production. In this work, the power law rate models of CO<sub>2</sub> methanation considering Sabatier and RWGS reactions can be represented as Eqs.4.1 and 4.2, respectively.

$$r_1 = k_1 p_{H_2}^{0.27} p_{CO_2}^{0.44} p_{H_2O}^{0.06} \left( 1 - \frac{p_{CH_4} p_{H_2O}^2}{p_{H_2}^4 p_{CO_2} K_{eq,1}} \right) \quad Eq\ 4.1$$

$$r_2 = k_2 \frac{p_{H_2O}^{0.13} p_{CO_2}^{0.18}}{p_{H_2}^{0.56}} \left( 1 - \frac{p_{CO} p_{H_2O}}{p_{H_2} p_{CO_2} K_{eq,2}} \right) \quad Eq\ 4.2$$

Since a power rate law is inadequate to describe the kinetics of the reaction, the Langmuir-Hinshelwood equations derived from Lalinde and group [65] were also emphasized to predict the mechanism of CO<sub>2</sub> methanation over Ni/SiO<sub>2</sub> catalyst. Three mechanism assumptions were investigated in this work. First, mechanism A (Table 9) represented the assumption mechanism of dissociation of CO<sub>2</sub> to CO\* and subsequent dissociation to C\*. Further, the C\* was hydrogenated to produce CH<sub>4</sub>. This mechanism can be called CO<sub>2</sub> methanation via CO or C intermediate formation. Table 10 showed CO<sub>2</sub> methanation through formate species (HCOO\*) formation. The CO<sub>2</sub> adsorbs on the support surface and reacts with adsorbed hydrogen atoms, forming formate species at the metal-support interface. Subsequently, hydrogenation of HCOO\* to COH\* (formyl species) and CH<sub>4</sub>. The hybrid mechanism between A and B was considered, as shown in Table 11.

According to the fitting of power law models, the inhibiting influence of water assumption showed the best result, then the general form of LH approach (Eq.3.9) was developed and expressed in Eq. 4.3 by eliminating  $K_{OH} \cdot p_{H_2O} \cdot p_{H_2}^{-0.5}$  term. The estimations with and without  $K_{OH} \cdot p_{H_2O} \cdot p_{H_2}^{-0.5}$  term showed similar parameter values with a similar chi-squared (not shown here), then it is insignificant to add  $K_{OH} \cdot p_{H_2O} \cdot p_{H_2}^{-0.5}$  term.

$$r_1 = \frac{k_1 \cdot K_{Ae} p_{CO_2}^a K_{H_2}^b p_{H_2}^c p_{H_2O}^d \left(1 - \frac{p_{CH_4} p_{H_2O}^2}{p_{CO_2} p_{H_2}^4 K_{eq,1}}\right)}{\left(1 + K_{Ae} p_{CO_2}^e K_{H_2}^f p_{H_2}^g p_{H_2O}^h + K_{H_2}^{0.5} p_{H_2}^{0.5}\right)^i} \quad Eq. 4.3$$

The results from fitting 20 models are expressed in Table 19, NO8 showed the lowest chi-square, AIC, and BIC values.

Table 19. Values for model discrimination of LH approach

	chi-square	AIC	BIC
NO18	2.41E-08	-2529.49	-2515.8
NO17	1.59E-08	-2576.98	-2563.3
NO2	1.34E-08	-2594.69	-2578.27
NO4	5.09E-09	-2706.76	-2693.08
NO3	4.77E-09	-2712.19	-2695.77
NO15	4.85E-09	-2712.39	-2698.71
NO16	4.30E-09	-2726.07	-2712.39
NO12	4.08E-09	-2732.22	-2718.54
NO14	3.57E-09	-2747.26	-2733.58
NO10	3.54E-09	-2748.17	-2734.49
NO11	3.54E-09	-2748.34	-2734.65
NO9	3.53E-09	-2748.51	-2734.83
NO7	3.48E-09	-2750.36	-2736.68
NO13	3.44E-09	-2751.52	-2737.84
NO6	3.43E-09	-2751.92	-2738.24
NO5	3.31E-09	-2753.89	-2737.48
NO8	3.35E-09	-2754.48	-2740.8

After that, the CO formation was considered using power law models derived from the RWGS reaction. The results from fitting  $r_{CO}$ ,  $r_{CH_4}$  and  $r_{CO_2}$  are shown in Figure 17, and the estimated kinetic parameters are listed in Table 20.

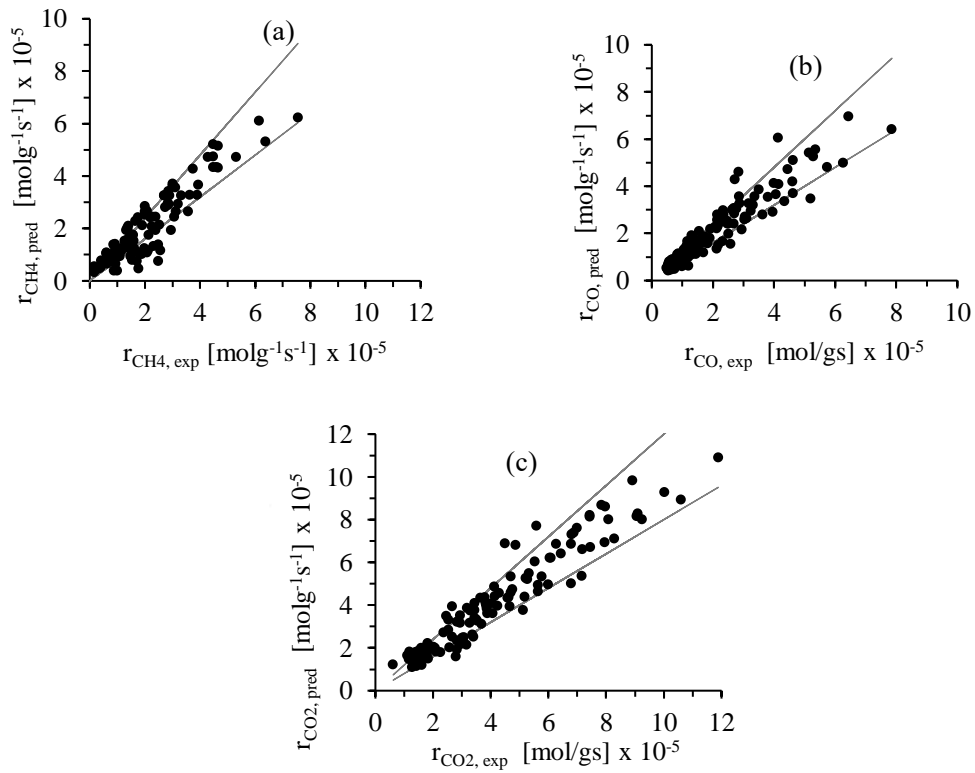


Figure 17. Results from fitting LH: (a)  $r_{CH_4}$ ; (b)  $r_{CO}$ ; (c)  $r_{CO_2}$

Table 20. Estimated parameter from hybrid models ( $NO_{8Sabatier}$  and  $PL-H_2O_{RWGS}$ )

Parameter	Value	Unit
Sabatier reaction		
$k_{1,0,ref}$	$4.90 \times 10^{-5} \pm 5.33 \times 10^{-6}$	$\text{mol g}^{-1} \text{s}^{-1} \text{bar}^{-0.5}$
$E_{a,1}$	$115.36 \pm 4.38$	$\text{kJ mol}^{-1}$
$K_{H_2,0,ref}$	$0.40 \pm 0.029$	bar
$\Delta H_{H_2}$	$-88.79 \pm 2.83$	$\text{kJ mol}^{-1}$
$K_{CO,0,ref}$	$0.81 \pm 0.029$	$\text{bar}^{-1}$
$\Delta H_{CO}$	$-34.63 \pm 1.45$	$\text{kJ mol}^{-1}$
RWGS reaction		
$k_{2,0,ref}$	$8.01 \times 10^{-6} \pm 7.49 \times 10^{-7}$	$\text{mol g}^{-1} \text{s}^{-1} \text{bar}^{0.25}$
$E_{a,2}$	$89.40 \pm 3.62$	$\text{kJ mol}^{-1}$
$n_{H_2,2}$	$-0.61 \pm 0.026$	-
$n_{CO_2,2}$	$0.23 \pm 0.025$	-
$n_{H_2O,2}$	$-0.14 \pm 0.010$	-

The activation energies of the forward Sabatier reaction obtained in this work are 67 and 115 kJ/mol for the power law and LH models, respectively. These values showed in the range obtained from other literatures, which reported about 60–120 kJ/mol for Ni-catalysts [56, 64, 65, 69-73, 75, 113, 114]. In addition, the activation energy obtained higher than 50 kJ/mol indicates that the experimental kinetic investigations were studied with the absence of transport limitations [115]. The value of activation energy for RWGS reaction was 89 kJ/mol, nearly with Marocco et al. [94], who reported 85 kJ/mol for RWGS reaction over Ni catalyst. Moreover, the enthalpy change of adsorption of H<sub>2</sub> ( $\Delta H_{H_2}$ ) is nearly obtained value from Rönsch et al. [116] at -88 kJ/mol, and also a similar result for H<sub>2</sub> adsorption on Ni catalyst is an exothermic reaction [64, 72]. The pre-exponential factors ( $k_{i,0,ref}$ ) are based on the reference temperature ( $T_{ref} = 281.85$  °C). The estimated parameters from RWGS reaction were described in the previous section. The kinetic models for the combination between LH and the power law model were demonstrated in Eq.4.4–4.5.

$$r_1 = \frac{k_1 K_{CO} p_{CO_2}^{0.5} K_{H_2}^{0.5} p_{H_2}^{0.5} \left(1 - \frac{p_{CH_4} p_{H_2O}^2}{p_{CO_2} p_{H_2}^4 K_{eq,1}}\right)}{\left(1 + K_{CO} p_{CO_2}^{0.5} + K_{H_2}^{0.5} p_{H_2}^{0.5}\right)^2} \quad Eq\ 4.4$$

$$r_2 = \frac{k_2 p_{H_2O}^{0.14} p_{CO_2}^{0.23}}{p_{H_2}^{0.61}} \left(1 - \frac{p_{CO} p_{H_2O}}{p_{H_2} p_{CO_2} K_{eq,2}}\right) \quad Eq\ 4.5$$

The results from the thermodynamic consistency of the adsorption term were shown as follows. The equations were early mentioned in section 3.5, which  $\Delta S_j^0$  represents in-unit J/molK, and the referent temperature at 280 °C was used for calculation.

Criterion 1:

$$A(K_{H_2}) = 1.76 \times 10^{-9} < 1 \text{ and } > 0$$

$$A(K_{CO}) = 4.4 \times 10^{-4} < 1 \text{ and } > 0$$

Criterion 2:

$$\ln A(K_{H_2}) = -20 \leq \frac{12.2 - 0.0014 \Delta H_j}{R} = 16$$

$$\ln A(K_{CO}) = -7.7 \leq \frac{12.2 - 0.0014 \Delta H_j}{R} = 7.29$$

The  $A(K_{H_2})$  and  $A(K_{CO})$  were proved as thermodynamic consistency, in other words these values satisfies the fundamental Gibbs–Duhem equation.

Values for model discrimination of power rate law models (Eq.4.1 and 4.2) and hybrid models (Eq.4.4 and 4.5) were shown in Table 21. Hybrid models showed low chi-square, AIC, and BIC. Then, it can be concluded that the hybrid models between LH and power law models with formyl formation as RDS and non-influence



of water are suitable to describe the kinetics of CO<sub>2</sub> methanation over Ni/SiO<sub>2</sub> catalyst.

Table 21. Values for model discrimination of LH approach

	Power law	Hybrid
chi-square	1.25x10 <sup>-9</sup>	1.23 x10 <sup>-9</sup>
AIC	-8210	-8212
BIC	-8190	-8192

Note that the determination of kinetic parameters is a prerequisite. The obtained kinetic models and parameters can be applied to predict reactors' performance for reactor design. The CO<sub>2</sub> conversion was calculated from the ordinary differential equation based on mole balance over a packed bed reactor shown as:

$$\frac{dn_i}{dm} = \vartheta_i \cdot r_1 + \alpha_i \cdot r_2$$

Where  $n_i$  is the molar flow of component  $i$ .  $\vartheta_i$  and  $\alpha_i$  represent the stoichiometric coefficient of Sabatier and RWGS reactions, respectively, and  $m$  stands for catalyst weight. The performance of Ni/SiO<sub>2</sub> catalyst in a plug flow reactor at different flow rates is shown in Figure 18. The highest CO<sub>2</sub> conversion was demonstrated at a temperature of 400 °C and 20 ml/min, and it was decreased because of the thermodynamic limitations. However, the increasing total flow rate expressed lower CO<sub>2</sub> conversion at the same temperature. Moreover, the condition can be freely changed to design the reactor.

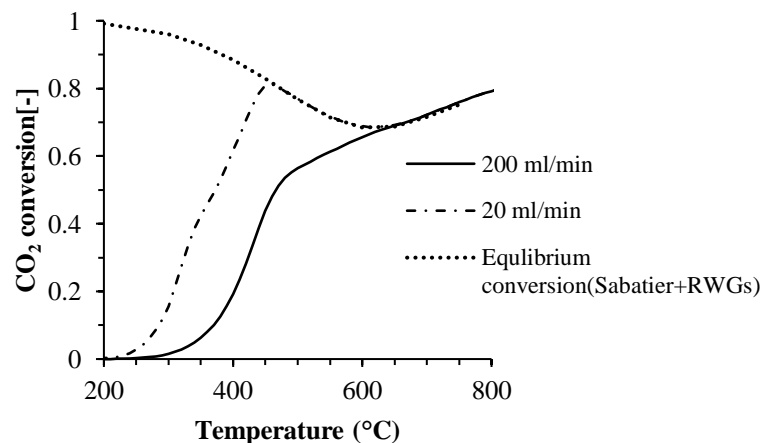


Figure 18. Prediction performance of reactor for Ni/SiO<sub>2</sub> catalyst under H<sub>2</sub>/CO<sub>2</sub>/Ar = 4/1/5, P = 0.5 MPa, Q = 200 and 20 ml/min, m = 20 mg.

Also, the collected kinetic models and parameters from literatures can be compared to investigate the performance of catalyst and reactor. As expected,

NiAl(O)<sub>x</sub> [64] demonstrated the highest catalyst activity. The catalyst activity from this work agreed with Chaing and Hopper [69], who provided the power law model obtained from kinetic study over Ni/kieselguhr catalyst. It showed a similar trend line in the range of temperature 200–470 °C, and the reaction rate seems slow because it is limited by equilibrium conversion.

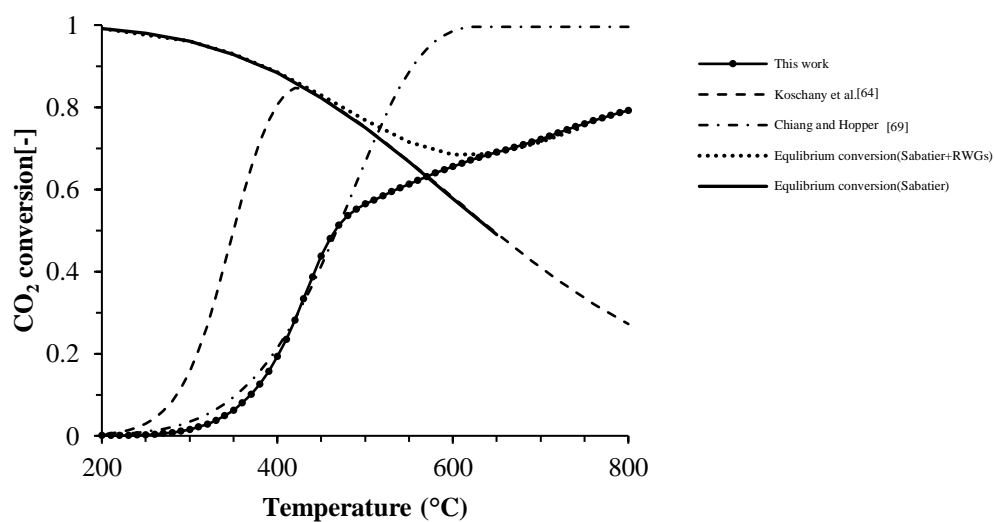


Figure 19. Temperature versus CO<sub>2</sub> conversion compared to other literature for H<sub>2</sub>/CO<sub>2</sub>/Ar = 4/1/5 P = 0.5 MPa, Q = 200 ml/min, m = 20 mg.



## CHAPTER V

### CONCLUSION

#### 5.1. Conclusion

The kinetic models were studied considering Sabatier and RWGS reactions in CO<sub>2</sub> methanation. The kinetic characterizations were studied in an isothermal packed bed reactor with the differential condition at temperature 300–350 °C, 0.1 to 0.9 MPa, GHSV of 37,494 h<sup>-1</sup> over commercial 17–23%wt Ni/SiO<sub>2</sub> catalyst at the stable catalyst activity. The experimental data for parameter estimations were absent from diffusional limitation, CO<sub>2</sub> conversion and  $\Delta T$  lower than 10% and 5 °C. Modeled considerations, the power law (PL, PL-H<sub>2</sub>O, PL-WI and PL-OH) and LH models were first emphasized only considering Sabatier reaction. Then, the RWGS reaction was added to account for the CO formation using the power law models. The model discriminations were assessed using AIC and BIC. The results found that 1) These experimental conditions successfully built an isothermal reactor without diffusional limitation. 2) The better fitting was obtained from hybrid model (LH and the power law model) with the formation of formyl as RDS and inhibiting influence of water. 3) The activation energies of the Sabatier and RWGS reactions were found in the range of other literature.

#### 5.2. Recommendation

1. The integral mode reactor should be taken into account to study the complete range of CO<sub>2</sub> conversion.
2. The characteristics of the catalyst should be checked to compare the results before and after the reaction to clearly explain the results.

## APPENDIX

## APPENDIX A

## THE EQUATION FOR ASSESMENT DIFFUSIONAL LIMITATION

A.1. Diffusivity of CO<sub>2</sub>

The effective mass diffusivity of CO<sub>2</sub> in the catalyst particle ( $D_{CO_2,e}, m^2s^{-1}$ ) was determined from Eq.A1, where porosity ( $\varepsilon_p$ ) and tortuosity ( $\tau_p$ ) of the catalyst particle were assumed equal to 0.4 and 4 following Miguel's work [71].

$$D_{CO_2,e} = \frac{D_{CO_2,mix} \varepsilon_p}{\tau_p} \quad Eq. A 1$$

Molecular diffusivity of CO<sub>2</sub> in the gas mixture ( $D_{CO_2,mix}, m^2s^{-1}$ ) expressed in Eq.A2, where  $y$  stands for mole fraction.

$$D_{CO_2,mix} = \frac{1 - y_{CO_2}}{\sum_{j=1}^n \frac{y_j}{D_{CO_2,j}}} \times 10^{-4} \quad Eq. A 2$$

To determine the diffusivity of CO<sub>2</sub> into a component  $j$  or  $D_{CO_2,j}$  in-unit  $cm^2s^{-1}$ , it can be estimated through the following equation, which  $M$  is molecular weight in-unit ( $g \text{ mol}^{-1}$ ),  $P$  stands for pressure in atm unit,

$$D_{CO_2,j} = \frac{10^{-3} T^{1.75} \left( \frac{1}{M_{CO_2}} + \frac{1}{M_j} \right)^{0.5}}{P \left[ (\sum \nu)_{CO_2}^{1/3} + (\sum \nu)_j^{1/3} \right]^2} \quad Eq. A 3$$

Where  $j$  is pure gas (H<sub>2</sub>, CH<sub>4</sub>, H<sub>2</sub>O, CO, Ar), and the diffusion volumes ( $\nu$ ) to calculate Eq.A3 was shown in Table A1 [117].

Table A 1. Diffusion volumes for simple molecules ( $\sum v, \text{cm}^3 \cdot \text{mol}^{-1}$ ) of each component

Molecule	Diffusion volume, ( $\sum v$ )
CO <sub>2</sub>	26.7
H <sub>2</sub>	6.12
H <sub>2</sub> O	13.1
CH <sub>4</sub>	25.14
CO	18
Ar	16.2

### A.2. Concentration of CO<sub>2</sub> at the solid surface

The concentration of CO<sub>2</sub> at the solid surface ( $C_{\text{CO}_2,s}, \text{molm}^{-3}$ ) and the bulk phase ( $C_{\text{CO}_2,b}, \text{molm}^{-3}$ ) can be estimated through the equation below [96].

$$C_{\text{CO}_2,s} = (1 - C_a)C_{\text{CO}_2,b} \quad \text{Eq. A 4}$$

$$C_{\text{CO}_2,b} = \frac{y_{\text{CO}_2}}{RT} \quad \text{Eq. A 5}$$

Where the Carberry number is the dimensionless term expressed in Eq.A6

$$C_a = \frac{r_{\text{obs}}}{k_g \frac{6}{d_p} C_{\text{CO}_2,b}} \quad \text{Eq. A 6}$$

The external mass transfer coefficient ( $k_g, \text{m s}^{-1}$ ) was given in section heat and mass transport coefficient.

### A.3. Heat of reaction and heat capacity

The heat of reaction ( $\Delta H_r, \text{Jmol}^{-1}$ ) can be calculated through Eq.A7.

$$\Delta H_r(T) = \Delta H_r^{298\text{K}} + R \int_{298\text{K}}^T \frac{\Delta C_p^0}{R} dT \quad \text{Eq. A 7}$$

Where the standard heat of Sabatier reaction at 298 K is equal to  $-165 \text{ Jmol}^{-1}$ , and the integral term was estimated from the Shomate equation [118].

$$R \int_{298\text{K}}^T \frac{\Delta C_p^0}{R} dT = \Delta A(T - T_0) + \frac{\Delta B}{2}(T^2 - T_0^2) + \frac{\Delta C}{3}(T^3 - T_0^3) + \frac{\Delta D}{4}(T^4 - T_0^4) - \Delta E \left( \frac{1}{T} - \frac{1}{T_0} \right) \quad \text{Eq. A 8}$$

The heat capacity of gas mixture ( $C_{p,mix}, Jkg^{-1}K^{-1}$ ) was estimated through Eq.A9, and the isobaric specific heat capacity of each species ( $C_{p,i}, Jmol^{-1}K^{-1}$ ) was determined by using the Shomate equation that provided the accuracy value expressed in Eq.A10.

$$C_{p,mix} = \sum_{i=1}^n \frac{y_i C_{p,i}}{M_i} \quad Eq. A 9$$

$$C_{p,i} = A + BT' + CT'^2 + CT'^3 + CT'^2 \quad Eq. A 10$$

Where  $T' = T(K)/1000$ ,  $T_0 = 298.15/1000$  and polynomial constant for Shomate equation was expressed in Table A2.  $\Delta A$  to  $\Delta E$  can be calculated following the mole from the Sabatier reaction, for example,  $\Delta A = (A_{CH_4} + 2A_{H_2O}) - (A_{CO_2} + 4A_{H_2})$ .

Table A 2. The polynomial constant for Shomate equation [118].

Constant	A	B	C	D	E	F	G
CO	25.57	6.10	4.05	-2.67	0.13	-118.0	227.3
CH <sub>4</sub>	-0.70	108.48	-42.52	5.86	0.68	-76.8	158.7
CO <sub>2</sub>	25.00	55.19	-33.69	7.95	-0.14	-403.6	228.2
H <sub>2</sub> O	30.09	6.83	6.79	-2.53	0.08	-250.8	223.3
H <sub>2</sub>	33.07	-11.36	11.43	-2.77	-0.16	-9.9	172.7
Ar	20.78	2.83x10 <sup>-07</sup>	-1.46X10 <sup>-07</sup>	1.09 X10 <sup>-08</sup>	-3.66X10 <sup>-08</sup>	-6.19	179.9

#### A.4. Thermal conductivity

The effective thermal conductivity of the particle,  $\lambda_e$  ( $W \cdot m^{-1} \cdot K^{-1}$ ), was calculated from equation below.

$$\lambda_e = \lambda_g \left( \frac{\lambda_s}{\lambda_g} \right)^{1-\varepsilon_p} \quad Eq. A 11$$

Where the thermal conductivity of Ni/SiO<sub>2</sub> catalyst ( $\lambda_s$ ) was followed by Sharma that reported  $\lambda_s = 0.14$  with  $\varepsilon_p = 0.4$  [119]

The thermal conductivity of the gas mixture ( $\lambda_g, Wm^{-1}K^{-1}$ ) was determined by the Wassiljewa method, as shown in Eq.A12.

$$\lambda_g = \sum_{i=1}^n \frac{y_i \lambda_{g,i}}{\sum_{j=1}^n y_j A_{ij}} \quad Eq. A 12$$

Where the thermal conductivity of each species ( $\lambda_{g,i}$ ) was determined by the Eucken model [120].

$$\lambda_{g,i} = \mu_i \left( \frac{5 R}{4 M_i} - \frac{C_{p,i}}{M_i} \right) \quad \text{Eq. A 13}$$

The  $A_{ij}$  stands for binary interaction parameter estimated by the equation below.

$$A_{ij} = \frac{\left[ 1 + (\lambda_{tr,i} / \lambda_{tr,j})^{0.5} (M_i / M_j)^{0.25} \right]^2}{\left[ 8(1 + M_i / M_j) \right]^{0.5}} \quad \text{Eq. A 14}$$

Where  $\left( \frac{\lambda_{tr,i}}{\lambda_{tr,j}} \right)$  is a term of translational thermal conductivities ratio calculated by Eq.A15

$$\frac{\lambda_{tr,i}}{\lambda_{tr,j}} = \frac{\Gamma_j [\exp(0.0464T_{r,i}) - \exp(-0.2412T_{r,i})]}{\Gamma_i [\exp(0.0464T_{r,j}) - \exp(-0.2412T_{r,j})]} \quad \text{Eq. A 15}$$

*S I*

$T_{r,i}$  equal to  $T/T_{c,i}$  and  $\Gamma_j$  or  $\Gamma_i$  are the reduced or inversed thermal conductivity of each species determined through Eq.A16.

$$\Gamma_i = 210 \left( \frac{T_{c,i} M_i^3}{P_{c,i}^4} \right)^{1/6} \quad \text{Eq. A 16}$$

Where  $T_{c,i}$  (K),  $P_{c,i}$  (bar) and  $M_i$  ( $\text{kg}\cdot\text{mol}^{-1}$ ) are the critical temperature, critical pressure and molar weight of species, as shown in the following table.

Table A 3. Critical property and molecular weight of gases

Property	CO	CH4	CO2	H2O	H2	Ar
Critical temperature, $T_c$ (K)	734.45	190.6	304.18	647	33.18	150.86
Critical pressure, $P_c$ (bar)	34.98	46.1	73.80	220.64	13	4.89
Molar weight, $M$ ( $\text{kg}\cdot\text{mol}^{-1}$ )	0.02801	0.01604	0.04401	0.01802	0.002016	0.03995

### A.5. Heat transport coefficient

Heat transport coefficient  $h(Wm^{-2}K^{-1})$ , was calculated from a correlation expressed in Eq.S17 [96].

$$h = \frac{Nu\lambda_g}{d_p} \quad \text{Eq. A 17}$$

$Nu$  is a Nusselt number, it can be determined from the dimensionless term section. The  $\lambda_g$  expresses in thermal conductivity section. To calculate the external mass transfer coefficient ( $k_g, m s^{-1}$ ), the Eq.A18 was used [96].

$$k_g = \frac{ShD_{CO_2,mix}}{d_p} \quad \text{Eq. A 18}$$

Where  $Sh$  stands for Sherwood number that can be calculated in equation expressed in dimensionless term section, and  $D_{CO_2,mix} (m^2s^{-1})$  can be calculated from Eq.A2.

### A.6. Dimensionless term

The Sherwood number ( $Sh$ ) can be estimated through Eq.A19 [121].

$$Sh = 2 + 1.1Re_p^{0.6} Sc^{1/3} ; 0.1 < Re < 100 \quad \text{Eq. A 19}$$

Where  $Re_p$  and  $Sc$  stand for Reynolds and Schmidt numbers, respectively. These were calculated from the following equation when  $d_p$  (m) is the diameter of particle.

$$Sc = \frac{\mu_g}{\rho_g D_{CO_2,mix}} \quad \text{Eq. A 20}$$

$$Re_p = \frac{\rho_g u_o d_p}{\mu_g} \quad \text{Eq. A 21}$$

To calculate Nusselt number( $Nu$ ), the equation was provided by Berger [96]. Note that it is applicable for  $0.1 < Re_p < 100$

$$Nu = 2 + 1.1Re_p^{0.6} Pr^{1/3} \quad \text{Eq. A 22}$$

Where Prandtl number ( $Pr$ ) can be calculated from following equation



$$\text{Pr} = \frac{C_{p,mix}\mu_g}{\lambda_g} \quad \text{Eq. A 23}$$

The  $C_{p,mix}$  and  $\lambda_g$  has been mentioned above.

### A.7. Viscosity

To calculate the viscosity of the gas mixture ( $\mu_g, Pa s$ ), the Wilke method was used as expressed in Eq.A24.

$$\mu_g = \frac{\sum_{i=1}^n y_i \mu_i}{\sum_{j=1}^n y_j \phi_{ij}} \quad \text{Eq. A 24}$$

The binary term ( $\phi_{ij}$ ) can be estimated through the Eq. A25, and viscosity of the pure CH<sub>4</sub>, CO<sub>2</sub>, H<sub>2</sub>O and H<sub>2</sub> species ( $\mu_i$ ) can be determined from Eq.A26 provided by Miguel [71], and CO and Ar can be calculated from Eq.A27 [122], which the coefficients for calculation shown in Table A4.

$$\phi_{ij} = \frac{\left[1 + (\mu_i/\mu_j)^{0.5} (M_i/M_j)^{0.25}\right]^2}{\left[8(1 + M_i/M_j)\right]^{0.5}} \quad \text{Eq. A 25}$$

$$\mu_i = \frac{AT^B}{1 + \frac{C}{T} + \frac{D}{T^2}} \quad \text{Eq. A 26}$$

$$\mu_i = \frac{10^{-6} T^{0.5}}{A + \frac{B}{T} + \frac{C}{T^2} + \frac{D}{T^3}} \quad \text{Eq. A 27}$$

Where  $u_o (ms^{-1})$  is fluid superficial velocity calculated from Eq. A26.

$$\mu_0 = \frac{\sum_{i=1}^n F_i}{A} \times \frac{T}{298.15} \times \frac{1}{P} \quad \text{Eq. A 28}$$

which A (m<sup>2</sup>) is the cross-section area of quartz tube, it can be calculated from  $\pi r^2$ . The density of the gas mixture ( $\rho_g, kgm^{-3}$ ) was calculated from the assumption of ideal gas behavior, as shown in Eq.A29.

$$\rho_g = \frac{P}{RT} \sum_{i=1}^n y_i M_i \quad \text{Eq. A 29}$$

Table A 4. The coefficients A-D used to estimate pure viscosity of each species.

Species	A	B	C	D
CO <sub>2</sub>	2.1480 x 10 <sup>-6</sup>	0.46000	290.000	0
H <sub>2</sub>	1.7970 x 10 <sup>-7</sup>	0.68500	-0.590	140
CH <sub>4</sub>	5.2546 x 10 <sup>-7</sup>	0.59006	105.670	0
H <sub>2</sub> O	1.7096 x 10 <sup>-8</sup>	1.11460	0.000	0
CO	6.6872 x 10 <sup>-1</sup>	70.992	14880	-2.4377x10 <sup>6</sup>
Ar	4.1379 x 10 <sup>-1</sup>	218.56	-72069	1.1639 x 10 <sup>7</sup>

The equation of Table 7 was compiled by Berger[96]. The detail for calculation was displayed as follows.

### A.8. Relative pressure

The pressure drop over the catalyst bed ( $\Delta P$ , Pa) can be estimated from Eq A30.

$$\frac{\Delta P}{H} = \frac{f_m \rho_g u_0^2}{d_p} \quad \text{Eq. A 30}$$

Where  $f_m$  is modified friction factor can be estimated from Eq.S31.

$$f_m = \frac{1 - \varepsilon_p}{\varepsilon_p} \left( 1.75 + 150 \frac{1 - \varepsilon_p}{\text{Re}_p} \right) \quad \text{Eq. A 31}$$

The parameter and equation to determine the Ranold number has been mentioned above.

### A.9. Axial dispersion

To calculate axial dispersion, the Bodenstein number ( $Bo$ ) was used.

$$\frac{1}{Bo} = \frac{\varepsilon_p}{\sqrt{\varepsilon_p} \text{Re}_p \text{Sc}} + 0.5 \quad \text{Eq. A 32}$$

### A.10. inert bed dilution

To assess inert bed dilution, the volumetric dilution ( $b$ ) can be determined with Eq.A33.

$$b = \frac{\frac{w_{inert}}{\rho_{inert}}}{\frac{w_{cat}}{\rho_b} + \frac{w_{inert}}{\rho_{inert}}} \quad \text{Eq. A 33}$$

Where the properties of particles were shown in Table 13.

### A.11. radial thermal conductivity

The effective radial thermal conductivity in the bed catalyst ( $\lambda_{er}, Wm^{-1}K^{-1}$ ) can be examined from the following relationship.

$$\frac{\lambda_{er}}{\lambda_g} = \frac{\lambda_{b,0}}{\lambda_g} + \frac{\lambda_{conv}}{\lambda_g} \quad Eq. A 34$$

The  $\lambda_{conv}$  and  $\lambda_{b,0}$  are a convective contribution to radial thermal conductivity and static contribution effective radial thermal conductivity in-unit  $Wm^{-1}K^{-1}$ . These can be calculated with the ratio of  $\lambda_g$ , as shown in Eq.A35 and A36.

$$\frac{\lambda_{conv}}{\lambda_g} = \frac{Re_p Pr}{8.65 \left[ 1 + 19.4 \left( \frac{d_p}{d_i} \right)^2 \right]} \quad Eq. A 35$$

$$\frac{\lambda_{b,0}}{\lambda_g} = \varepsilon_p + \frac{1 - \varepsilon_p}{0.22\varepsilon_p^2 + \frac{2}{3} \left( \frac{\lambda_g}{\lambda_p} \right)} \quad Eq. A 36$$

Where thermal conductivity of the catalyst particle ( $\lambda_p, Wm^{-1}K^{-1}$ ) can be determined from the relationship of conductivity of the catalyst pellets ( $\lambda_s$ ) and the inert material ( $\lambda_{inert}$ ).

$$\frac{1}{\lambda_p} = \frac{1-b}{\lambda_s} + \frac{b}{\lambda_{inert}} \quad Eq. A 37$$

Where the conductivity of  $\gamma\text{-Al}_2\text{O}_3$  ( $\lambda_{inert}$ ) constant as  $35 Wm^{-1}K^{-1}$  [123].

## APPENDIX B

## EQUILIBRIUM CONVERSION

The thermodynamic equilibrium conversion for Sabatier and RWGS reaction was calculated from following equation [124].

$$K_{c,Sabatier} = \frac{P_{CH_4} P_{H_2O}^2}{P_{H_2}^4 P_{CO_2}} \quad \text{Eq. B 1}$$

$$K_{c,RWGS} = \frac{P_{CO} P_{H_2O}}{P_{H_2} P_{CO_2}} \quad \text{Eq. B 2}$$

Where the equilibrium constant ( $K_c$ ) of each reaction can determine using Eq. B3

$$K_{c,j} = e^{-\frac{\Delta G_j}{RT}} \quad \text{Eq. B 3}$$

The Gibbs free energy change ( $\Delta G$ ) can be examined from different of Gibbs free energies of the products and the reactants.

$$\Delta G_{Sabatier} = G_{CH_4} + 2G_{H_2O} - G_{CO_2} - 4G_{H_2} \quad \text{Eq. B 4}$$

$$\Delta G_{RWGS} = G_{CO} + G_{H_2O} - G_{CO_2} - G_{H_2} \quad \text{Eq. B 5}$$

Gibbs free energy ( $G_i$ , kJ/mol), standard enthalpy ( $H_i$ , kJ/mol) and standard entropy ( $S_i$ , J/molK) are expressed in Eqs. B6 to B8, and polynomial constant for Shomate equation was demonstrated in Table A2.

$$G_i = H_i - TS_i \quad \text{Eq. B 6}$$

$$H_i(T) = H_r^{298K} + AT' + \frac{B}{2}T'^2 + \frac{C}{3}T'^3 + \frac{D}{4}T'^4 - E\frac{1}{T'} + F \quad \text{Eq. B 7}$$

$$S_i(T) = A\ln(T') + BT' + \frac{C}{2}T'^2 + \frac{D}{3}T'^3 - \frac{E}{2T'^2} + G \quad \text{Eq. B 8}$$

The Microsoft Excel add-in program was used to determine output composition by constraining mass balance input equal to output.

## APPENDIX C

## ANALYZE THE DATA

## C.1. GC calibration

Linearity of TCD response for three major compounds, CO, CO<sub>2</sub>, and CH<sub>4</sub>, was confirmed at seven different concentrations (Table C1). Figure C1 shows linear responses for the three compounds.

Table C 1. Feeding gas composition in for GC calibration (mL/min)

	Ar	CH <sub>4</sub> , CO <sub>2</sub> , CO
1	160	40
2	120	80
3	80	120
4	40	160
5	480	20
6	280	20
7	180	20

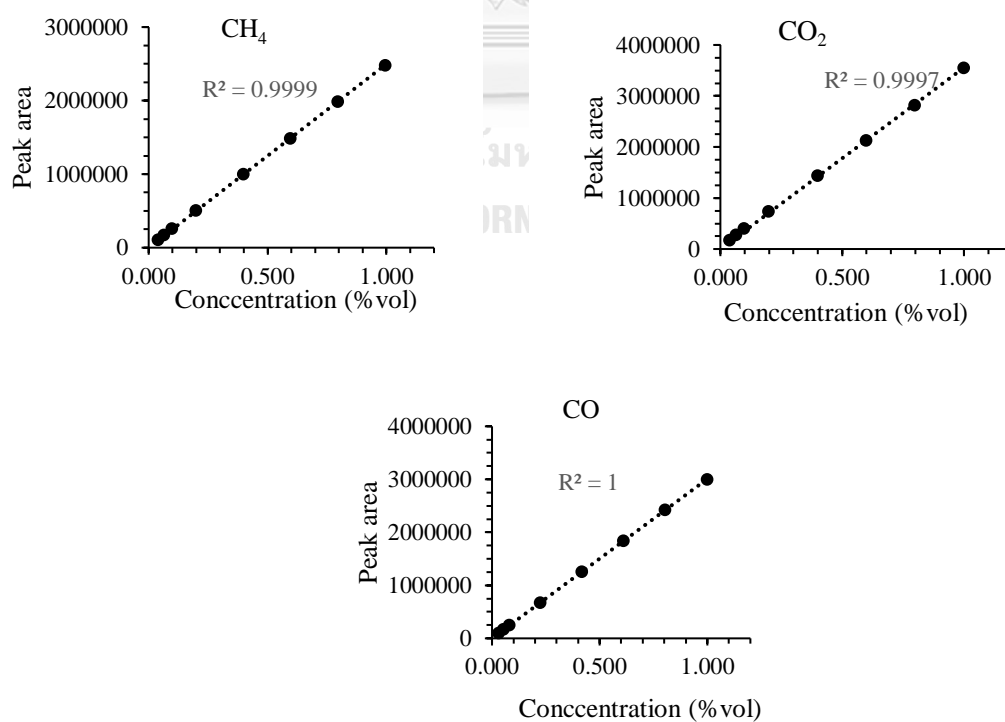


Figure C 1. Calibration curves for CO, CO<sub>2</sub>, and CH<sub>4</sub>

The results showed the relative response factor of CO/Ar = 1.058, CH<sub>4</sub>/Ar = 0.897, and CO<sub>2</sub>/Ar = 1.288

## C2. Calculation the conversion, selectivity, reaction rate, and confidence interval

### CO<sub>2</sub> Conversion

$$X_{CO_2} = \frac{\text{Flow rate of CO}_2 \text{ input } (F_{CO_2,in}) - \text{Flow rate of CO}_2 \text{ output } (F_{CO_2,out})}{\text{Flow rate of CO}_2 \text{ input } (F_{CO_2,in})} * 100$$

Where  $F_{CO_2,out}$  can calculate from

$$\frac{\text{peak area of } \frac{CO_2}{Ar} \times \text{relative response factor of } \frac{CO_2}{Ar}}{F_{Ar}}$$

Note that the output compositions were corrected with the mass balance 100%.

### Selectivity of CH<sub>4</sub>

$$S_{CH_4} = \frac{\text{Flow rate of CH}_4 \text{ out } (F_{CH_4,out})}{\text{Flow rate of total product } (F_{CH_4,out} + F_{CO,out})}$$

### Reaction rate of CH<sub>4</sub>

$$r_{CH_4} = \frac{\Delta F_{CH_4} (\text{mol/min})}{\text{weigh of catalyst } (W_{cat}, g)}$$

### Confidence interval

The confidence interval for nonlinear regression can be calculate from the following equations.

$$95\% C.I. I_{x_{ij}} = T_{value} \times \sqrt{\text{var}(x_{ij})}$$

$$\text{Where } (J^T J)^{-1} \cdot \hat{\sigma}^2 = \begin{bmatrix} \text{var}(x_{11}) & x \\ x & \text{var}(x_{ij}) \end{bmatrix}$$

$(J^T J)^{-1}$  is the inverse of transpose of Jacobian matrix multiplied by that matrix. The variance estimate value ( $\hat{\sigma}^2$ ) can be calculate from  $\frac{SSE}{n-p}$ , where SSE, n, and p stands for sum square error, number of data point, and number of parameters, respectively.

## APPENDIX D

## RESULT

Table D 1. Results from calculation conversion, selectivity, and reaction rate

ID	T <sub>furnace</sub> (°C)	T <sub>Top</sub> (°C)	T <sub>bottom</sub> (°C)	P (MPa)	X <sub>CO2</sub> (-)	S <sub>CH4</sub> (-)	S <sub>CO</sub> (-)	r <sub>CH4</sub> Mol/gs	r <sub>CO</sub> Mol/gs	r <sub>CO2</sub> Mol/gs
01	300	307.1	307.8	0.015	1.93	0.28	0.72	3.86E-06	9.74E-06	-1.36E-05
	300	307.1	308.9	0.402	1.97	0.55	0.45	7.58E-06	6.32E-06	-1.39E-05
	300	307.3	309.2	0.799	2.25	0.69	0.31	1.10E-05	4.84E-06	-1.59E-05
	325	332.5	333.8	0.016	3.98	0.24	0.76	6.84E-06	2.12E-05	-2.80E-05
	325	333.4	334.8	0.402	4.19	0.53	0.47	1.57E-05	1.38E-05	-2.95E-05
	325	333.4	336.0	0.799	4.89	0.69	0.31	2.38E-05	1.07E-05	-3.44E-05
	350	358.4	359.7	0.016	7.90	0.23	0.77	1.30E-05	4.27E-05	-5.57E-05
	350	358.8	362.0	0.401	8.63	0.53	0.47	3.20E-05	2.88E-05	-6.08E-05
	350	358.9	364.3	0.801	10.71	0.68	0.32	5.15E-05	2.39E-05	-7.54E-05
02	300	307.1	308.1	0.014	1.51	0.24	0.76	3.44E-06	1.08E-05	-1.43E-05
	300	307.3	309.1	0.401	1.67	0.56	0.44	8.89E-06	6.91E-06	-1.58E-05
	300	307.2	309.5	0.800	1.91	0.71	0.29	1.29E-05	5.19E-06	-1.81E-05
	325	333.2	333.8	0.015	3.24	0.24	0.76	7.45E-06	2.32E-05	-3.07E-05
	325	333.4	335.4	0.404	3.64	0.55	0.45	1.90E-05	1.54E-05	-3.44E-05
	325	333.5	336.6	0.800	4.30	0.70	0.30	2.86E-05	1.20E-05	-4.06E-05
	350	358.7	359.2	0.016	6.34	0.23	0.77	1.36E-05	4.63E-05	-6.00E-05
	350	358.9	362.5	0.401	7.59	0.55	0.45	3.94E-05	3.24E-05	-7.18E-05
	350	358.9	365.4	0.800	9.59	0.70	0.30	6.37E-05	2.70E-05	-9.07E-05
03	300	307.4	308.6	0.012	1.32	0.25	0.75	4.01E-06	1.21E-05	-1.61E-05
	300	307.4	309.2	0.399	1.46	0.58	0.42	1.03E-05	7.56E-06	-1.79E-05
	300	307.5	309.9	0.802	1.70	0.72	0.28	1.49E-05	5.78E-06	-2.07E-05
	325	333.3	334.0	0.013	2.79	0.24	0.76	8.14E-06	2.59E-05	-3.41E-05
	325	333.6	335.5	0.401	3.18	0.57	0.43	2.20E-05	1.69E-05	-3.89E-05
	325	333.5	336.7	0.802	3.78	0.72	0.28	3.31E-05	1.31E-05	-4.62E-05
	350	358.8	359.6	0.014	5.56	0.23	0.77	1.59E-05	5.20E-05	-6.79E-05
	350	358.9	363.0	0.402	6.78	0.56	0.44	4.65E-05	3.63E-05	-8.28E-05
	350	359.5	366.3	0.800	8.68	0.71	0.29	7.55E-05	3.05E-05	-1.06E-04
04	300	308.4	307.9	0.013	3.07	0.98	0.02	1.76E-05	1.04E-05	-2.80E-05
	300	308.6	308.6	0.401	3.11	0.99	0.01	2.07E-05	7.66E-06	-2.83E-05
	300	308.7	308.9	0.801	3.46	0.99	0.01	2.48E-05	6.75E-06	-3.16E-05
	325	334.5	334.3	0.013	4.05	0.97	0.03	1.53E-05	2.16E-05	-3.69E-05
	325	334.1	334.7	0.402	4.24	0.98	0.02	2.25E-05	1.61E-05	-3.86E-05
	325	333.9	335.4	0.800	4.54	0.98	0.02	2.73E-05	1.41E-05	-4.14E-05
	350	359.6	359.8	0.013	6.34	0.94	0.06	1.62E-05	4.15E-05	-5.78E-05

ID	T <sub>furnace</sub> (°C)	T <sub>Top</sub> (°C)	T <sub>bottom</sub> (°C)	P (MPa)	X <sub>CO2</sub> (-)	S <sub>CH4</sub> (-)	S <sub>CO</sub> (-)	r <sub>CH4</sub> Mol/gs	r <sub>CO</sub> Mol/gs	r <sub>CO2</sub> Mol/gs
	350	359.0	361.3	0.402	6.89	0.96	0.04	3.10E-05	3.18E-05	-6.28E-05
	350	359.1	363.0	0.801	8.15	0.96	0.04	4.65E-05	2.78E-05	-7.43E-05
	300	308.3	307.3	0.015	2.47	0.99	0.01	8.69E-06	8.69E-06	-1.74E-05
	300	308.7	308.1	0.401	2.51	0.99	0.01	1.10E-05	6.72E-06	-1.77E-05
	300	308.6	308.4	0.802	2.87	0.99	0.01	1.45E-05	5.72E-06	-2.02E-05
	325	334.5	333.9	0.014	3.59	0.97	0.03	6.21E-06	1.91E-05	-2.53E-05
05	325	334.0	334.3	0.402	4.19	0.98	0.02	1.55E-05	1.40E-05	-2.95E-05
	325	333.9	335.2	0.798	4.89	0.98	0.02	2.27E-05	1.17E-05	-3.44E-05
	350	359.1	358.8	0.015	6.11	0.95	0.05	9.30E-06	3.37E-05	-4.30E-05
	350	359.1	361.0	0.400	7.86	0.96	0.04	2.84E-05	2.69E-05	-5.54E-05
	350	359.1	362.9	0.799	9.67	0.97	0.03	4.48E-05	2.33E-05	-6.81E-05
	300	308.3	308.0	0.012	2.60	0.99	0.01	9.96E-06	8.38E-06	-1.83E-05
	300	308.6	308.8	0.400	2.99	0.99	0.01	1.47E-05	6.43E-06	-2.11E-05
	300	308.4	309.0	0.801	3.66	0.99	0.01	1.99E-05	5.86E-06	-2.57E-05
	325	333.9	334.2	0.012	3.78	0.98	0.02	9.35E-06	1.73E-05	-2.66E-05
06	325	333.9	335.0	0.401	4.96	0.99	0.01	2.13E-05	1.36E-05	-3.49E-05
	325	333.8	335.6	0.800	6.00	0.99	0.01	3.06E-05	1.17E-05	-4.22E-05
	350	359.2	359.8	0.013	5.78	0.97	0.03	9.75E-06	3.10E-05	-4.07E-05
	350	359.1	361.3	0.400	7.57	0.98	0.02	2.86E-05	2.47E-05	-5.33E-05
	350	358.9	363.2	0.802	9.64	0.98	0.02	4.60E-05	2.19E-05	-6.79E-05
	300	308.3	307.9	0.012	1.09	0.99	0.01	-9.08E-07	7.06E-06	-6.16E-06
	300	308.1	308.3	0.402	2.55	1.00	0.00	8.41E-06	6.03E-06	-1.44E-05
	300	307.5	308.9	0.799	4.00	1.00	0.00	1.73E-05	5.31E-06	-2.27E-05
	325	334.1	334.6	0.013	2.61	0.99	0.01	1.57E-06	1.32E-05	-1.48E-05
07	325	333.7	334.6	0.402	4.18	0.99	0.01	1.26E-05	1.11E-05	-2.37E-05
	325	333.1	335.1	0.800	6.23	0.99	0.01	2.52E-05	1.01E-05	-3.53E-05
	350	359.2	359.6	0.013	5.24	0.98	0.02	8.34E-06	2.13E-05	-2.97E-05
	350	358.7	360.2	0.402	6.75	0.99	0.01	2.00E-05	1.83E-05	-3.82E-05
	350	358.6	361.7	0.793	8.30	0.99	0.01	3.00E-05	1.70E-05	-4.70E-05
	300	308.1	307.6	0.017	1.04	0.13	0.87	2.38E-06	1.53E-05	-1.77E-05
	300	308.1	308.6	0.401	1.01	0.35	0.65	6.02E-06	1.12E-05	-1.72E-05
	300	307.8	309.3	0.800	1.06	0.49	0.51	8.91E-06	9.23E-06	-1.81E-05
	325	333.4	333.9	0.018	2.25	0.14	0.86	5.23E-06	3.32E-05	-3.84E-05
08	325	333.4	334.8	0.401	2.23	0.35	0.65	1.32E-05	2.47E-05	-3.79E-05
	325	333.1	335.8	0.800	2.41	0.48	0.52	2.00E-05	2.12E-05	-4.11E-05
	350	358.6	358.2	0.019	4.36	0.13	0.87	1.00E-05	6.44E-05	-7.44E-05
	350	358.4	361.0	0.400	4.60	0.34	0.66	2.70E-05	5.14E-05	-7.84E-05
	350	358.1	363.8	0.799	5.22	0.48	0.52	4.29E-05	4.62E-05	-8.91E-05
	300	308.2	308.0	0.015	0.83	0.15	0.85	3.13E-06	1.82E-05	-2.13E-05
	300	308.0	308.8	0.401	0.81	0.37	0.63	7.61E-06	1.31E-05	-2.07E-05
	300	307.9	309.8	0.800	0.88	0.51	0.49	1.15E-05	1.11E-05	-2.26E-05
	325	334.1	334.4	0.016	1.82	0.15	0.85	7.03E-06	3.96E-05	-4.67E-05
	325	333.4	335.5	0.399	1.83	0.37	0.63	1.75E-05	2.94E-05	-4.69E-05



ID	T <sub>furnace</sub> (°C)	T <sub>Top</sub> (°C)	T <sub>bottom</sub> (°C)	P (MPa)	X <sub>CO2</sub> (-)	S <sub>CH4</sub> (-)	S <sub>CO</sub> (-)	r <sub>CH4</sub> Mol/gs	r <sub>CO</sub> Mol/gs	r <sub>CO2</sub> Mol/gs
09	325	333.3	336.8	0.800	2.03	0.52	0.48	2.70E-05	2.52E-05	-5.21E-05
	350	359.0	359.5	0.017	3.60	0.15	0.85	1.39E-05	7.86E-05	-9.25E-05
	350	358.5	362.6	0.402	3.90	0.37	0.63	3.75E-05	6.27E-05	-1.00E-04
	350	358.5	366.2	0.801	4.63	0.52	0.48	6.15E-05	5.74E-05	-1.19E-04
10	300	308.3	307.8	0.018	1.64	0.15	0.85	1.71E-06	9.86E-06	-1.16E-05
	300	308.1	308.3	0.401	1.57	0.37	0.63	4.16E-06	6.93E-06	-1.11E-05
	300	308.0	308.7	0.799	1.69	0.52	0.48	6.16E-06	5.74E-06	-1.19E-05
	325	333.6	333.9	0.019	3.61	0.15	0.85	3.86E-06	2.15E-05	-2.54E-05
	325	333.4	334.5	0.401	3.49	0.37	0.63	9.09E-06	1.55E-05	-2.46E-05
	325	333.2	335.7	0.800	3.78	0.51	0.49	1.36E-05	1.30E-05	-2.66E-05
	350	358.6	359.1	0.020	6.92	0.15	0.85	7.37E-06	4.13E-05	-4.87E-05
	350	358.6	360.4	0.401	6.39	0.37	0.63	1.66E-05	2.84E-05	-4.50E-05
	350	358.4	362.2	0.802	7.93	0.51	0.49	2.85E-05	2.73E-05	-5.58E-05
	300	308.4	308.4	0.017	1.27	0.18	0.82	2.59E-06	1.21E-05	-1.46E-05
	300	308.1	308.6	0.404	1.30	0.43	0.57	6.37E-06	8.60E-06	-1.50E-05
	11	300	308.0	309.2	0.800	1.38	0.57	0.43	9.03E-06	6.92E-06
325		333.9	333.7	0.018	2.84	0.18	0.82	5.94E-06	2.68E-05	-3.27E-05
325		333.5	334.9	0.402	2.86	0.42	0.58	1.39E-05	1.90E-05	-3.29E-05
325		333.5	336.0	0.801	3.16	0.57	0.43	2.07E-05	1.58E-05	-3.65E-05
350		358.5	359.1	0.019	5.59	0.18	0.82	1.15E-05	5.29E-05	-6.45E-05
350		358.7	361.6	0.401	5.97	0.42	0.58	2.89E-05	3.99E-05	-6.88E-05
350		358.6	363.8	0.801	6.91	0.56	0.44	4.47E-05	3.50E-05	-7.97E-05
300		308.3	308.1	0.015	1.52	0.22	0.78	2.86E-06	9.94E-06	-1.28E-05
12	300	308.6	308.7	0.401	1.51	0.49	0.51	6.17E-06	6.52E-06	-1.27E-05
	300	308.5	309.0	0.801	1.65	0.62	0.38	8.58E-06	5.32E-06	-1.39E-05
	325	334.0	334.2	0.016	3.37	0.23	0.77	6.50E-06	2.18E-05	-2.84E-05
	325	333.9	334.8	0.402	3.37	0.49	0.51	1.40E-05	1.44E-05	-2.84E-05
	325	333.9	335.6	0.801	3.79	0.63	0.37	2.00E-05	1.19E-05	-3.19E-05
	350	359.2	359.4	0.016	6.71	0.23	0.77	1.30E-05	4.35E-05	-5.65E-05
	350	359.0	361.7	0.401	7.17	0.50	0.50	3.01E-05	3.03E-05	-6.04E-05
	350	359.1	363.3	0.800	8.30	0.64	0.36	4.48E-05	2.51E-05	-6.99E-05
13	300	308.0	308.0	0.015	2.03	0.98	0.02	2.08E-05	1.39E-05	-3.47E-05
	300	308.0	308.5	0.400	1.78	0.98	0.02	1.88E-05	1.14E-05	-3.03E-05
	300	307.6	308.8	0.801	1.97	0.99	0.01	2.31E-05	1.05E-05	-3.36E-05
	325	333.9	334.1	0.016	2.69	0.96	0.04	1.72E-05	2.87E-05	-4.58E-05
	325	333.2	334.5	0.400	2.78	0.97	0.03	2.39E-05	2.36E-05	-4.74E-05
	325	333.1	335.3	0.799	3.09	0.97	0.03	3.13E-05	2.14E-05	-5.27E-05
	350	358.9	359.1	0.016	4.37	0.93	0.07	2.11E-05	5.35E-05	-7.46E-05
	350	358.3	360.9	0.401	4.74	0.94	0.06	3.63E-05	4.45E-05	-8.08E-05
	350	358.2	363.1	0.799	5.46	0.95	0.05	5.20E-05	4.12E-05	-9.32E-05
	300	308.6	307.5	0.014	2.68	0.98	0.02	3.28E-05	1.30E-05	-4.57E-05
300	308.4	308.1	0.400	2.31	0.98	0.02	2.85E-05	1.09E-05	-3.94E-05	
300	308.2	308.5	0.802	2.37	0.99	0.01	2.98E-05	1.05E-05	-4.03E-05	

ID	T <sub>furnace</sub> (°C)	T <sub>Top</sub> (°C)	T <sub>bottom</sub> (°C)	P (MPa)	X <sub>CO2</sub> (-)	S <sub>CH4</sub> (-)	S <sub>CO</sub> (-)	r <sub>CH4</sub> Mol/gs	r <sub>CO</sub> Mol/gs	r <sub>CO2</sub> Mol/gs
14	325	334.7	333.7	0.014	3.00	0.96	0.04	2.49E-05	2.64E-05	-5.12E-05
	325	334.0	333.9	0.400	3.03	0.97	0.03	2.95E-05	2.23E-05	-5.17E-05
	325	333.9	334.9	0.801	3.31	0.97	0.03	3.57E-05	2.07E-05	-5.64E-05
	350	359.5	358.7	0.015	4.20	0.94	0.06	2.56E-05	4.60E-05	-7.16E-05
	350	359.0	360.3	0.401	4.66	0.95	0.05	3.89E-05	4.06E-05	-7.94E-05
	350	358.8	362.5	0.799	5.34	0.95	0.05	5.31E-05	3.80E-05	-9.11E-05

Table D 2. Experimental data and prediction data from hybrid model

ID	r <sub>CH4</sub>		r <sub>CO</sub>		r <sub>CO2</sub>	
	Exp. data	Pred.data	Exp. data	Pred.data	Exp. data	Pred.data
01	3.9E-06	3.8E-06	9.7E-06	9.7E-06	1.4E-05	1.3E-05
	7.6E-06	9.2E-06	6.3E-06	7.3E-06	1.4E-05	1.6E-05
	1.1E-05	1.2E-05	4.8E-06	6.5E-06	1.6E-05	1.9E-05
	6.8E-06	6.4E-06	2.1E-05	2.0E-05	2.8E-05	2.7E-05
	1.6E-05	1.7E-05	1.4E-05	1.5E-05	2.9E-05	3.3E-05
	2.4E-05	2.4E-05	1.1E-05	1.4E-05	3.4E-05	3.8E-05
	1.3E-05	9.9E-06	4.3E-05	4.0E-05	5.6E-05	5.0E-05
	3.2E-05	3.0E-05	2.9E-05	3.1E-05	6.1E-05	6.0E-05
02	3.4E-06	4.7E-06	1.1E-05	8.9E-06	1.4E-05	1.4E-05
	8.9E-06	1.1E-05	6.9E-06	6.7E-06	1.6E-05	1.7E-05
	1.3E-05	1.4E-05	5.2E-06	6.0E-06	1.8E-05	2.0E-05
	7.4E-06	8.1E-06	2.3E-05	1.9E-05	3.1E-05	2.7E-05
	1.9E-05	2.1E-05	1.5E-05	1.4E-05	3.4E-05	3.5E-05
	2.9E-05	2.9E-05	1.2E-05	1.3E-05	4.1E-05	4.2E-05
	1.4E-05	1.3E-05	4.6E-05	3.6E-05	6.0E-05	4.9E-05
	3.9E-05	3.7E-05	3.2E-05	2.8E-05	7.2E-05	6.5E-05
03	4.0E-06	5.5E-06	1.2E-05	8.5E-06	1.6E-05	1.4E-05
	1.0E-05	1.2E-05	7.6E-06	6.3E-06	1.8E-05	1.8E-05
	1.5E-05	1.5E-05	5.8E-06	5.7E-06	2.1E-05	2.1E-05
	8.1E-06	9.6E-06	2.6E-05	1.8E-05	3.4E-05	2.7E-05
	2.2E-05	2.4E-05	1.7E-05	1.3E-05	3.9E-05	3.8E-05
	3.3E-05	3.3E-05	1.3E-05	1.2E-05	4.6E-05	4.5E-05
	1.6E-05	1.5E-05	5.2E-05	3.5E-05	6.8E-05	5.0E-05
	4.6E-05	4.3E-05	3.6E-05	2.7E-05	8.3E-05	7.0E-05
04	1.8E-05	4.6E-06	1.0E-05	9.9E-06	2.8E-05	1.5E-05
	2.1E-05	1.1E-05	7.7E-06	7.5E-06	2.8E-05	1.8E-05
	2.5E-05	1.4E-05	6.7E-06	6.7E-06	3.2E-05	2.0E-05
	1.5E-05	7.9E-06	2.2E-05	2.0E-05	3.7E-05	2.8E-05
	2.3E-05	2.1E-05	1.6E-05	1.5E-05	3.9E-05	3.6E-05
	2.7E-05	2.8E-05	1.4E-05	1.3E-05	4.1E-05	4.2E-05
	1.6E-05	1.2E-05	4.1E-05	3.6E-05	5.8E-05	4.8E-05

ID	rCH4		rCO		rCO2	
	Exp. data	Pred.data	Exp. data	Pred.data	Exp. data	Pred.data
	3.1E-05	3.6E-05	3.2E-05	2.8E-05	6.3E-05	6.3E-05
	4.6E-05	5.1E-05	2.8E-05	2.5E-05	7.4E-05	7.7E-05
05	8.7E-06	3.8E-06	8.7E-06	1.0E-05	1.7E-05	1.4E-05
	1.1E-05	9.3E-06	6.7E-06	7.9E-06	1.8E-05	1.7E-05
	1.5E-05	1.2E-05	5.7E-06	7.1E-06	2.0E-05	1.9E-05
	6.2E-06	6.5E-06	1.9E-05	2.0E-05	2.5E-05	2.6E-05
	1.6E-05	1.7E-05	1.4E-05	1.5E-05	2.9E-05	3.3E-05
	2.3E-05	2.4E-05	1.2E-05	1.4E-05	3.4E-05	3.8E-05
	9.3E-06	9.8E-06	3.4E-05	3.5E-05	4.3E-05	4.5E-05
	2.8E-05	2.9E-05	2.7E-05	2.8E-05	5.5E-05	5.7E-05
	4.5E-05	4.3E-05	2.3E-05	2.6E-05	6.8E-05	6.9E-05
	06	1.0E-05	3.8E-06	8.4E-06	1.0E-05	1.8E-05
1.5E-05		9.3E-06	6.4E-06	7.7E-06	2.1E-05	1.7E-05
2.0E-05		1.2E-05	5.9E-06	6.9E-06	2.6E-05	1.9E-05
9.4E-06		6.4E-06	1.7E-05	1.9E-05	2.7E-05	2.5E-05
2.1E-05		1.7E-05	1.4E-05	1.5E-05	3.5E-05	3.2E-05
3.1E-05		2.4E-05	1.2E-05	1.3E-05	4.2E-05	3.8E-05
9.7E-06		9.8E-06	3.1E-05	3.2E-05	4.1E-05	4.2E-05
2.9E-05		2.9E-05	2.5E-05	2.6E-05	5.3E-05	5.5E-05
4.6E-05		4.3E-05	2.2E-05	2.4E-05	6.8E-05	6.8E-05
07	8.4E-06	8.2E-06	6.0E-06	7.2E-06	1.4E-05	1.5E-05
	1.7E-05	1.1E-05	5.3E-06	6.6E-06	2.3E-05	1.7E-05
	1.6E-06	5.4E-06	1.3E-05	1.7E-05	1.5E-05	2.3E-05
	1.3E-05	1.5E-05	1.1E-05	1.3E-05	2.4E-05	2.9E-05
	2.5E-05	2.1E-05	1.0E-05	1.2E-05	3.5E-05	3.4E-05
	8.3E-06	8.1E-06	2.1E-05	2.9E-05	3.0E-05	3.7E-05
	2.0E-05	2.5E-05	1.8E-05	2.3E-05	3.8E-05	4.8E-05
	3.0E-05	3.7E-05	1.7E-05	2.2E-05	4.7E-05	5.9E-05
08	2.4E-06	4.5E-06	1.5E-05	1.7E-05	1.8E-05	2.1E-05
	6.0E-06	1.0E-05	1.1E-05	1.3E-05	1.7E-05	2.3E-05
	8.9E-06	1.3E-05	9.2E-06	1.1E-05	1.8E-05	2.4E-05
	5.2E-06	7.6E-06	3.3E-05	3.5E-05	3.8E-05	4.3E-05
	1.3E-05	1.9E-05	2.5E-05	2.6E-05	3.8E-05	4.6E-05
	2.0E-05	2.6E-05	2.1E-05	2.4E-05	4.1E-05	5.0E-05
	1.0E-05	1.2E-05	6.4E-05	6.7E-05	7.4E-05	7.9E-05
	2.7E-05	3.3E-05	5.1E-05	5.2E-05	7.8E-05	8.5E-05
09	7.0E-06	1.0E-05	4.0E-05	3.3E-05	4.7E-05	4.3E-05
	1.7E-05	2.4E-05	2.9E-05	2.4E-05	4.7E-05	4.9E-05
	2.7E-05	3.3E-05	2.5E-05	2.2E-05	5.2E-05	5.5E-05
	1.4E-05	1.6E-05	7.9E-05	6.3E-05	9.2E-05	7.9E-05
	3.7E-05	4.3E-05	6.3E-05	4.9E-05	1.0E-04	9.1E-05
	1.7E-06	3.1E-06	9.9E-06	1.4E-05	1.2E-05	1.8E-05
	4.2E-06	7.7E-06	6.9E-06	1.1E-05	1.1E-05	1.8E-05

ID	rCH4		rCO		rCO2	
	Exp. data	Pred.data	Exp. data	Pred.data	Exp. data	Pred.data
10	6.2E-06	1.0E-05	5.7E-06	9.6E-06	1.2E-05	2.0E-05
	3.9E-06	5.1E-06	2.2E-05	3.0E-05	2.5E-05	3.5E-05
	9.1E-06	1.4E-05	1.6E-05	2.3E-05	2.5E-05	3.7E-05
	1.4E-05	2.0E-05	1.3E-05	2.0E-05	2.7E-05	4.1E-05
	7.4E-06	7.5E-06	4.1E-05	5.8E-05	4.9E-05	6.5E-05
	1.7E-05	2.3E-05	2.8E-05	4.4E-05	4.5E-05	6.7E-05
	2.9E-05	3.4E-05	2.7E-05	4.0E-05	5.6E-05	7.4E-05
11	2.6E-06	4.4E-06	1.2E-05	1.3E-05	1.5E-05	1.7E-05
	6.4E-06	1.0E-05	8.6E-06	9.5E-06	1.5E-05	2.0E-05
	9.0E-06	1.3E-05	6.9E-06	8.6E-06	1.6E-05	2.2E-05
	5.9E-06	7.4E-06	2.7E-05	2.7E-05	3.3E-05	3.4E-05
	1.4E-05	1.9E-05	1.9E-05	2.0E-05	3.3E-05	3.9E-05
	2.1E-05	2.7E-05	1.6E-05	1.8E-05	3.6E-05	4.5E-05
	1.2E-05	1.1E-05	5.3E-05	5.1E-05	6.4E-05	6.3E-05
	2.9E-05	3.2E-05	4.0E-05	4.0E-05	6.9E-05	7.2E-05
12	4.5E-05	4.7E-05	3.5E-05	3.7E-05	8.0E-05	8.4E-05
	2.9E-06	4.7E-06	9.9E-06	8.3E-06	1.3E-05	1.3E-05
	6.2E-06	1.1E-05	6.5E-06	6.2E-06	1.3E-05	1.7E-05
	8.6E-06	1.4E-05	5.3E-06	5.6E-06	1.4E-05	1.9E-05
	6.5E-06	8.2E-06	2.2E-05	1.8E-05	2.8E-05	2.6E-05
	1.4E-05	2.1E-05	1.4E-05	1.3E-05	2.8E-05	3.4E-05
	2.0E-05	2.8E-05	1.2E-05	1.2E-05	3.2E-05	4.0E-05
	1.3E-05	1.3E-05	4.4E-05	3.4E-05	5.6E-05	4.7E-05
	3.0E-05	3.6E-05	3.0E-05	2.6E-05	6.0E-05	6.2E-05
13	4.5E-05	5.2E-05	2.5E-05	2.4E-05	7.0E-05	7.6E-05
	2.1E-05	4.4E-06	1.4E-05	1.7E-05	3.5E-05	2.2E-05
	1.9E-05	1.0E-05	1.1E-05	1.3E-05	3.0E-05	2.3E-05
	2.3E-05	1.3E-05	1.0E-05	1.2E-05	3.4E-05	2.5E-05
	1.7E-05	7.5E-06	2.9E-05	3.3E-05	4.6E-05	4.1E-05
	2.4E-05	1.9E-05	2.4E-05	2.5E-05	4.8E-05	4.4E-05
	3.1E-05	2.6E-05	2.1E-05	2.3E-05	5.3E-05	4.9E-05
	2.1E-05	1.2E-05	5.3E-05	5.7E-05	7.5E-05	6.9E-05
	3.6E-05	3.3E-05	4.4E-05	4.5E-05	8.1E-05	7.8E-05
14	5.2E-05	4.7E-05	4.1E-05	4.2E-05	9.3E-05	8.9E-05
	3.3E-05	4.4E-06	1.3E-05	1.7E-05	4.6E-05	2.1E-05
	2.9E-05	1.0E-05	1.1E-05	1.3E-05	3.9E-05	2.3E-05
	3.0E-05	1.3E-05	1.0E-05	1.1E-05	4.0E-05	2.4E-05
	2.5E-05	7.4E-06	2.6E-05	3.1E-05	5.1E-05	3.8E-05
	2.9E-05	1.9E-05	2.2E-05	2.4E-05	5.2E-05	4.3E-05
	3.6E-05	2.6E-05	2.1E-05	2.2E-05	5.6E-05	4.8E-05
	2.6E-05	1.1E-05	4.6E-05	5.3E-05	7.2E-05	6.4E-05
	3.9E-05	3.3E-05	4.1E-05	4.1E-05	7.9E-05	7.4E-05
5.3E-05	4.7E-05	3.8E-05	3.9E-05	9.1E-05	8.6E-05	

## APPENDIX E

## PYTHON CODE FOR PARAMETER ESTIMATION

```

# Import the package
import matplotlib.pyplot as plt
import numpy as np
from lmfit import minimize, Parameters, Parameter, report_fit, Minimizer
#load csv. file and name the column with script the first raw.
load = "01_input_using dataThesis.csv"
date, yCOi, yCH4i, yCO2i, yH2Oi, yH2i, yAri, Pt, T, rCH4, rCO = np.loadtxt(load,
skiprows=1, delimiter=',', unpack=True)
#Define parameters and reaction rate
def fn(params):
    k0    = params['k0']
    Ea    = params['Ea']
    k02   = params['k02']
    Ea2   = params['Ea2']
    AH2   = params['AH2']
    HH2   = params['HH2']
    Amix  =params['Amix']
    Hmix  =params['Hmix']
    nH22  =params['nH22']
    nCO22 =params['nCO22']
    nH2O2 =params['nH2O2']
    yt = yH2i + yCO2i + yCH4i + yH2Oi + yAri +yCOi #mol s-1
    pH2 = yH2i / yt * Pt #bar
    pCO2 = yCO2i / yt * Pt #bar
    pCH4 = yCH4i / yt * Pt #bar
    pH2O = yH2Oi / yt * Pt #bar
    pCO = yCOi / yt * Pt
    Tref = 555
    #reference temperature, K
    R = 0.008314 #gas constant, kJ mol-1 K-1
    Keq = 137 * T**-3.998 * np.exp(158.7 / (R * T ))
    Keq2 = 1/(np.exp(4577.8 /T -4.33))
    k = k0 * np.exp(Ea / R * (1/Tref - 1/T))
    k2 = k02 * np.exp(Ea2 / R * (1/Tref - 1/T))
    KH2 = AH2 * np.exp(HH2 / R * (1/Tref - 1/T))
    Kmix = Amix * np.exp(Hmix / R * (1/Tref - 1/T))
# #NO 8
a,b,c,d,e,f,g,h,i = 0.5, 0.5, 0.5, 0, 0.5, 0 ,0 ,0 , 2.0

```

```

r_Sabatier = k * Kmix * pCO2**a * KH2**b * pH2**c * pH2O**d * (1 - pCH4 *
pH2O**2 / (pCO2 * pH2**4 * Keq)) / (1 + Kmix * pCO2**e * KH2**f * pH2**g
*pH2O**h + (KH2 * pH2)**0.5)**i
r_RWGs = k2 * pH2**nH22 * pCO2**nCO22 / pH2O**nH2O2 * (1 - pCO *
pH2O / (pCO2 * pH2 * Keq2))
rCH4_mol = r_Sabatier
rCO_mol = r_RWGs
rCH4_data = rCH4
rCO_data = rCO
rCO2_data = rCH4_data + rCO_data
rCO2_mol = r_Sabatier + r_RWGs
#save to csv file name "test"
save = np.array(( rCH4_data , rCH4_mol, rCO_data , rCO_mol ,rCO2_data ,
rCO2_mol))
export = save.T
np.savetxt('test.csv', export, delimiter=',')
#return residual of rCO, rCH4, and rCO2
return [rCO_mol - rCO_data , rCH4_mol - rCH4_data, rCO2_mol - rCO2_data]
#initial parameters
k0 = 4.9402e-05 #at 555K, mol bar-1 s-1 g-cat-1
Ea = 115.362325 #kJ mol-1
k02 = 9.5839e-06 #at 555K, mol bar-1 s-1 g-cat-1
Ea2 = 93.4965894 #kJ mol-1
AH2 = 0.40042010#at 555K, bar-0.5
HH2 = -88.7961896 # kJ mol-1
Amix = 0.80772168 #at 555K, bar-0.5
Hmix = -34.6318977 #kJ mol-1
nH22 = -0.73090135 #at 555K, bar-0.5
nCO22 = 0.25753538#kJ mol-1
nH2O2 = -0.22874363 #at 555K, bar-0.5
# HCO = 22.4 #kJ mol-1
params = Parameters()
#parameters is dictionary containing the model parameters
params.add('k0', value=k0, vary=False)
params.add('Ea', value=Ea, vary=False)
params.add('k02', value=k02)
params.add('Ea2', value=Ea2)
params.add('AH2', value=AH2, vary=False)
params.add('HH2', value=HH2, vary=False)
params.add('Amix', value=Amix, vary=False)
params.add('Hmix', value=Hmix, vary=False)
params.add('nH22', value=nH22)
params.add('nCO22', value=nCO22)
params.add('nH2O2', value=nH2O2)
result = minimize(fn, params, method='leastsq')
report_fit(result)
#Plotting the results

```

```

import pandas as pd
want = pd.read_csv('test.csv', names=["rCH4_data" , "rCH4_mol" , "rCO_data" ,
"rCO_mol" , "rCO2_data" , "rCO2_mol"],
delimeter=',')
plt.figure(figsize=(8,6))
plt.scatter(want['rCH4_data']*100000, want['rCH4_mol']*100000)
plt.xlabel(r"rCH4_data ( $\times 10^{64}$ )", fontsize=14)
plt.ylabel(r"rCH4_mol ( $\times 10^{-6}$ 
$)", fontsize=14)
plt.plot([0 ,10], [0, 10], 'k')
plt.xlim(0, 9)
plt.ylim(0, 9)

plt.figure(figsize=(8,6))
plt.scatter(want['rCO_data']*100000, want['rCO_mol']*100000)
plt.xlabel(r"rCO_data ( $\times 10^{-6}$ )", fontsize=14)
plt.ylabel(r"rCO_mol ( $\times 10^{-6}$ )", fontsize=14)
plt.plot([0 ,10], [0, 10], 'k')
plt.xlim(0, 9)
plt.ylim(0, 9)

plt.figure(figsize=(8,6))
plt.scatter(want['rCO2_data']*100000, want['rCO2_mol']*100000)
plt.xlabel(r"rCO2_data ( $\times 10^{-6}$ )", fontsize=14)
plt.ylabel(r"rCO2_mol ( $\times 10^{-6}$ )", fontsize=14)
plt.plot([0 ,20], [0, 20], 'k')
plt.xlim(0, 20)
plt.ylim(0, 20)

```

## APPENDIX F

## APPARATUS DIAGRAM

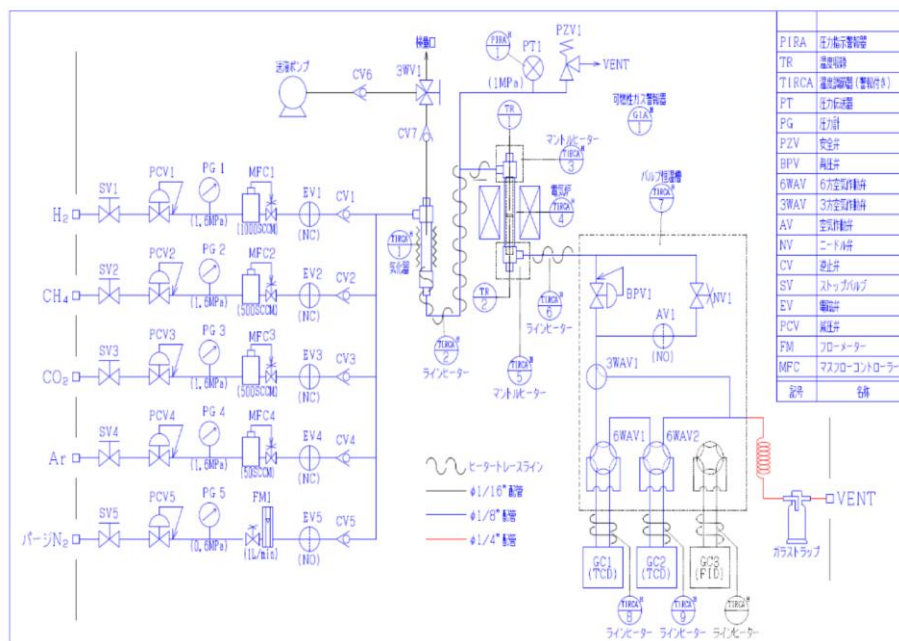


Figure F 1. Apparatus diagram



Figure F 2. Experimental apparatus



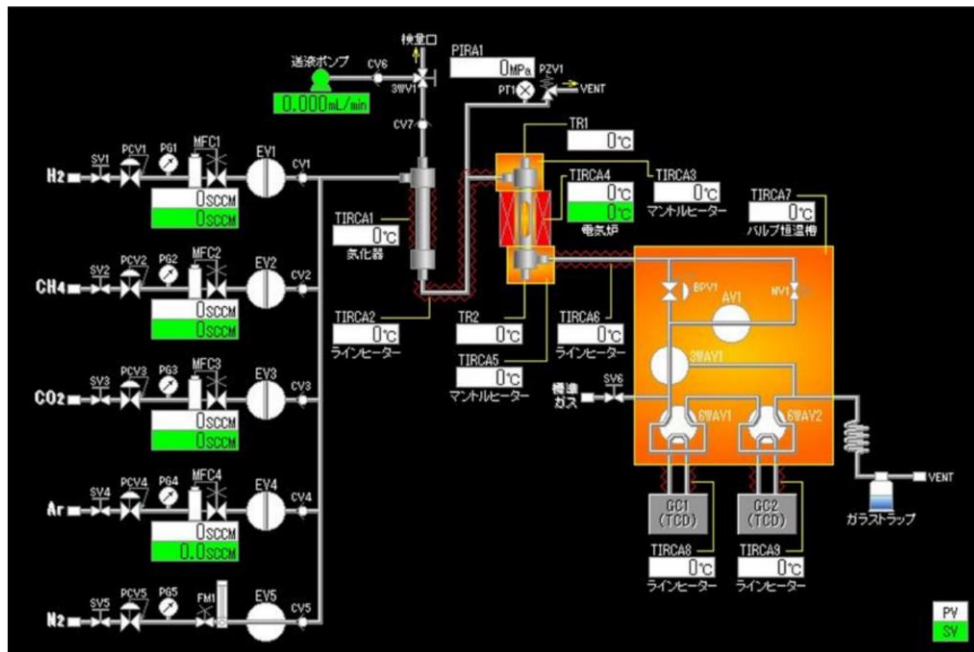


Figure F 3. Monitor to investigate the status of reaction condition

## REFERENCES

1. Rebecca L. *Climate Change: Atmospheric Carbon Dioxide*. 2020 [cited 2021 9/3]; Available from: <https://www.climate.gov/news-features/understanding-climate/climate-change-atmospheric-carbon-dioxide>.
2. Jackson R., Le Quéré C., Andrew R., Canadell J., Peters G., Roy J., and Wu L., *Warning signs for stabilizing global CO<sub>2</sub> emissions*. Environmental Research Letters, 2017. **12**(11): p. 110202.
3. Farooqi A.S., Al-Swai B.M., Ruslan F.H., Mohd Zabidi N.A., Saidur R., Syed Muhammad S.A.F.a., and Abdullah B., *Catalytic conversion of greenhouse gases (CO<sub>2</sub> and CH<sub>4</sub>) to syngas over Ni-based catalyst: Effects of Ce-La promoters*. Arabian Journal of Chemistry, 2020. **13**(6): p. 5740-5749.
4. Swann A.L., Hoffman F.M., Koven C.D. and Randerson J.T., *Plant responses to increasing CO<sub>2</sub> reduce estimates of climate impacts on drought severity*. Proceedings of the National Academy of Sciences, 2016. **113**(36): p. 10019-10024.
5. Niehaus F., *The Problem of Carbon Dioxide*. IAEA BULLETIN. **21**(1): p. 2-10.
6. Chris D.R. *The Effects of Carbon Dioxide on Air Pollution*. 2018 [cited 2021 10/3/2021]; Available from: <https://sciencing.com/list-5921485-effects-carbon-dioxide-air-pollution.html>.
7. Ashrafuzzaman M. and Furini G.L., *Climate change and human health linkages in the context of globalization: An overview from global to southwestern coastal region of Bangladesh*. Environment International, 2019. **127**: p. 402-411.
8. Jacobson T.A., Kler J.S., Hernke M.T., Braun R.K., Meyer K.C. and Funk W.E., *Direct human health risks of increased atmospheric carbon dioxide*. Nature Sustainability, 2019. **2**(8): p. 691-701.
9. Nahian M.A., Ahmed A., Lázár A.N., Hutton C.W., Salehin M., Streatfield P.K., et al., *Drinking water salinity associated health crisis in coastal Bangladesh*. Elementa: Science of the Anthropocene, 2018. **6**.
10. Statistical Review of World Energy. *The Statistical Review of World Energy analyses data on world energy markets from the prior year*. 2020 [cited 2021 10/3/2021]; Available from: <https://www.bp.com/content/dam/bp/business-sites/en/global/corporate/pdfs/energy-economics/statistical-review/bp-stats-review-2020-full-report.pdf>.
11. Fendt S., Buttler A., Gaderer M. and Spliethoff H., *Comparison of synthetic natural gas production pathways for the storage of renewable energy*. Wiley Interdisciplinary Reviews: Energy and Environment, 2016. **5**(3): p. 327-350.
12. Zhou G., Liu H., Xing Y., Xu S., Xie H. and Xiong K., *CO<sub>2</sub> hydrogenation to methane over mesoporous Co/SiO<sub>2</sub> catalysts: Effect of structure*. Journal of CO<sub>2</sub> Utilization, 2018. **26**: p. 221-229.
13. Perl K. *Natural gas expected to remain most-consumed fuel in the U.S. industrial sector*. 2018 [cited 2021 2021/4/12]; Available from: <https://www.eia.gov/todayinenergy/detail.php?id=35152>.
14. Nicole W., *Cooking up indoor air pollution: emissions from natural gas stoves*. 2014, National Institute of Environmental Health Sciences.
15. Leonard M.D., Michaelides E.E. and Michaelides D.N., *Energy storage needs for the substitution of fossil fuel power plants with renewables*. Renewable

- Energy, 2020. **145**: p. 951-962.
16. Cuéllar-Franca R.M. and Azapagic A., *Carbon capture, storage and utilisation technologies: A critical analysis and comparison of their life cycle environmental impacts*. Journal of CO<sub>2</sub> Utilization, 2015. **9**: p. 82-102.
  17. Gao P., Zhang L., Li S., Zhou Z. and Sun Y., *Novel Heterogeneous Catalysts for CO<sub>2</sub> Hydrogenation to Liquid Fuels*. ACS Central Science, 2020. **6**(10): p. 1657-1670.
  18. Yang H., Zhang C., Gao P., Wang H., Li X., Zhong L., et al., *A review of the catalytic hydrogenation of carbon dioxide into value-added hydrocarbons*. Catalysis science & technology, 2017. **7**(20): p. 4580-4598.
  19. Saeidi S., Najari S., Hessel V., Wilson K., Keil F.J., Concepción P., et al., *Recent advances in CO<sub>2</sub> hydrogenation to value-added products — Current challenges and future directions*. Progress in Energy and Combustion Science, 2021. **85**: p. 100905.
  20. Younas M., Loong Kong L., Bashir M.J.K., Nadeem H., Shehzad A. and Sethupathi S., *Recent Advancements, Fundamental Challenges, and Opportunities in Catalytic Methanation of CO<sub>2</sub>*. Energy & Fuels, 2016. **30**(11): p. 8815-8831.
  21. Mebrahtu C., Krebs F., Abate S., Perathoner S., Centi G. and Palkovits R., *Chapter 5 - CO<sub>2</sub> Methanation: Principles and Challenges*, in *Studies in Surface Science and Catalysis*, Albonetti S., Perathoner S., and Quadrelli E.A., Editors. 2019, Elsevier. p. 85-103.
  22. Yang L., Pastor-Pérez L., Villora-Pico J.J., Gu S., Sepúlveda-Escribano A. and Reina T.R., *CO<sub>2</sub> valorisation via reverse water-gas shift reaction using promoted Fe/CeO<sub>2</sub>-Al<sub>2</sub>O<sub>3</sub> catalysts: Showcasing the potential of advanced catalysts to explore new processes design*. Applied Catalysis A: General, 2020. **593**: p. 117442.
  23. Stangeland K., Kalai D., Li H. and Yu Z., *CO<sub>2</sub> Methanation: The Effect of Catalysts and Reaction Conditions*. Energy Procedia, 2017. **105**: p. 2022-2027.
  24. Lee W.J., Li C., Prajitno H., Yoo J., Patel J., Yang Y., and Lim S., *Recent trend in thermal catalytic low temperature CO<sub>2</sub> methanation: A critical review*. Catalysis Today, 2020.
  25. Hussain I., Jalil A.A., Hassan N.S. and Hamid M.Y.S., *Recent advances in catalytic systems for CO<sub>2</sub> conversion to substitute natural gas (SNG): Perspective and challenges*. Journal of Energy Chemistry, 2021. **62**: p. 377-407.
  26. Seemann M. and Thunman H., *9 - Methane synthesis*, in *Substitute Natural Gas from Waste*, Materazzi M. and Foscolo P.U., Editors. 2019, Academic Press. p. 221-243.
  27. Rönsch S., Schneider J., Matthischke S., Schlüter M., Götz M., Lefebvre J., et al., *Review on methanation – From fundamentals to current projects*. Fuel, 2016. **166**: p. 276-296.
  28. Zhan Y., Wang Y., Gu D., Chen C., Jiang L. and Takehira K., *Ni/Al<sub>2</sub>O<sub>3</sub>-ZrO<sub>2</sub> catalyst for CO<sub>2</sub> methanation: The role of  $\gamma$ -(Al, Zr)<sub>2</sub>O<sub>3</sub> formation*. Applied Surface Science, 2018. **459**: p. 74-79.
  29. Gao J., Liu Q., Gu F., Liu B., Zhong Z. and Su F., *Recent advances in methanation catalysts for the production of synthetic natural gas*. Rsc Advances, 2015. **5**(29): p. 22759-22776.

30. Xu Y., Wu Y., Li J., Wei S., Gao X. and Wang P., *Combustion-impregnation preparation of Ni/SiO<sub>2</sub> catalyst with improved low-temperature activity for CO<sub>2</sub> methanation*. International Journal of Hydrogen Energy, 2021.
31. Guo M. and Lu G., *The effect of impregnation strategy on structural characters and CO<sub>2</sub> methanation properties over MgO modified Ni/SiO<sub>2</sub> catalysts*. Catalysis Communications, 2014. **54**: p. 55-60.
32. Dias Y.R. and Perez-Lopez O.W., *CO<sub>2</sub> conversion to methane using Ni/SiO<sub>2</sub> catalysts promoted by Fe, Co and Zn*. Journal of Environmental Chemical Engineering, 2021. **9**(1): p. 104629.
33. Ye R.-P., Gong W., Sun Z., Sheng Q., Shi X., Wang T., et al., *Enhanced stability of Ni/SiO<sub>2</sub> catalyst for CO<sub>2</sub> methanation: Derived from nickel phyllosilicate with strong metal-support interactions*. Energy, 2019. **188**: p. 116059.
34. Alarcón A., Guilera J., Soto R. and Andreu T., *Higher tolerance to sulfur poisoning in CO<sub>2</sub> methanation by the presence of CeO<sub>2</sub>*. Applied Catalysis B: Environmental, 2020. **263**: p. 118346.
35. Han Y., Quan Y., Hao P., Zhao J. and Ren J., *Highly anti-sintering and anti-coking ordered mesoporous silica carbide supported nickel catalyst for high temperature CO methanation*. Fuel, 2019. **257**: p. 116006.
36. Sehested J., *Four challenges for nickel steam-reforming catalysts*. Catalysis Today, 2006. **111**(1): p. 103-110.
37. Kim S., Tsang Y.F., Kwon E.E., Lin K.-Y.A. and Lee J., *Recently developed methods to enhance stability of heterogeneous catalysts for conversion of biomass-derived feedstocks*. Korean Journal of Chemical Engineering, 2019. **36**(1): p. 1-11.
38. Ren J., Li H., Jin Y., Zhu J., Liu S., Lin J., and Li Z., *Silica/titania composite-supported Ni catalysts for CO methanation: Effects of Ti species on the activity, anti-sintering, and anti-coking properties*. Applied Catalysis B: Environmental, 2017. **201**: p. 561-572.
39. Siakavelas G.I., Charisiou N.D., AlKhoori S., AlKhoori A.A., Sebastian V., Hinder S.J., et al., *Highly selective and stable nickel catalysts supported on ceria promoted with Sm<sub>2</sub>O<sub>3</sub>, Pr<sub>2</sub>O<sub>3</sub> and MgO for the CO<sub>2</sub> methanation reaction*. Applied Catalysis B: Environmental, 2021. **282**: p. 119562.
40. Thema M., Weidlich T., Hörl M., Bellack A., Mörs F., Hackl F., et al., *Biological CO<sub>2</sub>-methanation: an approach to standardization*. Energies, 2019. **12**(9): p. 1670.
41. Gao J., Wang Y., Ping Y., Hu D., Xu G., Gu F., and Su F., *A thermodynamic analysis of methanation reactions of carbon oxides for the production of synthetic natural gas*. RSC advances, 2012. **2**(6): p. 2358-2368.
42. Bukhari S.N., Chong C.C., Setiabudi H.D., Cheng Y.W., Teh L.P. and Jalil A.A., *Ni/Fibrous type SBA-15: Highly active and coke resistant catalyst for CO<sub>2</sub> methanation*. Chemical Engineering Science, 2021. **229**: p. 116141.
43. Kesavan J.K., Luisetto I., Tuti S., Meneghini C., Iucci G., Battocchio C., et al., *Nickel supported on YSZ: The effect of Ni particle size on the catalytic activity for CO<sub>2</sub> methanation*. Journal of CO<sub>2</sub> Utilization, 2018. **23**: p. 200-211.
44. Shafiee P., Alavi S.M. and Rezaei M., *Mechanochemical synthesis method for the preparation of mesoporous Ni–Al<sub>2</sub>O<sub>3</sub> catalysts for hydrogen purification via CO<sub>2</sub> methanation*. Journal of the Energy Institute, 2021. **96**: p. 1-10.

45. Gholami S., Alavi S.M. and Rezaei M., *Preparation of highly active and stable nanostructured Ni-Cr<sub>2</sub>O<sub>3</sub> catalysts for hydrogen purification via CO<sub>2</sub> methanation reaction*. Journal of the Energy Institute, 2021. **95**: p. 132-142.
46. Taherian Z., Khataee A. and Orooji Y., *Promoted nickel-based catalysts on modified mesoporous silica support: The role of yttria and magnesia on CO<sub>2</sub> methanation*. Microporous and Mesoporous Materials, 2020. **306**: p. 110455.
47. Jaffar M.M., Nahil M.A. and Williams P.T., *Parametric study of CO<sub>2</sub> methanation for synthetic natural gas production*. Energy Technology, 2019. **7**(11): p. 1900795.
48. Aziz M.A.A., Jalil A.A., Triwahyono S., Mukti R.R., Taufiq-Yap Y.H. and Sazegar M.R., *Highly active Ni-promoted mesostructured silica nanoparticles for CO<sub>2</sub> methanation*. Applied Catalysis B: Environmental, 2014. **147**: p. 359-368.
49. Zhou L., Wang Q., Ma L., Chen J., Ma J. and Zi Z., *CeO<sub>2</sub> promoted mesoporous Ni/ $\gamma$ -Al<sub>2</sub>O<sub>3</sub> catalyst and its reaction conditions for CO<sub>2</sub> methanation*. Catalysis Letters, 2015. **145**(2): p. 612-619.
50. Hatzisymeon M., Petala A. and Panagiotopoulou P., *Carbon dioxide hydrogenation over supported Ni and Ru catalysts*. Catalysis Letters, 2021. **151**(3): p. 888-900.
51. Konsolakis M., Lykaki M., Stefa S., Carabineiro S.A., Varvoutis G., Papista E., and Marnellos G.E., *CO<sub>2</sub> hydrogenation over nanoceria-supported transition metal catalysts: role of ceria morphology (nanorods versus nanocubes) and active phase nature (Co versus Cu)*. Nanomaterials, 2019. **9**(12): p. 1739.
52. Han D., Kim Y., Byun H., Cho W. and Baek Y., *CO<sub>2</sub> Methanation of Biogas over 20 wt% Ni-Mg-Al Catalyst: on the Effect of N<sub>2</sub>, CH<sub>4</sub>, and O<sub>2</sub> on CO<sub>2</sub> Conversion Rate*. Catalysts, 2020. **10**(10): p. 1201.
53. Karelovic A. and Ruiz P., *Mechanistic study of low temperature CO<sub>2</sub> methanation over Rh/TiO<sub>2</sub> catalysts*. Journal of Catalysis, 2013. **301**: p. 141-153.
54. Zhu M., Ge Q. and Zhu X., *Catalytic reduction of CO<sub>2</sub> to CO via reverse water gas shift reaction: Recent advances in the design of active and selective supported metal catalysts*. Transactions of Tianjin University, 2020. **26**(3): p. 172-187.
55. Xu X., Tong Y., Huang J., Zhu J., Fang X., Xu J., and Wang X., *Insights into CO<sub>2</sub> methanation mechanism on cubic ZrO<sub>2</sub> supported Ni catalyst via a combination of experiments and DFT calculations*. Fuel, 2021. **283**: p. 118867.
56. Bian Z., Chan Y.M., Yu Y. and Kawi S., *Morphology dependence of catalytic properties of Ni/CeO<sub>2</sub> for CO<sub>2</sub> methanation: A kinetic and mechanism study*. Catalysis Today, 2020. **347**: p. 31-38.
57. Takano H., Kirihata Y., Izumiya K., Kumagai N., Habazaki H. and Hashimoto K., *Highly active Ni/Y-doped ZrO<sub>2</sub> catalysts for CO<sub>2</sub> methanation*. Applied Surface Science, 2016. **388**: p. 653-663.
58. Cárdenas-Arenas A., Quindimil A., Davó-Quiñonero A., Bailón-García E., Lozano-Castelló D., De-La-Torre U., et al., *Isotopic and in situ DRIFTS study of the CO<sub>2</sub> methanation mechanism using Ni/CeO<sub>2</sub> and Ni/Al<sub>2</sub>O<sub>3</sub> catalysts*. Applied Catalysis B: Environmental, 2020. **265**: p. 118538.
59. Ren J., Guo H., Yang J., Qin Z., Lin J. and Li Z., *Insights into the mechanisms of CO<sub>2</sub> methanation on Ni(111) surfaces by density functional theory*. Applied

- Surface Science, 2015. **351**: p. 504-516.
60. Jia X., Zhang X., Rui N., Hu X. and Liu C.-j., *Structural effect of Ni/ZrO<sub>2</sub> catalyst on CO<sub>2</sub> methanation with enhanced activity*. Applied Catalysis B: Environmental, 2019. **244**: p. 159-169.
  61. Low Y.K., *From Carbon Dioxide to Fuel: Kinetic Modelling of Methane Production in Carbon Dioxide Hydrogenation Processes*. 2020.
  62. Jalama K., *Carbon dioxide hydrogenation over nickel-, ruthenium-, and copper-based catalysts: Review of kinetics and mechanism*. Catalysis Reviews, 2017. **59**(2): p. 95-164.
  63. Baraj E., Vagaský S., Hlinčík T., Ciahotný K. and Tekáč V., *Reaction mechanisms of carbon dioxide methanation*. Chemical Papers, 2016. **70**(4): p. 395-403.
  64. Koschany F., Schlereth D. and Hinrichsen O., *On the kinetics of the methanation of carbon dioxide on coprecipitated NiAl(O)<sub>x</sub>*. Applied Catalysis B: Environmental, 2016. **181**: p. 504-516.
  65. Hernandez Lalinde J.A., Roongruangsree P., Ilsemann J., Bäumer M. and Kopyscinski J., *CO<sub>2</sub> methanation and reverse water gas shift reaction. Kinetic study based on in situ spatially-resolved measurements*. Chemical Engineering Journal, 2020. **390**: p. 124629.
  66. Prins R., *Eley-Rideal, the Other Mechanism*. Topics in Catalysis, 2018. **61**(9): p. 714-721.
  67. Davis M.E. and Davis R.J., *Fundamentals of chemical reaction engineering*. 2003: Courier Corporation. 228-230.
  68. *Chapter 5 Heterogeneous catalysis*, in *Studies in Surface Science and Catalysis*, van Santen R.A., et al., Editors. 1999, Elsevier. p. 209-287.
  69. Chiang J.H. and Hopper J.R., *Kinetics of the hydrogenation of carbon dioxide over supported nickel*. Industrial & Engineering Chemistry Product Research and Development, 1983. **22**(2): p. 225-228.
  70. Weatherbee G.D. and Bartholomew C.H., *Hydrogenation of CO<sub>2</sub> on group VIII metals: II. Kinetics and mechanism of CO<sub>2</sub> hydrogenation on nickel*. Journal of Catalysis, 1982. **77**(2): p. 460-472.
  71. Miguel C.V., Mendes A. and Madeira L.M., *Intrinsic kinetics of CO<sub>2</sub> methanation over an industrial nickel-based catalyst*. Journal of CO<sub>2</sub> Utilization, 2018. **25**: p. 128-136.
  72. Kai T., Takahashi T. and Furusaki S., *Kinetics of the methanation of carbon dioxide over a supported Ni-La<sub>2</sub>O<sub>3</sub> catalyst*. The Canadian Journal of Chemical Engineering, 1988. **66**(2): p. 343-347.
  73. Dew J., White R. and Sliepcevich C., *Hydrogenation of carbon dioxide on nickel-kieselguhr catalyst*. Industrial & Engineering Chemistry, 1955. **47**(1): p. 140-146.
  74. Lim J.Y., McGregor J., Sederman A. and Dennis J., *Kinetic studies of CO<sub>2</sub> methanation over a Ni/γ-Al<sub>2</sub>O<sub>3</sub> catalyst using a batch reactor*. Chemical Engineering Science, 2016. **141**: p. 28-45.
  75. Champon I., Bengaouer A., Chaise A., Thomas S. and Roger A.-C., *Carbon dioxide methanation kinetic model on a commercial Ni/Al<sub>2</sub>O<sub>3</sub> catalyst*. Journal of CO<sub>2</sub> Utilization, 2019. **34**: p. 256-265.
  76. Schaaf T., Grünig J., Schuster M.R., Rothenfluh T. and Orth A., *Methanation of*

- CO<sub>2</sub>-storage of renewable energy in a gas distribution system.* Energy, Sustainability and Society, 2014. **4**(1): p. 1-14.
77. Weekman Jr V.W., *Laboratory reactors and their limitations.* AIChE Journal, 1974. **20**(5): p. 833-840.
  78. Hernandez Lalinde J.A., Kofler K., Huang X. and Kopyscinski J., *Improved Kinetic Data Acquisition Using An Optically Accessible Catalytic Plate Reactor with Spatially-Resolved Measurement Techniques. Case of Study: CO<sub>2</sub> Methanation.* Catalysts, 2018. **8**(2): p. 86.
  79. Dalla Betta R.A., Piken A.G. and Shelef M., *Heterogeneous methanation: Steady-state rate of CO hydrogenation on supported ruthenium, nickel and rhenium.* Journal of Catalysis, 1975. **40**(2): p. 173-183.
  80. Cusumano J.A., Dalla Betta R.A. and Levy R.B., *Chapter 17 - Water-Gas Shift and Methanation Catalysis in the Synthesis of Substitute Natural Gas, in Catalysis in Coal Conversion,* Cusumano J.A., Dalla Betta R.A., and Levy R.B., Editors. 1978, Academic Press. p. 221-232.
  81. Burger T., Koschany F., Thomys O., Köhler K. and Hinrichsen O., *CO<sub>2</sub> methanation over Fe- and Mn-promoted co-precipitated Ni-Al catalysts: Synthesis, characterization and catalysis study.* Applied Catalysis A: General, 2018. **558**: p. 44-54.
  82. Fogler and Gurmen. *Collection and Analysis of Rate Data.* 2008 [cited 2021 3/31/2021]; Available from: <http://umich.edu/~elements/05chap/html/05prof3.htm>.
  83. Dry M., Shingles T. and Boshoff L., *Rate of the Fischer-Tropsch reaction over iron catalysts.* Journal of Catalysis, 1972. **25**(1): p. 99-104.
  84. Lunde P.J. and Kester F.L., *Carbon dioxide methanation on a ruthenium catalyst.* Industrial & Engineering Chemistry Process Design and Development, 1974. **13**(1): p. 27-33.
  85. Lim H.S., Kim G., Kim Y., Lee M., Kang D., Lee H., and Lee J.W., *Ni-exsolved La<sub>1-x</sub>Ca<sub>x</sub>NiO<sub>3</sub> perovskites for improving CO<sub>2</sub> methanation.* Chemical Engineering Journal, 2021. **412**: p. 127557.
  86. Karemore A.L., Sinha R., Chugh P. and Vaidya P.D., *Mixed reforming of methane over Ni-K/CeO<sub>2</sub>-Al<sub>2</sub>O<sub>3</sub>: Study of catalyst performance and reaction kinetics.* International Journal of Hydrogen Energy, 2021. **46**(7): p. 5223-5233.
  87. Pandey D., Ray K., Bhardwaj R., Bojja S., Chary K.V.R. and Deo G., *Promotion of unsupported nickel catalyst using iron for CO<sub>2</sub> methanation.* International Journal of Hydrogen Energy, 2018. **43**(10): p. 4987-5000.
  88. Lojewska J. and Dziembaj R., *Deactivation of cobalt hydrogenation catalyst induced by carbonaceous deposits. A model and its experimental verification, in Studies in Surface Science and Catalysis,* Delmon B. and Froment G.F., Editors. 1999, Elsevier. p. 121-128.
  89. Kai T., Furusaki S. and Yamamoyo K., *Methanation of carbon monoxide by a fluidized catalyst bed.* Journal of chemical engineering of Japan, 1984. **17**(3): p. 280-285.
  90. Zhao A., Ying W., Zhang H., Hongfang M. and Fang D., *Ni/Al<sub>2</sub>O<sub>3</sub> catalysts for syngas methanation: Effect of Mn promoter.* Journal of Natural Gas Chemistry, 2012. **21**(2): p. 170-177.
  91. Barrientos J., González N., Lualdi M., Boutonnet M. and Järås S., *The effect of*

- catalyst pellet size on nickel carbonyl-induced particle sintering under low temperature CO methanation*. Applied Catalysis A: General, 2016. **514**: p. 91-102.
92. Irankhah A., Haghtalab A., Farahani E.V. and Sadaghianizadeh K., *Fischer-Tropsch Reaction Kinetics of Cobalt Catalyst in Supercritical Phase*. Journal of Natural Gas Chemistry, 2007. **16**(2): p. 115-120.
  93. Hadjigeorghiou G.A. and Richardson J.T., *Fischer-Tropsch selectivity of Ni/Al<sub>2</sub>O<sub>3</sub> catalysts*. Applied Catalysis, 1986. **21**(1): p. 11-35.
  94. Marocco P., Morosanu E.A., Giglio E., Ferrero D., Mebrahtu C., Lanzini A., et al., *CO<sub>2</sub> methanation over Ni/Al hydrotalcite-derived catalyst: Experimental characterization and kinetic study*. Fuel, 2018. **225**: p. 230-242.
  95. Zhang M., Wang M., Xu B. and Ma D., *How to Measure the Reaction Performance of Heterogeneous Catalytic Reactions Reliably*. Joule, 2019. **3**(12): p. 2876-2883.
  96. Berger R. *EUROKIN spreadsheet on requirements for measurement of intrinsic kinetics in the gas-solid fixed bed reactor*. 2012; Available from: <https://docplayer.net/101923962-Eurokin-spreadsheet-on-requirements-for-measurement-of-intrinsic-kinetics-in-the-gas-solid-fixed-bed-reactor.html>.
  97. Aparicio L.M., *Transient Isotopic Studies and Microkinetic Modeling of Methane Reforming over Nickel Catalysts*. Journal of Catalysis, 1997. **165**(2): p. 262-274.
  98. Smith B., Muruganandam L., Murthy L. and Shantha S., *A Review of the Water Gas Shift Reaction Kinetics*. International Journal of Chemical Reactor Engineering - INT J CHEM REACT ENG, 2010. **8**.
  99. Yang X.-S., *4 - Data fitting and regression*, in *Introduction to Algorithms for Data Mining and Machine Learning*, Yang X.-S., Editor. 2019, Academic Press. p. 67-90.
  100. Xu J. and Froment G.F., *Methane steam reforming, methanation and water-gas shift: I. Intrinsic kinetics*. AIChE journal, 1989. **35**(1): p. 88-96.
  101. Ewald S., Kolbeck M., Kratky T., Wolf M. and Hinrichsen O., *On the deactivation of Ni-Al catalysts in CO<sub>2</sub> methanation*. Applied Catalysis A: General, 2019. **570**: p. 376-386.
  102. Garbarino G., Wang C., Cavattoni T., Finocchio E., Riani P., Flytzani-Stephanopoulos M., and Busca G., *A study of Ni/La-Al<sub>2</sub>O<sub>3</sub> catalysts: A competitive system for CO<sub>2</sub> methanation*. Applied Catalysis B: Environmental, 2019. **248**: p. 286-297.
  103. Lefebvre J., Bajohr S. and Kolb T., *A comparison of two-phase and three-phase CO<sub>2</sub> methanation reaction kinetics*. Fuel, 2019. **239**: p. 896-904.
  104. Tada S., Ikeda S., Shimoda N., Honma T., Takahashi M., Nariyuki A., and Satokawa S., *Sponge Ni catalyst with high activity in CO<sub>2</sub> methanation*. International Journal of Hydrogen Energy, 2017. **42**(51): p. 30126-30134.
  105. Fogler H.S., *Essentials of Chemical Reaction Engineering: Essenti Chemica Reactio Engi*. 2010: Pearson Education.
  106. Wang X., Hong Y., Shi H. and Szanyi J., *Kinetic modeling and transient DRIFTS-MS studies of CO<sub>2</sub> methanation over Ru/Al<sub>2</sub>O<sub>3</sub> catalysts*. Journal of Catalysis, 2016. **343**: p. 185-195.
  107. Vidal Vázquez F., Kihlman J., Mylvaganam A., Simell P., Koskinen-Soivi M.-L.



- and Alopaeus V., *Modeling of nickel-based hydrotalcite catalyst coated on heat exchanger reactors for CO<sub>2</sub> methanation*. Chemical Engineering Journal, 2018. **349**: p. 694-707.
108. Garbarino G., Bellotti D., Riani P., Magistri L. and Busca G., *Methanation of carbon dioxide on Ru/Al<sub>2</sub>O<sub>3</sub> and Ni/Al<sub>2</sub>O<sub>3</sub> catalysts at atmospheric pressure: Catalysts activation, behaviour and stability*. International Journal of Hydrogen Energy, 2015. **40**(30): p. 9171-9182.
  109. Phatak A.A., Koryabkina N., Rai S., Ratts J.L., Ruettinger W., Farrauto R.J., et al., *Kinetics of the water-gas shift reaction on Pt catalysts supported on alumina and ceria*. Catalysis Today, 2007. **123**(1): p. 224-234.
  110. Kikkawa S., *The Design of Active Sites for Selective Catalytic Conversion of Carbon Dioxide*. 2020.
  111. Richardson J.T., Garratt M. and Hung J.K., *Carbon dioxide reforming with Rh and Pt-Re catalysts dispersed on ceramic foam supports*. Applied Catalysis A: General, 2003. **255**(1): p. 69-82.
  112. Paksoy A.I., Yassi Akdag C., Selen Caglayan B. and Aksoylu A.E., *Kinetic and mechanistic features of carbon dioxide reforming of methane over Co-Ce/ZrO<sub>2</sub> catalysts*. International Journal of Chemical Kinetics, 2019. **51**(2): p. 138-145.
  113. Yang Lim J., McGregor J., Sederman A.J. and Dennis J.S., *Kinetic studies of CO<sub>2</sub> methanation over a Ni/γ-Al<sub>2</sub>O<sub>3</sub> catalyst using a batch reactor*. Chemical Engineering Science, 2016. **141**: p. 28-45.
  114. Duyar M.S., Ramachandran A., Wang C. and Farrauto R.J., *Kinetics of CO<sub>2</sub> methanation over Ru/γ-Al<sub>2</sub>O<sub>3</sub> and implications for renewable energy storage applications*. Journal of CO<sub>2</sub> Utilization, 2015. **12**: p. 27-33.
  115. Gruber M., Wiedmann D., Haas M., Harth S., Loukou A. and Trimis D., *Insights into the catalytic CO<sub>2</sub> methanation of a boiling water cooled fixed-bed reactor: Simulation-based analysis*. Chemical Engineering Journal, 2021. **406**: p. 126788.
  116. Rönsch S., Köchermann J., Schneider J. and Matthischke S., *Global reaction kinetics of CO and CO<sub>2</sub> methanation for dynamic process modeling*. Chemical Engineering & Technology, 2016. **39**(2): p. 208-218.
  117. Fuller E.N., Ensley K. and Giddings J.C., *Diffusion of halogenated hydrocarbons in helium. The effect of structure on collision cross sections*. The Journal of Physical Chemistry, 1969. **73**(11): p. 3679-3685.
  118. Linstrom P.J.E., *NIST Chemistry WebBook*. <http://webbook.nist.gov>, 2005.
  119. Sharma C.S., Harriott P. and Hughes R., *Thermal conductivity of catalyst pellets and other porous particles: Part II: Experimental measurements*. The Chemical Engineering Journal, 1975. **10**(1): p. 73-80.
  120. Poling B.E., Prausnitz J.M. and O'Connell J.P., *Properties of gases and liquids*. 2001: McGraw-Hill Education.
  121. Wakao N. and Funazkri T., *Effect of fluid dispersion coefficients on particle-to-fluid mass transfer coefficients in packed beds: correlation of Sherwood numbers*. Chemical Engineering Science, 1978. **33**(10): p. 1375-1384.
  122. Clifford A.A., Gray P. and Scott A.C., *Viscosities of gaseous argon, oxygen and carbon monoxide between 273 and 1300 K*. Journal of the Chemical Society, Faraday Transactions 1: Physical Chemistry in Condensed Phases, 1975. **71**: p. 875-882.

123. Vasheghani M., Marzbanrad E., Zamani C., Aminy M., Raissi B., Ebadzadeh T., and Barzegar-Bafrooei H., *Effect of  $Al_2O_3$  phases on the enhancement of thermal conductivity and viscosity of nanofluids in engine oil*. Heat and mass transfer, 2011. **47**(11): p. 1401-1405.
124. Moioli E., Gallandat N. and Züttel A., *Parametric sensitivity in the Sabatier reaction over  $Ru/Al_2O_3$  – theoretical determination of the minimal requirements for reactor activation*. Reaction Chemistry & Engineering, 2019. **4**(1): p. 100-111.





จุฬาลงกรณ์มหาวิทยาลัย  
**CHULALONGKORN UNIVERSITY**

## VITA

**NAME** ANGKANA KHUENPETCH

**DATE OF BIRTH** 13 Sep 1991

**PLACE OF BIRTH** Ranong, Thailand

**INSTITUTIONS ATTENDED** Chulalongkorn University

**HOME ADDRESS** 36/7 M.4, Banna, Kapoe, Ranong, 85120

**PUBLICATION** Choi, C., Khuenpetch, A., Zhang, W., Yasuda, S., Lin, Y., Machida, H., ... & Norinaga, K. (2021). Determination of Kinetic Parameters for CO<sub>2</sub> Methanation (Sabatier Reaction) over Ni/ZrO<sub>2</sub> at a Stoichiometric Feed-Gas Composition under Elevated Pressure. *Energy & Fuels*, 35(24), 20216-20223.

Angkana Khuenpetch, Cheolyong Choi, Prasert Reubroycharoen, Koyo Norinaga, Development of a kinetic model for CO<sub>2</sub> methanation over a commercial Ni/SiO<sub>2</sub> catalyst in a differential reactor, *Energy reports*, in press (2022)